

Revealing loss and degradation mechanisms in metal halide perovskite solar cells
The role of defects and trap states

Caselli, V.M.

DOI

[10.4233/uuid:f8361576-f35d-4334-8bee-68a48ed70037](https://doi.org/10.4233/uuid:f8361576-f35d-4334-8bee-68a48ed70037)

Publication date

2022

Document Version

Final published version

Citation (APA)

Caselli, V. M. (2022). *Revealing loss and degradation mechanisms in metal halide perovskite solar cells: The role of defects and trap states*. [Dissertation (TU Delft), Delft University of Technology].
<https://doi.org/10.4233/uuid:f8361576-f35d-4334-8bee-68a48ed70037>

Important note

To cite this publication, please use the final published version (if applicable).
Please check the document version above.

Copyright

Other than for strictly personal use, it is not permitted to download, forward or distribute the text or part of it, without the consent of the author(s) and/or copyright holder(s), unless the work is under an open content license such as Creative Commons.

Takedown policy

Please contact us and provide details if you believe this document breaches copyrights.
We will remove access to the work immediately and investigate your claim.

REVEALING LOSS AND DEGRADATION MECHANISMS IN METAL HALIDE PEROVSKITE SOLAR CELLS

THE ROLE OF DEFECTS AND TRAP STATES

REVEALING LOSS AND DEGRADATION MECHANISMS IN METAL HALIDE PEROVSKITE SOLAR CELLS

THE ROLE OF DEFECTS AND TRAP STATES

Proefschrift

ter verkrijging van de graad van doctor
aan de Technische Universiteit Delft,
op gezag van de Rector Magnificus prof. dr. ir. T.H.J.J. van der Hagen,
voorzitter van het College voor Promoties,
in het openbaar te verdedigen op 20 December 2022 om 12:30 uur

door

Valentina Marta CASELLI

Master of Science in Sustainable Energy Technology,
Technische Universiteit Delft, Delft, Nederland,
geboren te Varese, Italië.

Dit proefschrift is goedgekeurd door de

promotor: Dr. ir. T.J. Savenije

copromotor: Prof. dr. F.C. Grozema

Samenstelling promotiecommissie:

Rector Magnificus,
Dr. ir. T.J. Savenije,
Prof. dr. F.C. Grozema,

voorzitter
Technische Universiteit Delft
Technische Universiteit Delft

Onafhankelijke leden:

Dr. M. Morales Masis,
Prof. dr. T. Kirchartz,
Prof. dr. ir. O. Isabella,
Prof. dr. B. Dam,

Universiteit Twente
Forschungszentrum Jülich
Technische Universiteit Delft
Technische Universiteit Delft



Keywords: perovskites, defects, electronic trap states, time-resolved microwave conductance

Printed by: Ipskamp Printing

Front & Back: V.M. Caselli

Copyright © 2022 by V.M. Caselli

ISBN 978-94-6421-953-1

An electronic version of this dissertation is available at

<http://repository.tudelft.nl>

*Considerate la vostra semenza:
Foste non fatti a viver come bruti,
ma per seguir virtute e canoscenza.*

Dante Alighieri, La Divina Commedia, Inferno canto XXVI

CONTENTS

1	Introduction	1
1.1	A versatile class of materials: perovskites	2
1.2	Motivation and research aim	7
1.3	Outline of this thesis	9
2	Microwave Conductance Technique	15
2.1	Traditional set-up: time-resolved microwave conductance	16
2.2	Working principle	16
2.3	Different operational modes	18
3	Dielectric Losses and Charge Carrier Dynamics: the Role of the A-Cation	25
3.1	Methylammonium's dipole effect on MHPs properties	26
3.2	Temperature-dependent microwave conductance	27
3.3	Dielectric constants and relaxation time	29
3.4	Impact on charge carrier dynamics	31
3.5	Conclusions.	32
	Appendices	38
3.A	Sample characterization	39
3.B	Impedance spectroscopy	42
3.C	Computational details	44
4	Intra-Bandgap Regions in MAPbI₃: Urbach Tail and Defects	47
4.1	Trap states and Urbach tail	48
4.2	Sub-bandgap linear absorption region	49
4.3	Two photon absorption region	51
4.4	Surface and bulk defects	51
4.5	Charge transfer to C60 and spiro-OMeTAD	52
4.6	Urbach energy in MAPbI ₃	53
4.7	Intra-bandgap regions in MAPbI ₃	54
4.8	Conclusions.	56
	Appendices	60
4.A	Optical and structural characterization	61
4.B	TRMC traces fits	62
4.C	MAPbI ₃ below the bandgap absorption coefficient	64
4.D	Photothermal deflection spectroscopy	65

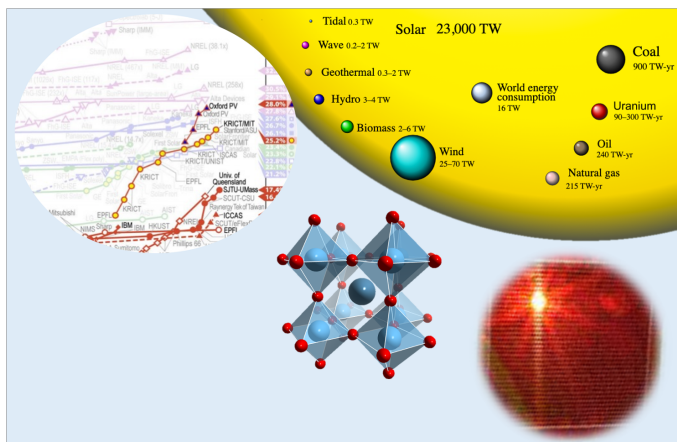
5	Recombination Losses in MAPbI₃ Single and Bilayers under Bias Illumination	67
5.1	Reducing recombination losses in perovskite solar cells	68
5.2	Quantifying recombination losses at the interface: a new approach	68
5.3	Methodology	70
5.4	Modelling of the TRMC traces with and without bias illumination	74
5.5	AM1.5 simulation	77
5.6	Conclusions.	80
	Appendices	83
5.A	Structural characterisation	83
5.B	Bias illumination	83
5.C	Additional microwave conductance data	84
6	Cs₂AgBiBr₆'s Traps in the Spotlight	89
6.1	Towards lead-free perovskites.	90
6.2	Perovskite synthesis and characterization.	91
6.3	Double pulse time-resolved microwave conductance (DPE-TRMC). . . .	91
6.4	Modelling.	93
6.5	Discussion	98
6.6	Verification with TRPL and TA	99
6.7	Extrapolation to solar light	100
6.8	Conclusions.	101
	Appendices	105
6.A	Cs ₂ AgBiBr ₆ thin film characterization.	105
6.B	Additional measurements.	107
6.C	Saha model	111
6.D	TRPL simulation	112
6.E	AM1.5 simulation	113
	Summary	115
	Samenvatting	119
	Acknowledgements	123
	Curriculum Vitae	125
	List of Publications	127

1

INTRODUCTION

For the first time, in 2021, the Intergovernmental Panel on Climate Change (IPCC) officially reported, black on white, the "unequivocal influence" of human behaviour on climate change. As the human population continues to grow, and so does the energy demand, we must switch to more sustainable and less polluting technologies. Luckily, we have feasible and practical alternatives provided by nature: renewable energy resources.

In the "Global Energy Review 2021", the International Energy Agency (IEA) reported that during the last years the demand for renewable energy production has increased, with the power sector leading the way, aiming to produce 8300 TWh from renewable energies alone. Among the different technologies, wind and solar are expected to be the major contributors to this transition. And it is in this scenario that perovskite solar cells could play a key role.



These statements are part of the IPCC "Climate Change 2021, The Physical Science Basis" and IEA "Global Energy Review 2021" reports available online.

1.1. A VERSATILE CLASS OF MATERIALS: PEROVSKITES

THE name perovskite was used for the first time in the 19th century, when a new mineral, CaTiO_3 , was discovered in the Ural Mountains by Gustavus Rose (1839) and named after the mineralogist Lev Perovski. Lately, the name perovskite has been applied to describe a class of materials with crystal structure similar to CaTiO_3 .¹ Owing to its ionic nature and tolerance factor, the perovskite structure is able to accommodate a great variety of ions, allowing the formation of versatile materials, suitable for different applications. Among the many options, a hybrid organic-inorganic, metal halide perovskite (MHP) composition captured the attention of scientists, as it showed remarkable opto-electronic properties suitable for utilization in devices such as solar cells, light emitting diodes (LEDs), photo-detectors, etc.²⁻⁵

One of the first applications of MHPs dates back to 2009, when a dye-sensitized perovskite-based solar cell (PSC) was built by Miyasaka's group, achieving a 3.8% efficiency.² Only few years later, in 2015, NREL certified a 21% efficient planar perovskite-based solar cell.⁶ This astonishing growth has since then captivated the attention of the scientific community and many groups are nowadays devoted to investigate the properties of these remarkable materials.

This first chapter is dedicated to provide a general introduction to the properties of metal halide perovskites. As the aim of this thesis is to investigate losses and degradation mechanisms in perovskites mainly for photovoltaic applications, the discussion will concentrate on the so called 3D perovskites. Their main structural and opto-electronic properties will be discussed in the following sections.

PEROVSKITE CRYSTAL STRUCTURE

The 3D halide perovskite structure is the most studied variant for optoelectronic device applications. It is generally described by the formula ABX_3 , where A is monovalent cation, B a bivalent cation, and X an anion. As mentioned before, both organic and inorganic ions have been tested leading to the formation of either hybrid or fully inorganic perovskites. A representation of the cubic 3D ABX_3 structure is shown in Figure 1.1, where the most commonly used ions are listed. While formamidium (FA^+), methylammonium (MA^+) or caesium (Cs^+) are employed as A-site cations, lead (Pb^{2+}) and tin (Sn^{2+}) generally occupy the B-site, coordinated to six anions to form the octahedra visible in Figure 1.1.⁷

The ion size plays a fundamental role in the formation of the crystals. The stability of a specific structure can be assessed by the Goldsmith tolerance factor, t , as defined in equation 1.1:⁸

$$t = \frac{r_A + r_X}{\sqrt{2}r_B + r_X} \quad (1.1)$$

where r_A , r_B and r_X are the ionic radii of the A, B and X ions, respectively. The 3D perovskite structure can be formed if $0.8 < t < 1$. For its stability, the A-cation plays a dominant role; in fact, if the A-cation is too small, the octahedra would tilt to fill the empty space, leading to a stable orthorhombic structure (to the limit of $t=0.8$). On the other hand, an A-cation that is too large would lead to a preferred hexagonal close-packed structure.⁹ Structural deformations can also be induced by partial substitution of the

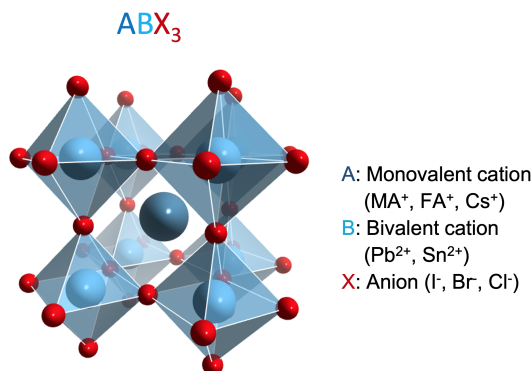


Figure 1.1: The cubic perovskite crystal structure. A is a monovalent organic or inorganic cation, B a bivalent metal cation, and X an anion.

constituent atoms, often leading to improved stability of the perovskite phase. For example, a strategy to stabilize the otherwise structurally unstable CsPbI₃ involves the addition of the larger formamidinium cation.¹⁰ Similarly, to stabilize the highly mobile organic methylammonium cation, Cs⁺ and FA⁺ can be added during synthesis.⁹ Moreover, the halide can also influence the stability of a specific structure; an example is given by comparing the stable phases of MAPbI₃ and MAPbBr₃. At room temperature, the former is in the tetragonal phase, while the latter in the cubic structure.^{11,12}

OPTO-ELECTRONIC PROPERTIES

Optical properties are of utmost importance for an optoelectronic device. The proven suitability of perovskites as light absorber materials in a solar cell results from their high absorption coefficient in the visible region of the solar spectrum (10^4 - 10^5 cm⁻¹)¹³ in addition to the great advantage of having tunable bandgaps. As shown in Figure 1.2, bandgaps higher than 3.5 eV as well as low as 1.2 eV can be obtained by varying the ionic composition. In particular, the B and X ions have a great impact on the optical properties of perovskites. As revealed by several theoretical and experimental studies, this is related to the fact that the valence and conduction bands in perovskites are predominately formed by the B and X orbitals.¹⁴⁻¹⁶ More specifically, the *s* orbitals of the B metal and *p* orbitals of the X anion are the major contributors to the valence band (VB), while *p* orbitals of the B ion form the conduction band (CB).¹⁴⁻¹⁶ A detailed study by Tao et al., revealed the interplay of electronegativity, hybridisation strength and structural deformations on the bandgap of different perovskites.¹⁷ On the other hand, while the A-cation does not directly affect the electronic bands, it can distort the crystal lattice, leading to variation of the bandgap itself.^{18,19} Alternatively, doping has also been suggested as a possible route to tune the bandgap energy of perovskites.²⁰⁻²⁴

Bandgap tuning can be achieved not only by complete substitution of the constituent atoms, but also by mixing the composition to achieve specific requirements. A commonly applied method to tune the bandgap in MHPs is the partial substitution of iodide with bromide ions.²⁵ However, in this process, attention must be paid to effectively ba-

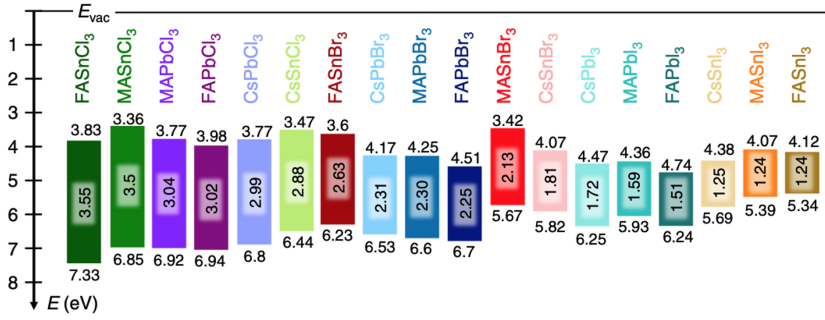


Figure 1.2: Energy level diagram of metal halide perovskites of different composition. Image by Tao et al.¹⁷

lance the positive and negative effects of substitution. For example, in mixed halide perovskites phase segregation due to halide migration is a widely recognized issue.^{26–28} In an attempt to replace the toxic lead and to lower the bandgap, complete or partial substitution with tin has been tested.¹⁷ However, due to the fast oxidation of Sn^{2+} into Sn^{4+} , the introduction of Sn in devices is still challenging.^{29–31}

MHPs also exhibit low exciton binding energies. Excitons are coulombically bound electron-hole pairs, whose presence in semiconductors can affect the opto-electronic properties of the material. In Pb-based perovskites, the exciton binding energies are relatively low, in the order of 10-50 meV at room temperature, which ensures high yields of free carrier generation upon photoexcitation.^{32–34} On top of that, appreciable charge carriers mobilities have been measured not only in crystals ($10\text{-}800\text{ cm}^2/(\text{Vs})$),^{35–41} but also in thin films ($1\text{-}100\text{ cm}^2/(\text{Vs})$)^{42–47} of both Pb- and Sn-based perovskites. As such, long charge carrier diffusion lengths (several tens of nm to over $1\mu\text{m}$) have been observed in devices under solar illumination intensities, desirable for efficient charge extraction in devices.^{6,42,48}

Notwithstanding all these favourable properties for diverse optoelectronic applications, perovskites do suffer of intrinsic instability and are prone to defect formation. As it will be presented in the coming section, lattice defects can lead to the emergence of electronic trap states, detrimental in devices.

DEFECTS AND TRAP STATES IN PEROVSKITES

Although ideally each atom in a crystal lattice should have its equilibrium position at a specific site, the formation of structural defects in the solid states is inevitable. Such disruption in the periodicity of a lattice can severely impact not only the structural properties of a solid but also its opto-electronic characteristics; the presence of structural defects can affect the lattice bonding and orbital configuration, introduce intra-bandgap electronic states in which electrons and holes may get trapped and limit the overall charge carrier diffusion length.

As extensively discussed by Jin et al.⁴⁹ and shown in Figure 1.3, different types of defects have been identified in perovskites that can be divided into two main categories:

1. Intrinsic defects, i.e. vacancies, interstitials and anti-site substitutions, line defects;
2. Extrinsic defects, e.g. grain boundaries, foreign atom substitutions and unsaturated surface bonds.

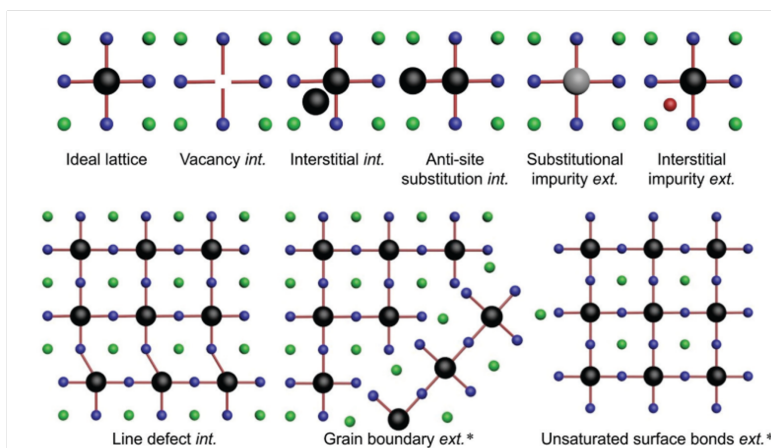


Figure 1.3: Schematic representation of defects in a perovskite crystal lattice. Intrinsic defects are indicated as *int.*, while extrinsic defects are denominated *ext.* The A cation is shown in green, B in black and X in blue.⁴⁹

Intrinsic defects arise from displacements of the atoms in the crystal lattice or the presence of impurity atoms. Due to the complexity of the perovskite structure, varying the ion constituents affects the defect formation energies and ionization levels. In order to understand these differences, it is important to underline the types of chemical bonds in the lattice; a distinction is made between the metal halide framework (BX_3^-) and the A-cation framework interactions. In presence of dipolar molecules like methylammonium and formamidinium, intermolecular interactions also play a role in the formation of defects and their ionisation energies. As it can be expected, these interactions are stronger when MA^+ is present, whose permanent dipole reorientation can also affect the dielectric properties of perovskites.⁵⁰

Metal halide framework: the bonds between the B and X ions consist of mixed ionic/covalent interactions, with low electrostatic potentials.⁵⁰ The antibonding *s-p* coupling between lead and halides is energetically unfavorable, resulting in an easier formation of lattice vacancies.^{50,51} Supporting this statement, several density functional theory (DFT) simulations have confirmed the relatively low formation energies for Pb vacancies (V_{Pb}^{2-}), one of the most stable defects in lead halide perovskites.^{51–53} Halide vacancies (V_X^+) can also be formed, especially in positively charged environments, possibly compensating halide interstitials (Frenkel defect - stoichiometric vacancy/interstitial pair) and/or

coupling with the metal vacancies (Schottky defect - stoichiometric vacancy/vacancy pair).⁵³ Together with V_{Pb}^{2-} , halide interstitials (X_i^-) are amongst the most stable defects in perovskites.^{51–53} A detailed study from Meggiolaro et al. shows that both defects exhibit charge transitions within the perovskite bandgap;⁵² this leads to the presence of defects ionization levels throughout the bandgap of the materials, increasing the chances of deep trapping of both electrons and holes.⁵³

A-cation framework: the bond in between the A-cations and the inorganic cage is electrostatic in nature.⁵⁰ If molecules like MA and FA are involved, dipolar and hydrogen bonds also contribute to the stability of the structure. As proven by different studies, the interactions of the A-cation and the framework are weak, resulting in low formation energies for stable interstitial defects.^{51–53} Nonetheless, as the monovalent cation is not directly involved in the electronic structure of the materials, the defects states formed are typically shallow.^{51,53}

The thermodynamic ionization energies of the most stable defects in MAPbI₃ and MAPbBr₃ are shown in Figure 1.4. As discussed, and visible from Figure 1.4, lead vacancies and halide interstitials have the potential to become detrimental deep trap states in the materials, while the other defects can be considered as shallow.

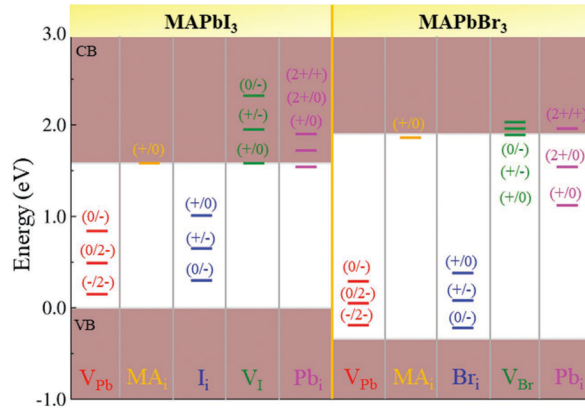


Figure 1.4: Ionization energy of the most stable defects in MAPbI₃ and MAPbBr₃, as presented by Motti et al.⁵³

Another important factor that needs to be taken into account when discussing the impact of defects on charge carrier dynamics in perovskites is their (re)activity. Although thermodynamically stable, defect formation may be hindered if they present high activation barriers to migration.⁵² It is broadly recognised that vacancy or interstitial-mediated migrations of halide and MA ions are faster than Pb migration;^{54–56} this makes the former two species the major contributors not only to defect activity, but also to the instability of MHPs.

1.2. MOTIVATION AND RESEARCH AIM

The ionic complexity of the system and the great variety of defects that can be formed during device fabrication has made a quantitative analysis of defect states in perovskites a challenge. Many techniques have been employed in recent years to provide qualitative and quantitative characterisation of defect states in perovskites of different compositions. Among them, sub-bandgap investigation by optical spectroscopy has been performed on perovskite thin films, e.g. absorption and photoluminescence (PL)^{52,53,57,58}, transient absorption (TA)^{52,59}, and photothermal deflection spectroscopy (PDS)^{60,61}. Different device characterisation techniques have also been applied for this purpose, like thermally stimulated current (TSC)⁶² and photocurrent spectroscopy.^{57,61,63} In the framework of these studies this thesis fits in.

The aim of this thesis is to reveal the efficiency losses and degradation mechanisms in perovskites of different composition by analysing the nature and impact of trap states on charge carrier dynamics in single and bilayer systems.

In the upcoming chapters the nature and impact of the most detrimental electronic trap states will be revealed by means of time-resolved conductance (TRMC) measurements. As it will be further discussed in Chapter 2, this technique is based on the interaction of microwaves with photo-excited charge carriers, i.e. electrons and holes. The TRMC offers several advantages compared to the mentioned analytical methods; firstly, it is contactless. This condition brings two major advances: the signal is not affected by additional parasitic losses and there is no need to fabricate a full, optimised device. Secondly, radiative and non-radiative processes can be revealed as the photoconductance response arises from the interaction of microwaves with mobile charge carriers. This implies that, although one carrier may be immobile in a trap state, its mobile counter-charge would still contribute the signal. Furthermore, the high sensitivity of the system allows the investigation of kinetic processes at low excitation intensities, out of the region of high-order recombination mechanisms, like Auger recombination.

All these characteristics make TRMC a unique, powerful tool to investigate the charge carrier dynamics under a broad range of excitation energies and intensities. In this thesis, TRMC analyses have been performed under different operational conditions. Each of them allowed the investigation of specific processes related to loss mechanisms in perovskites with different compositions. While the details will be discussed in Chapter 2, an overview is also provided in the following sections.

STEADY-STATE MICROWAVE CONDUCTANCE

As implied by its name, TRMC is a time-resolved technique. However, its fundamental working principle is based on the interaction of microwaves with a dielectric medium and, if operated in the dark, steady-state conductance measurements can be performed. Such measurements can provide very useful information on materials properties like the background concentration of charge carriers in thermal equilibrium. The presence of background carrier in the dark can originate from ionisation of charged defects. Depending on their concentrations, their presence can deeply affect the time-dependent charge carrier dynamics. As such it is important to know:

Can we quantify the background charge carrier concentration and how does it relate to the presence of defects?

To this end, steady-state microwave conductance (SSMC) measurements have been performed on different Pb-based perovskites. However, interpretation of the results must be careful as the presence of permanent dipoles, like in the case of MA^+ , can influence the dielectric properties of the sample.

How are TRMC measurements influenced by dielectric losses and does the nature of the A cation affect the charge carrier dynamics in perovskites?

Furthermore, SSMC measurements can also be performed in the presence of a continuous illumination source. Information about the charge carriers' concentration upon different illumination condition are very powerful to relate the time-resolved results to device operational conditions.

SUB-BANDGAP ANALYSIS

Reducing the trap state density has been a major point of interest of many research groups in the past years. Several strategies have been applied, during and after the synthesis process, as well as the use of additives in the precursor solution. Different techniques and computational methods have been employed to predict the origin and to estimate the number of deep defects in different perovskites. However, the relative low concentration of such defects makes it difficult to quantify them, as well as experimentally characterise their nature.

Can we quantify and characterize deep trap states in metal halide perovskites?

Thanks to the high sensitivity of the TRMC, the presence of an optically active state can be revealed, despite one carrier being effectively immobile. As it has been already discussed in a TRMC study focused on the two-photon absorption process in MAPbI_3 , excitation with low intensities can lead to sub-bandgap linear absorption (SLA);⁶⁴ this process originates from optically active transitions of electrons either from the VB into a trap state, or from photo-active defects into the CB. As such, either VB holes or CB electrons would contribute to a photoconductance signal, respectively. Discrimination in between the two contributions can only be made in the presence of an additional selective transport material that can efficiently collect one type of carrier.

INTERFACIAL DEFECTS CHARACTERISATION

A major point of concern for device optimisation is reducing the losses at the interfaces with transport layers, as well as electrical contacts. One of the main questions for an effective device optimisation is:

Which recombination mechanism is responsible for charge carrier losses in perovskite/selective transport layer bilayers?

Although very informative, time-resolved measurements may fail to provide a quantitative analysis of the recombination processes during steady state illumination condition.

This limitation is inherent to perovskites due to light-induced instability related to ionic motion. For this reason, an additional continuous illumination source has been added to the TRMC set-up, allowing the determination of kinetic parameters under steady state illumination.

DOUBLE PULSE EXCITATION TRMC

The most innovative method introduced in this thesis is the double pulse excitation TRMC experiments (DPE-TRMC). As it will be discussed more extensively in the next chapter, the original TRMC set-up is equipped with a second laser source that is coupled to the first one by means of an electronic delay generator. This configuration offers several advantages, such as the selective tunability of the two excitation sources and an accurate control over the delay time between the two pulses.

DPE-TRMC analysis is then an extremely powerful tool which can be used to investigate the charge carrier (de-)trapping processes and the results can provide unique insights into charge carrier trapping in perovskites. One of the fundamental questions that is addressed is:

Is it possible to release a trapped charge carrier with a second pulse? Is the release limited by the trap-assisted recombination rate?

This option is investigated by setting the energy of the second pulse lower than the bandgap.

What are the energy levels of the most active defects?

If the previous option is verified, it would be possible to map the intra-bandgap defect region by varying the delayed excitation wavelength.

How does the trap population evolve over time?

This can be done by acting on the delay time between the two excitations.

The answers to these questions would be able to provide us a unique insight on charge carrier (de-)trapping dynamics in different perovskites. In addition, DPE-TRMC can also be applied also to different type of studies, like the investigation of the effect of phase segregation in mixed halide perovskites by selectively exciting the bulk and the segregated domains at different wavelengths.

1.3. OUTLINE OF THIS THESIS

Regarding the overall structure of this thesis, five more chapters will be following in addition to the current introductory one. In Chapter 2, the main experimental technique applied in this thesis, i.e. TRMC, will be introduced in detail, including the set-up variations mentioned in the previous section. Chapter 3 will be focused on the dielectric properties of different Pb-based perovskites revealed by temperature-dependent SMC measurements. Chapter 4 will present the results of the sub-bandgap investigation of MAPbI₃ thin films. Different sub-bandgap regimes are identified on the basis of the charge carrier decay kinetics, namely band tail absorption, sub-bandgap linear absorption, and

two photon-absorption regimes. The addition of selective electron or hole transport layers allows us to discriminate over the nature of these optically active sub-bandgap states. In Chapter 5, the focus will move towards the characterisation of the interface with selective transport layers (TLs). For this study, the most commonly applied TLs in the planar p-i-n and n-i-p solar cell configurations have been investigated, namely C60 (ETL), and Spiro-OMeTAD (HTL). The kinetic parameters are extracted in absence and presence of bias illumination, revealing the strong influence of light-induced ionic migration on the charge carrier dynamics. In the last chapter the attention will be shifted towards lead-free materials, more specifically the complex alternative of double metal AB'B''X₆ perovskites. Chapter 6 will provide a comprehensive overview of the charge carrier properties in CsAgBiBr₆ perovskite. Using DPE-TRMC measurements, we reveal the interplay in between excitons, colour centres and shallow trap states and their effect on the opto-electronic properties of this material.

BIBLIOGRAPHY

- (1) Wenk, H.-R.; Bulakh, A., *Minerals: Their Constitution and Origin*; Press, C. U., Ed., 2004.
- (2) Kojima, A.; Teshima, K.; Shirai, Y.; Miyasaka, T. *Journal of the American Chemical Society* **2009**, *131*, 6050–6051.
- (3) Tan, Z.-K.; Moghaddam, R. S.; Lai, M. L.; Docampo, P.; Higler, R.; Deschler, F.; Price, M.; Sadhanala, A.; Pazos, L. M.; Credgington, D.; Hanusch, F.; Bein, T.; Snaith, H. J.; Friend, R. H. *Nature Nanotechnology* **2014**, *9*, 687–692.
- (4) Li, C.; Ma, Y.; and Liang Shen, Y. X.; Ding, L. *InfoMat* **2020**, *2*, 1247–1256.
- (5) Lin, Q.; Burn, A. A. P. L.; Meredith, P. *Nature Photonics* **2015**, *9*, 687–694.
- (6) Bi, Y.; Hutter, E. M.; Fang, Y.; Dong, Q.; Huang, J.; Savenije, T. J. *Journal of Physical Chemistry Letters* **2016**, *7*, 923–928.
- (7) Frost, J. M.; Butler, K. T.; Brivio, F.; Hendon, C. H.; van Schilfgaarde, M.; Walsh, A. *Nano letters* **2014**, *14*, 2584–90.
- (8) Golschmidt, V. M. *Die Naturwissenschaften* **1926**, *21*, 1247–1256.
- (9) Saliba, M.; Matsui, T.; Seo, J.-Y.; Domanski, K.; Correa-Baena, J.-P.; Nazeeruddin, M. K.; Zakeeruddin, S. M.; Tress, W.; Abate, A.; Hagfeldt, A.; Grätzel, M. *Energy Environ. Sci.* **2016**, 1989.
- (10) Li, Z.; Yang, M.; Park, J.-S.; Su-Huai, W.; Berry, J. J.; Zhu, K. *Chem. Mater.* **2016**, *1*, 284–292.
- (11) Quarti, C.; Mosconi, E.; Ball, J. M.; D’Innocenzo, V.; Tao, C.; Pathak, S.; Snaith, H. J.; Petrozza, A.; De Angelis, F. *Energy Environ. Sci.* **2016**, 155–163.
- (12) Wang, K.-H.; Li, L.-C.; Shellaiah, M.; Sun, K. W. *Scientific Reports* **2017**, *7*.
- (13) Wolf, S. D.; Holovsky, J.; Moon, S. J.; Löper, P.; Niesen, B.; Ledinsky, M.; Haug, F. J.; Yum, J. H.; Ballif, C. *Journal of Physical Chemistry Letters* **2014**, *5*, 1035–1039.
- (14) Philippe, B.; Jacobsson, T. J.; Correa-Baena, J. P.; Jena, N. K.; Banerjee, A.; Chakraborty, S.; Cappel, U. B.; Ahuja, R.; Hagfeldt, A.; Odelius, M.; Rensmo, H. *Journal of Physical Chemistry C* **2017**, *121*, 26655–26666.
- (15) Endres, J.; Egger, D. A.; Kulbak, M.; Kerner, R. A.; Zhao, L.; Silver, S. H.; Hodes, G.; Rand, B. P.; Cahen, D.; Kronik, L.; Kahn, A. *Journal of Physical Chemistry Letters* **2016**, *7*, 2722–2729.
- (16) Tao, S. X.; Cao, X.; Bobbert, P. A. *Scientific Reports* **2017**, *7*, 1–9.
- (17) Tao, S.; Schmidt, I.; Brocks, G.; Jiang, J.; Tranca, I.; Meerholz, K.; Olthof, S. *Nature Communications* **2019**, *10*, DOI: [10.1038/s41467-019-10468-7](https://doi.org/10.1038/s41467-019-10468-7).

- (18) Prasanna, R.; Gold-Parker, A.; Leijtens, T.; Conings, B.; Babayigit, A.; Boyen, H.-G.; Toney, M. F.; McGehee, M. D. *Journal of the American Chemical Society* **2017**, *139*, PMID: 28704048, 11117–11124.
- (19) McMeekin, D. P.; Sadoughi, G.; Rehman, W.; Eperon, G. E.; Saliba, M.; Hörantner, M. T.; Haghighirad, A.; Sakai, N.; Korte, L.; Rech, B.; Johnston, M. B.; Herz, L. M.; Snaith, H. J. *Science* **2016**, *351*, 151–155.
- (20) Hasegawa, H.; Kobayashi, K.; Takahashi, Y.; Harada, J.; Inabe, T. *Journal of Materials Chemistry C* **2017**, *5*, 4048–4052.
- (21) Kholil, M. I.; Bhuiyan, M. T.; Rahman, M. A.; Ali, M. S.; Aftabuzzaman, M. *AIP Advances* **2021**, *11*, DOI: [10.1063/5.0042847](https://doi.org/10.1063/5.0042847).
- (22) Tang, Z. K.; Xu, Z. F.; Zhang, D. Y.; Hu, S. X.; Lau, W. M.; Liu, L. M. *Scientific Reports* **2017**, *7*, 1–7.
- (23) Phung, N. et al. *Journal of the American Chemical Society* **2020**, *142*, 2364–2374.
- (24) Luo, J.; Lin, F.; Xia, J.; Yang, H.; Zhang, R.; Malik, H. A.; Shu, H.; Wan, Z.; Han, K.; Wang, R.; Yao, X.; Jia, C. *Nano Energy* **2021**, *82*, 105751.
- (25) Hoke, E. T.; Slotcavage, D. J.; Dohner, E. R.; Bowring, A. R.; Karunadasa, H. I.; McGehee, M. D. *Chemical Science* **2015**, *6*, 613–617.
- (26) Tang, X.; Van Den Berg, M.; Gu, E.; Horneber, A.; Matt, G. J.; Osvet, A.; Meixner, A. J.; Zhang, D.; Brabec, C. J. *Nano Letters* **2018**, *18*, 2172–2178.
- (27) Knight, A. J.; Borchert, J.; Oliver, R. D.; Patel, J. B.; Radaelli, P. G.; Snaith, H. J.; Johnston, M. B.; Herz, L. M. *ACS Energy Letters* **2021**, *6*, 799–808.
- (28) Slotcavage, D. J.; Karunadasa, H. I.; McGehee, M. D. *ACS Energy Letters* **2016**, *1*, 1199–1205.
- (29) Shao, S.; Dong, J.; Duim, H.; ten Brink, G. H.; Blake, G. R.; Portale, G.; Loi, M. A. *Nano Energy* **2019**, *60*, 810–816.
- (30) *Nature Communications* **2021**, *12*, 1–11.
- (31) Cao, J.; Yan, F. *Energy and Environmental Science* **2021**, *14*, 1286–1325.
- (32) Ruf, F.; Aygüler, M. F.; Giesbrecht, N.; Rendenbach, B.; Magin, A.; Docampo, P.; Kalt, H.; Hetterich, M. *APL Materials* **2019**, *7*, DOI: [10.1063/1.5083792](https://doi.org/10.1063/1.5083792).
- (33) Chen, X.; Lu, H.; Yang, Y.; Beard, M. C. *Journal of Physical Chemistry Letters* **2018**, *9*, 2595–2603.
- (34) Miyata, A.; Mitoglu, A.; Plochocka, P.; Portugall, O.; Wang, J. T. W.; Stranks, S. D.; Snaith, H. J.; Nicholas, R. J. *Nature Physics* **2015**, *11*, 582–587.
- (35) Dong, Q.; Fang, Y.; Shao, Y.; Mulligan, P.; Qiu, J.; Cao, L.; Huang, J. *Science (New York, N.Y.)* **2015**, *347*, 967–970.
- (36) Semonin, O. E. et al. *The Journal of Physical Chemistry Letters* **2016**, *7*, 3510–3518.
- (37) Chen, Y.; Yi, H. T.; Wu, X.; Haroldson, R.; Gartstein, Y. N.; Rodionov, Y. I.; Tikhonov, K. S.; Zakhidov, A.; Zhu, X. Y.; Podzorov, V. *Nature Communications* **2016**, *7*, DOI: [10.1038/ncomms12253](https://doi.org/10.1038/ncomms12253).

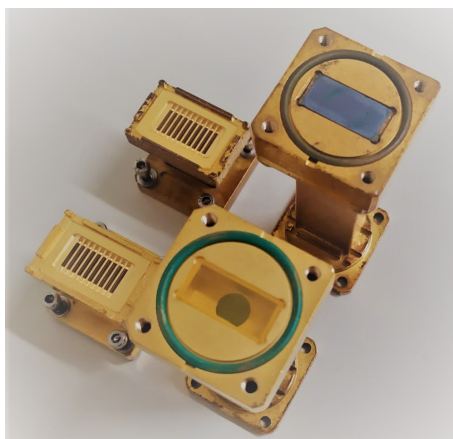
- (38) Saidaminov, M. I.; Abdelhady, A. L.; Murali, B.; Alarousu, E.; Burlakov, V. M.; Peng, W.; Dursun, I.; Wang, L.; He, Y.; Maculan, G.; Goriely, A.; Wu, T.; Mohammed, O. F.; Bakr, O. M. *Nature Communications* **2015**, *6*, 7586.
- (39) Valverde-Chávez, D. A.; Ponseca, C. S. J.; Stoumpos, C. C.; Yartsev, A.; Kanatzidis, M. G.; Sundström, V.; Cooke, D. G. *Energy Environ. Sci.* **2015**, *8*, DOI: [10.1039/C5EE02503F](https://doi.org/10.1039/C5EE02503F).
- (40) Stoumpos, C. C.; Malliakas, C. D.; Kanatzidis, M. G. *Inorganic Chemistry* **2013**, *52*, 9019–9038.
- (41) Takahashi, Y.; Hasegawa, H.; Takahashi, Y.; Inabe, T. *Journal of Solid State Chemistry* **2013**, *205*, 39–43.
- (42) Hutter, E. M.; Eperon, G. E.; Stranks, S. D.; Savenije, T. J. *Journal of Physical Chemistry Letters* **2015**, *6*, 3082–3090.
- (43) Brenes, R.; Guo, D.; Osherov, A.; Noel, N. K.; Eames, C.; Hutter, E. M.; Pathak, S. K.; Niroui, F.; Friend, R. H.; Islam, M. S.; Snaith, H. J.; Bulović, V.; Savenije, T. J.; Stranks, S. D. *Joule* **2017**, *1*, 155–167.
- (44) Reid, O. G.; Yang, M.; Kopidakis, N.; Zhu, K.; Rumbles, G. *ACS Energy Letters* **2016**, *1*, 561–565.
- (45) Caselli, V. M.; Wei, Z.; Ackermans, M. M.; Hutter, E. M.; Ehrler, B.; Savenije, T. J. *ACS Energy Letters* **2020**, *5*, 3821–3827.
- (46) Milot, R. L.; Eperon, G. E.; Snaith, H. J.; Johnston, M. B.; Herz, L. M. *Advanced Functional Materials* **2015**, *25*, 6218–6227.
- (47) Milot, R. L.; Eperon, G. E.; Green, T.; Snaith, H. J.; Johnston, M. B.; Herz, L. M. *J. Phys. Chem. Lett.* **2016**, *7*, 4178–4184.
- (48) Stranks, S. D.; Eperon, G. E.; Grancini, G.; Menelaou, C.; Alcocer, M. J. P.; Leijtens, T.; Herz, L. M.; Petrozza, A.; Snaith, H. J. *Science* **2013**, *342*, 341–344.
- (49) Jin, H.; Debroye, E.; Keshavarz, M.; Scheblykin, I. G.; Roeffaers, M. B.; Hofkens, J.; Steele, J. A. *Materials Horizons* **2020**, *7*, 397–410.
- (50) Walsh, A. *Journal of Physical Chemistry C* **2015**, *119*, 5755–5760.
- (51) Yin, W.-J.; Shi, T.; Yan, Y. *Applied Physics Letters* **2014**, *104*, 063903.
- (52) Meggiolaro, D.; Motti, S. G.; Mosconi, E.; Barker, A. J.; Ball, J.; Perini, C. A. R.; Deschler, E.; Petrozza, A.; Angelis, F. D. *Energy and Environmental Science* **2018**, *11*, 702–713.
- (53) Motti, S. G.; Meggiolaro, D.; Martani, S.; Sorrentino, R.; Barker, A. J.; Angelis, F. D.; Petrozza, A. *Advanced Materials* **2019**, *31*, 1–11.
- (54) Yang, J. H.; Yin, W. J.; Park, J. S.; Wei, S. H. *Journal of Materials Chemistry A* **2016**, *4*, 13105–13112.
- (55) Eames, C.; Frost, J. M.; Barnes, P. R.; O'Regan, B. C.; Walsh, A.; Islam, M. S. *Nature Communications* **2015**, *6*, 2–9.
- (56) Azpiroz, J. M.; Mosconi, E.; Bisquert, J.; Angelis, F. D. *Energy and Environmental Science* **2015**, *8*, 2118–2127.

- (57) Sutter-Fella, C. M.; Miller, D. W.; Ngo, Q. P.; Roe, E. T.; Toma, F. M.; Sharp, I. D.; Lonergan, M. C.; Javey, A. *ACS Energy Letters* **2017**, 2, 709–715.
- (58) Motti, S. G.; Gandini, M.; Barker, A. J.; Ball, J. M.; Kandada, A. R. S.; Petrozza, A. *ACS Energy Letters* **2016**, 1, 726–730.
- (59) Nah, S.; Spokoyny, B.; Jiang, X.; Stoumpos, C.; Soe, C. M.; Kanatzidis, M. G.; Harel, E. *Nano Letters* **2018**, 18, 827–831.
- (60) Kobbekaduwa, K.; Shrestha, S.; Adhikari, P.; Liu, E.; Coleman, L.; Zhang, J.; Shi, Y.; Zhou, Y.; Bekenstein, Y.; Yan, F.; Rao, A. M.; Tsai, H.; Beard, M. C.; Nie, W.; Gao, J. *Nature Communications* **2021**, 12, 1–7.
- (61) Ma, Y.; Cheng, Y.; Xu, X.; Li, M.; Zhang, C.; Cheung, S. H.; Zeng, Z.; Shen, D.; Xie, Y. M.; Chiu, K. L.; Lin, F.; So, S. K.; Lee, C. S.; Tsang, S. W. *Advanced Functional Materials* **2021**, 31, 1–9.
- (62) Baumann, A.; V  th, S.; Rieder, P.; Heiber, M. C.; Tvingstedt, K.; Dyakonov, V. *The Journal of Physical Chemistry Letters* **2015**, 6, 2350–2354.
- (63) Patel, J. B.; Lin, Q.; Zadvorna, O.; Davies, C. L.; Herz, L. M.; Johnston, M. B. *The Journal of Physical Chemistry Letters* **2018**, 9, 263–268.
- (64) Wei, Z.; Guo, D.; Thieme, J.; Katan, C.; Caselli, V. M.; Even, J.; Savenije, T. J. *Nature Communications* **2019**, 10, 1–8.

2

MICROWAVE CONDUCTANCE TECHNIQUE

The core technique employed for the analysis of the different metal halide perovskites in this thesis is microwave conductance. As introduced in the previous chapter, different modes have been employed for the studies that will follow. For this reason, this chapter aims to provide a basic introduction of the technique and more specific details of the configuration used in different modes.



This chapter is partially based on:

Valentina M. Caselli et al., Charge Carriers Are Not Affected by the Relatively Slow-Rotating Methylammonium Cations in Lead Halide Perovskite Thin Films, *J. Phys. Chem. Lett.* 2019, 10, 5128-5134

Valentina M. Caselli and Tom J. Savenije, Quantifying Charge Carrier Recombination Losses in MAPbI₃/C60 and MAPbI₃/Spiro-OMeTAD with and without Bias Illumination, *J. Phys. Chem. Lett.* 2022,13, 7523-7531

Valentina M. Caselli et al., Traps in the Spotlight: How Traps Affect the Charge Carriers Dynamics in Cs₂AgBiBr₆ Perovskite, *Cell Reports Physical Science* 2022, 3, 101055

2.1. TRADITIONAL SET-UP: TIME-RESOLVED MICROWAVE CONDUCTANCE

MICROWAVE conductance is a technique based on the interaction of the electric field component of microwaves with a dielectric medium. In the microwave conductance set-up employed in this thesis, microwaves of frequencies ranging from 8.2 to 12.2 GHz are generated by means of a voltage-controlled oscillator and they are guided into a gold-coated brass X-band waveguide (see Figure 2.1).^{1,2} A horizontal grating at the end of the brass waveguide allows light to reach the sample, while reflecting the incoming microwaves. This side of the cell is then sealed with a UV grade quartz window, while the opposite side is sealed by foil. Two different types of cell have been used in the studies reported in this thesis: an "open cell" and a "cavity". In the latter, a 9-10 mm wide iris is located at the foil-sealed side. Its presence substantially enhances the sensitivity of the cell at the expense of the temporal resolution of the measurement, i.e. ca. 3 ns for an open cell and 18 ns for a cavity.² In both cases, the cell length, Λ , is designed to match the length of a full oscillation of the microwave. During the measurements, the samples are placed at a distance of $3/4\Lambda$ from the front window; this position corresponds to one of oscillating field's maxima at resonant frequency, as schematically represented in Figure 2.1.^{1,2}

The incident and reflected microwaves are separated by a circulator, and the latter are detected by a Schottky barrier diode and converted into a DC signal (see Figure 2.1).¹ During a time-resolved measurement, this signal is subtracted by an offset regulator. The remaining laser-induced AC signal is then amplified and stored in a digital oscilloscope triggered by a photodiode that is directly illuminated by the laser.^{1,2} The lasers employed for photoexcitation during the time-dependent measurements are 3-5 ns full width at half maximum (FWHM) Nd:YAG lasers whose wavelength can be tuned in the 240-2400 nm range. The lasers operate at a repetition rate of 10 Hz and the intensity of the irradiation can be tuned by means of metal-coated neutral density filters. A schematic representation of the complete set-up and cavity configuration is shown in Figure 2.1. Unless specified otherwise, the time-resolved microwave conductance (TRMC) measurements presented in the following chapters have been performed under pulsed laser illumination only without alterations of the set-up described above.

2.2. WORKING PRINCIPLE

The interaction of microwaves with a dielectric medium can result in an attenuation and/or phase shift of the microwave power. These changes can be related to variations in the real and imaginary component of the conductivity, σ , respectively, of the conducting medium. For the following description, and for most of the studies presented in this thesis, only the changes in the real conductivity, $\Delta\sigma_{Re}$, will be considered. Hence, the notation $\Delta\sigma$ used from now on will refer to $\Delta\sigma_{Re}$ only, unless clearly specified.

The electrical conductivity of a material depends on product of the concentration of free charge carriers, i.e. electrons and holes, and their respective mobilities, according to:

$$\sigma = e(n_e\mu_e + n_h\mu_h) \quad (2.1)$$

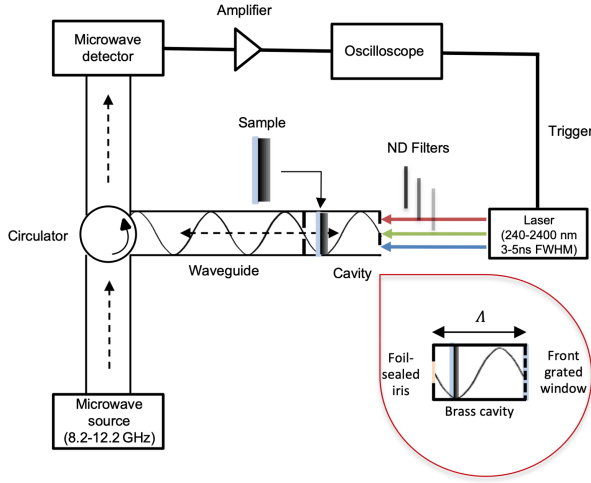


Figure 2.1: Schematic representation of the main components for the traditional microwave conductance set-up. The microwave cavity cell is enhanced on the bottom right corner to highlight the specific features mentioned in the main text.

where e represent the elementary charge, n_e and n_h the concentrations of electrons and holes, respectively, and μ_e and μ_h the corresponding mobilities. The changes in electrical conductivity, $\Delta\sigma$, due to photoexcitation in a TRMC experiment can be related to the attenuation of the detected microwave power, as

$$\frac{\Delta P}{P} = -K\Delta\sigma\beta L \quad (2.2)$$

where K is a pre-determined sensitivity factor, β the ratio of the long and short inner dimensions of the waveguide, and L the sample thickness. For samples of thickness much smaller than the microwave's wavelength, the conductance can be determined by integrating the conductivity change over the sample thickness, as per equation 2.3, resulting in the simplified relation in equation 2.4.

$$\Delta G = \beta \int_0^L \Delta\sigma(z) dz \quad (2.3)$$

$$\frac{\Delta P}{P} = -K\Delta G \quad (2.4)$$

2.3. DIFFERENT OPERATIONAL MODES

As mentioned, most of the measurements presented in the following chapters have been conducted under pulsed excitation only (TRMC). However, the microwave conductance technique can be also employed under different illumination conditions, which will be introduced in the following sections.

STEADY-STATE MICROWAVE CONDUCTANCE (SSMC)

Steady-state microwave conductance (SSMC) measurements can be performed in a resonant cavity in absence of pulsed (laser) illumination. This type of measurement is performed around the resonance frequency, f_0 , frequency at which a minimum in microwave power is detected (maximum microwave absorption). The resonance frequency depends on the geometrical cavity factors, i.e. length and inner dimensions of the cavity, and dielectric properties of the medium. An example of the resonance curve of an empty cavity is shown in Figure 2.2a, normalized by the incident power determined using a fully reflective end plate. With good approximation, the resonance curve, R , can be described by a Lorentzian function:

$$R(f) = \frac{R_0 + \left(\frac{2(f-f_0)}{\Delta W}\right)^2}{1 + \left(\frac{2(f-f_0)}{\Delta W}\right)^2} \quad (2.5)$$

where f represents the frequency, f_0 and R_0 are the frequency and depth of the curve minimum, respectively, and ΔW is the full width at half maximum (FWHM).

The conductivity and dielectric properties of a sample can be obtained from the analyses of SSMC results by fitting the resonance dips using a home-built software. This program numerically solves the Maxwell equations accounting for the dimensions and resonance properties of the cavity employed, as well as the dielectric properties and dimensions the sample loaded in it.³ An accurate fit, and therefore reliable results, can be obtained if the properties of the cavity and also characteristics of the sample substrate are known. To achieve this, distinct steps and analyses are performed, namely:

1. determine the resonance properties of the cavity by performing a frequency scan of the empty cell;
2. perform the scans at all relevant operation condition of the cell loaded with the substrate only, i.e. a quartz plate;
3. perform the measurements on the sample of interest.

The traces recorded in each stage are normalised by the incident microwave power, and fitted with the variables obtained during the step-by-step analysis. An example is provided in Figure 2.2b, where the resonance curves of a cavity loaded with quartz are shown at different temperatures. As it will be further discussed in Chapter 3, the shift to lower resonance frequencies with higher temperatures can be attributed to a slight enhancement in cavity length.⁴ The change in R_0 can be largely attributed to the lower surface conductivity of the inner walls of the cavity leading to higher losses at higher temperatures.

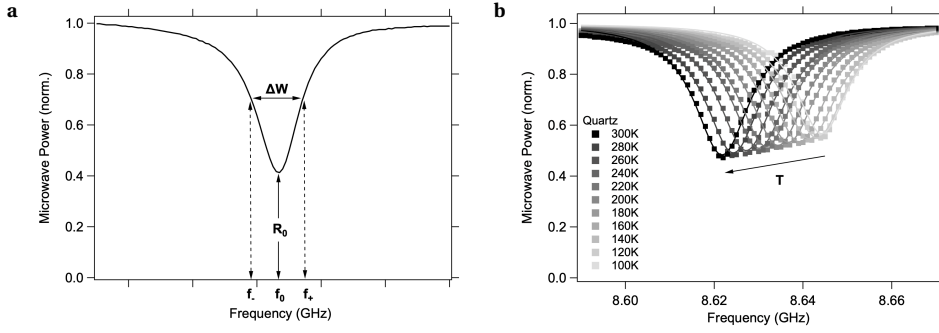


Figure 2.2: (a) Example of a normalized resonance curve of a microwave cavity. The FWHM, ΔW , resonance frequency, f_0 , and depth at the resonance position, R_0 , are shown. (b) Temperature-dependent normalized microwave power response for a cavity loaded with a bare quartz substrate at its resonance frequency.

SSMC measurements can be performed in the dark, as in the study presented in Chapter 3, or under steady-state illumination, as discussed in Chapter 5. From SSMC measurements conducted in the dark, relevant information about the background concentration of charge carriers can be obtained. Furthermore, as in the case presented in Chapter 3, dielectric losses due to dipolar reorientation can be quantified. Both are relevant for steady-state illumination SSMC analyses, where the concentration of excess charge carriers is determined under different illumination conditions.⁵

TIME-RESOLVED MICROWAVE CONDUCTANCE WITH BIAS ILLUMINATION

TRMC measurements in presence of continuous bias illumination (BI) can be performed by adding a LED lamp and a semitransparent mirror to the set-up. The mirror is placed in front of the microwave cell front window and it allows both laser (in transmission) and LED (in reflection) light to simultaneously reach the sample. The intensity of the LED can be tuned by manually varying its position with respect to the mirror.

In a previous study by Guo et al., continuous illumination has been used to extract the concentrations of excess charge carriers from SSMC measurements.⁵ To determine the number of photons absorbed by the sample during the measurements, the following procedure is applied. First the light intensity of the white light LED (see emission spectrum in Figure 2.3a) at the sample position is measured with a Silicon photodiode (Coherent, OP-2/LM-2 VIS). This intensity matches to the total number of integrated photons of the white light LED. Next, we integrated the number of photons over the wavelength emission range of the LED, however now corrected for the fraction of absorbed photons, F_A of the sample under examination. The absorbance spectrum of the MAPbI₃ in the example here reported is shown in Figure 2.3a. To relate the observed values of the LED light intensity to AM1.5 we corrected the solar emission spectrum for the LED spectrum and the absorbance spectrum of the photoactive layer. The spectra are shown in Figure 2.3b. After integration of this corrected emission spectrum over the wavelength, the intensity corresponding to AM1.5 is found.

The effect of the bias light on the charge carrier dynamics is investigated by performing measurements before, during and after exposition to the LED light. As introduced

in Chapter 1, light instability is a common issue in MHPs and it can deeply affect device performances. Therefore, obtaining detailed information on the charge carrier dynamics under continuous illumination is of great relevance to understand the loss mechanisms in perovskite-based solar cells. This issue is addressed in Chapter 5, where bias illumination is used to investigate the quality of MAPbI₃ interface with selective transport layers.

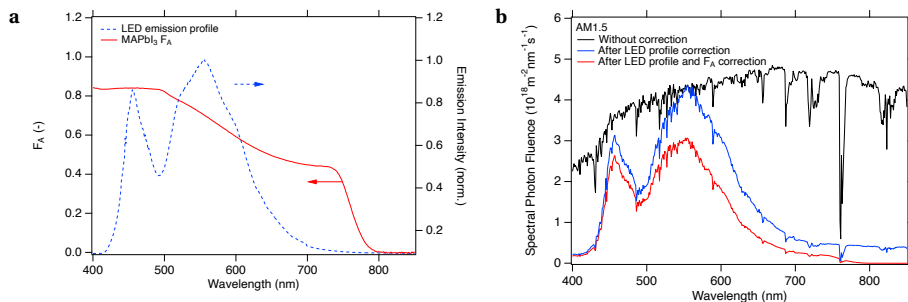


Figure 2.3: (a) Spectral absorption of a MAPbI₃ thin film (red), and emission spectrum of the LED lamp. (b) AM1.5 spectrum without any correction (black), corrected for the spectral emission of the LED lamp (blue), and subsequently by the spectral absorption of the sample, MAPbI₃ in this example (red).

DOUBLE-PULSE EXCITATION TIME-RESOLVED MICROWAVE CONDUCTANCE (DPE-TRMC)

In this thesis, a new TRMC-technique is introduced called the double-pulse excitation time resolved microwave conductance (DPE-TRMC) as displayed in Figure 2.4a. In this technique two Nd:YAG lasers, i.e. an Opotek Vibrant 355 LD+VIS and an Expla NT 340 laser, are oriented perpendicularly to one another and directed on the TRMC cell opening by means of a semitransparent mirror (ThorLabs 50x50mm, UVFS reflective, ND filter). The lasers are independently tuneable in wavelength and intensity by means of separate sets of ND filters. Furthermore, the use of optical shutters allow recording single pulse reference measurements during a DPE-TRMC experiment. A digital delay generator is used to set the delay time, t_D , between the two laser pulses ranging from 0 ns to 30 μ s.

During a DPE-TRMC experiment, the photoconductance signals ΔG_1 and ΔG_2 are first measured after each individual laser pulse, as shown in red and orange in the example reported in Figure 2.4b. The combined trace, ΔG_{DPE} (green in Figure 2.4b) is then recorded upon double pulse excitation. No unique data processing procedure can be specified beforehand for this technique since the results are strongly dependent on the sample's properties. Nonetheless, the changes induced by photoexciting the sample with two pulses can be better visualized by subtracting the ΔG_1 and ΔG_2 contributions from the ΔG_{DPE} signal. This results in a new trace, ΔG_{change} in Figure 2.4b, whose magnitude and decay are dependent on the changes of charge carrier dynamics in the sample of interest.

This technique is extremely useful to investigate the trapping processes and subsequent depopulation of electronic trap states in different materials. For the aim of this

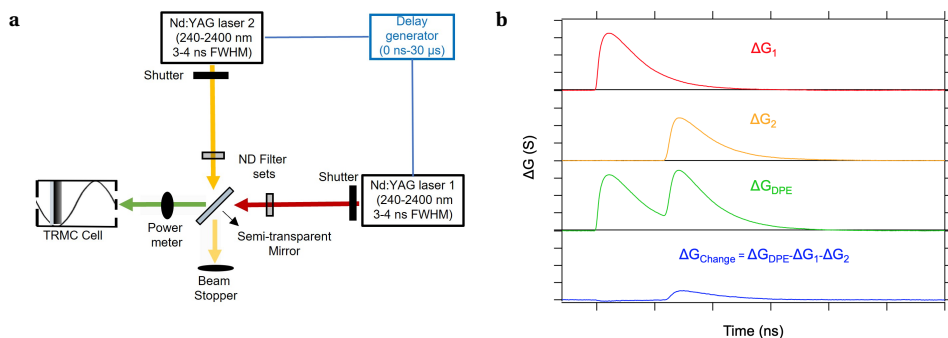


Figure 2.4: (a) DPE-TRMC schematic set-up representation and (b) example of the construction and analysis of a DPE-TRMC experiment.

thesis, perovskites of different composition have been investigated, some of which are reported on in Chapter 6. As schematically depicted in Figure 2.5, analyses that can be performed with DPE-TRMC involve:

- (i) investigation of trap state energy and population lifetime by performing a sub-bandgap excitation with the second pulse after free charge carriers have been generated by the first laser;
- (ii) investigation of charge carrier dynamic changes upon double excitation with identical wavelengths (see Chapter 6);
- (iii) study on the impact of phase segregation on charge carrier dynamics by exciting high and low bandgap regions separately.

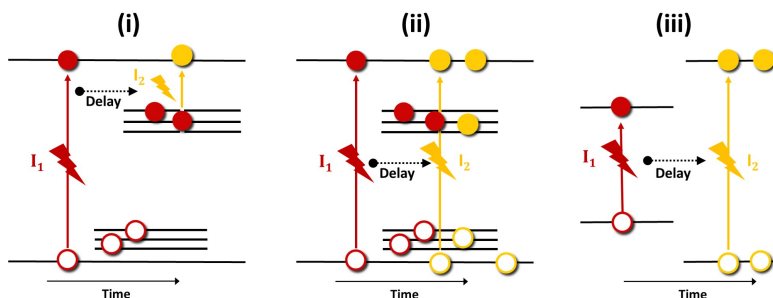


Figure 2.5: Examples of DPE-TRMC experiment diagrams for: (i) investigation of trap state energy and population lifetime (ii) investigation of charge carrier dynamic changes upon double excitation and (iii) impact of phase segregation.

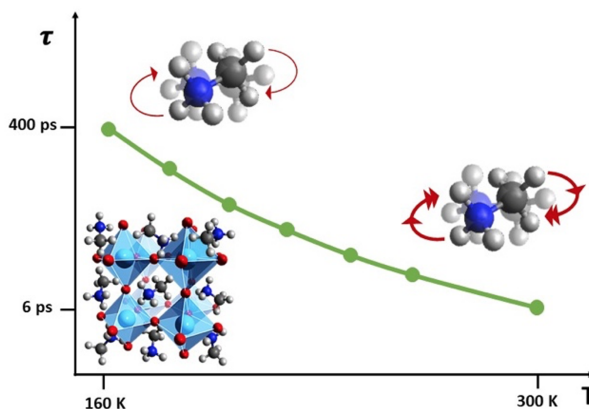
BIBLIOGRAPHY

- (1) Savenije, T. J.; Ferguson, A. J.; Kopidakis, N.; Rumbles, G. *Journal of Physical Chemistry C* **2013**, *117*, 24085–24103.
- (2) Savenije, T. J.; Guo, D.; Caselli, V. M.; Hutter, E. M. *Advanced Energy Materials* **2020**, *10*, 1–12.
- (3) Schins, J. M.; Talgorn, E. *Review of Scientific Instruments* **2011**, *82*, DOI: [10.1063/1.3600062](https://doi.org/10.1063/1.3600062).
- (4) Sarafis, P.; Nassiopoulou, A. G. *Nanoscale Research Letters* **2014**, *9*, 1–8.
- (5) Guo, D.; Caselli, V. M.; Hutter, E. M.; Savenije, T. J. *ACS Energy Letters* **2019**, *4*, 855–860.

3

DIELECTRIC LOSSES AND CHARGE CARRIER DYNAMICS: THE ROLE OF THE A-CATION

To begin the discussion on the charge carrier dynamics in different perovskites, in this chapter an in depth analysis on the dielectric properties of different metal halide perovskites (MHPs) is presented. From the analysis of the temperature-dependent dielectric behavior of four different MHP films in the gigahertz regime it resulted that the dipolar re-orientation of the MA cation does not affect charge carrier mobility and lifetime in MHPs.



This chapter is based on:

Valentina M. Caselli, Mathias Fischer, Daniele Meggiolaro, Edoardo Mosconi, Filippo De Angelis, Samuel D. Stranks, Andreas Baumann, Vladimir Dyakonov, Eline M. Hutter, and Tom J. Savenije, Charge Carriers Are Not Affected by the Relatively Slow-Rotating Methylammonium Cations in Lead Halide Perovskite Thin Films, J. Phys. Chem. Lett. 2019, 10, 5128-5134

3.1. METHYLAMMONIUM'S DIPOLE EFFECT ON MHPs PROPERTIES

IN the past few years, solar cells based on metal halide perovskite (MHP) semiconductors, with general structure ABX_3 , have emerged as promising low-cost alternatives to established semiconductors like silicon and CIGS. In addition, other applications such as light-emitting diodes, lasers and photodetectors were recently reported.¹ The success of MHP-based solar cells is due to their exceptional opto-electronic properties, such as high absorption coefficients, low exciton binding energies and long charge carriers lifetimes and diffusion lengths.^{2–5} Part of these properties can be attributed to the low densities of trap states and background charges.^{5,6} In addition it has been suggested that the large dipole moment of the methylammonium group (MA^+) in $MAPbI_3$ can result in the formation of ferroelectric domains by the collective motion of the MA^+ dipoles.^{7,8} This, although still under debate, might lead to enhanced exciton dissociation, polaron formation,⁹ reduced charge carrier recombination and defect screening.^{10–12} The rotational dynamics of the MA cation have been theoretically and experimentally studied.^{11,13–21} First studies on the rotational dynamics were carried out using IR¹⁹ and dielectric²² techniques. IR measurements on powders revealed a very rapid reorientation of the MA cation around the C-N axis with activation energies of 2.6 and 2.0 kJ/mol and relaxation times 1 and 0.7 ps for $MAPbI_3$ and $MAPbBr_3$, respectively.¹⁹ On the other hand, from dielectric measurements at 90 GHz, Poglitsch and Weber determined relaxation times of 5.37 and 2.73 ps for $MAPbI_3$ and $MAPbBr_3$, respectively.²² As extensively discussed by Gallop et al.¹², these values can be attributed to two different motions, namely a rapid wobbling and a slower reorientation of the MA^+ group. Raman spectroscopy has been more recently applied to study the dynamic (dis)order in perovskite materials. While the link between the (dis)order of the MA cation and the orthorhombic-tetragonal phase transition in MA^+ based MHPs appears to be clear,^{11,23} its influence on the lattice dynamics is still under debate.^{12,24} Furthermore, the impact of the MA^+ dipole on the formation of ferroelectric domains is still under discussion, although recent dielectric¹¹ and impedance spectroscopy (IS)²¹ studies reported no indication of formation of ferroelectric domains in these compounds. Theoretical modeling confirmed the limited stability of a possible ferroelectric $MAPbI_3$ phase at room temperature.^{20,25}

Despite the above mentioned studies on dipolar motion in MHPs, knowledge on dielectric properties in the GHz regime is still limited. Poglitsch and Weber²² and Anusca et al.¹¹ have shown the great impact of temperature on the dielectric properties of these materials, but both studies are missing information around 10 GHz. In this range, substantial changes in the temperature dependent dielectric behaviour related to the presence of the MA^+ dipolar reorientational motion can be expected. Moreover, to the best of our knowledge, no such study has been devoted on MHPs with different cations.

In this study we investigate the relationship between the perovskite constituents, temperature and the dielectric properties by means of microwave conductance (MC) measurements in the GHz regime. All these measurements are performed in the dark in contrast to standard TRMC measurements in which light induced changes in the real and imaginary part of the dielectric constant of many materials have been studied, re-

vealing the time dependent formation of e.g. charge transfer states,²⁶ excitons,²⁷ and mobile charges.⁶ The high quality factor of our cavity with resonance frequencies around 10 GHz ensures that even small changes in the dielectric properties by e.g. changing the constituents of the MHPs can be determined. Next, we prepared devices from the corresponding layers by using ITO and Au as contact layers and recorded the real and imaginary dielectric properties by impedance spectroscopy (IS) between 20 Hz and 2 MHz in the dark.

We performed MC measurements on the following spin-coated MHP layers: MAPbI₃, MAPbBr₃, FAPbI₃, CsPbI₃ and FA_{0.85}MA_{0.15}Pb(I_{0.85}Br_{0.15})₃ (FAMA). Interestingly, MA-based MHPs exhibited a strong temperature dependent dielectric loss in the GHz regime, which is absent for the FA- and Cs-based MHPs. With the low frequency IS measurements no appreciable temperature dependent changes were observed for both MAPbI₃ and FAPbI₃, meaning that the dielectric loss in the GHz regime is not related to background charges. Therefore, we attribute the changes in dielectric losses to the rotational motion of the MA⁺ dipoles. Activation energies for the rotational motion and corresponding temperature dependent relaxation times for MAPbI₃, MAPbBr₃ and FAMA were obtained by applying the Cole-Cole model²⁸ to our results. Despite the great impact of the dipolar orientation on dielectric properties in the GHz regime, no major implications for the charge carrier dynamics were found.

3.2. TEMPERATURE-DEPENDENT MICROWAVE CONDUCTANCE

MHP samples were fabricated on quartz or on patterned indium tin oxide (ITO) by the two step spin-coating procedure followed by a five minutes annealing step at 100°C. For optical and structural characterisation see Figure 3.A.1 in Appendix 3.A. For the MC technique a MHP layer on quartz was mounted in a temperature-controlled microwave cavity without any exposure to air. Apart from its superior sensitivity, the MC technique does not require electrical contacts. First a scan of the reflected microwave power is recorded by sweeping the frequency, ν , over a certain microwave range revealing a dip, which can be attributed to the formation of a standing wave pattern within the loaded cavity. Next, the microwave scans are normalised to a scan recorded by replacing the cavity with a fully reflecting end plate. In Figure 3.1 the normalised scans of MAPbI₃, MAPbBr₃, FAPbI₃, and FAMA are shown in a temperature range varying from 120 to 300 K. The gradual shift to lower frequencies upon heating combined with the increase in microwave absorption can be explained by changes of the cavity, i.e. expanding of the cavity length and enhanced losses in the metallic walls, respectively (see section 2.3 in Chapter 2 for more details). Most importantly, the scans of the MA-based samples are substantially different from those of FAPbI₃ and CsPbI₃. That is, up to 220 K for MAPbI₃ and up to 200 K for MAPbBr₃, we observe an increase in microwave absorption, which then decreases again at higher temperatures. For FAPbI₃ and CsPbI₃, on the other hand, the scans are very similar to those observed for a bare quartz substrate (compare Figure 3.A.2c and Figure 3.A.3a in Appendix 3.A to Figure 2.2b in Chapter 2).

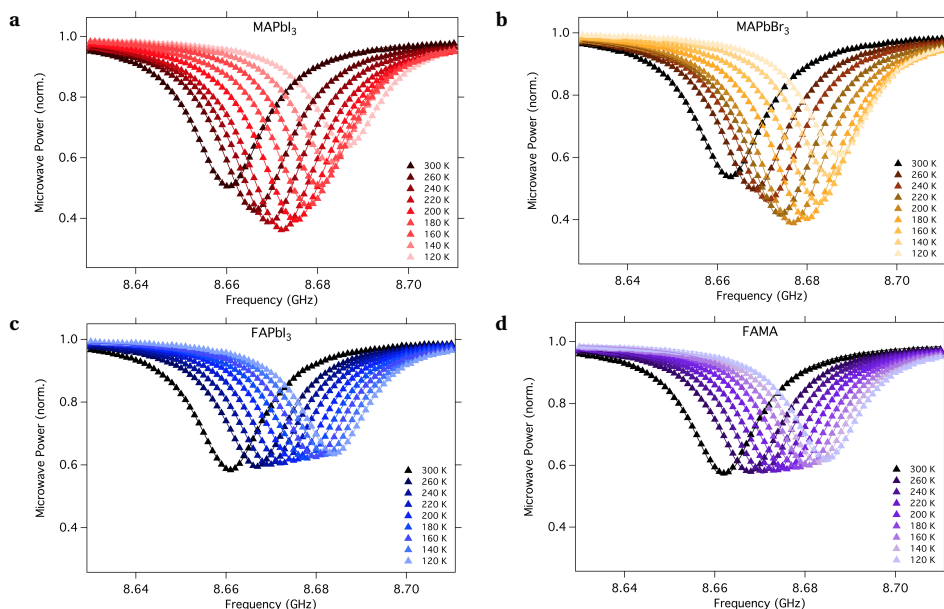


Figure 3.1: Normalized microwave power as function of frequency recorded at different temperatures for (a) MAPbI₃, (b) MAPbBr₃, (c) FAPbI₃ and (d) FA_{0.85}MA_{0.15}Pb(I_{0.85}Br_{0.15})₃ (FAMA). The solid lines are the results of the fits to the experimental data points (triangles).

The power scans in Figure 3.1 were modeled using a custom-built computer program, which numerically solves the Maxwell equations using the resonance characteristics of the cavity and the dielectric properties and dimensions of all media inside the cell as input.²⁹ The results of the fits are shown as solid lines in Figure 3.1, and the temperature-dependent conductivities are summarized in Table 3.A.1 in Appendix 3.A. The values of the imaginary dielectric constant, ϵ'' , are calculated from the real conductivities σ_{Re} by:

$$\sigma_{Re} = \omega \epsilon_0 \epsilon'' \quad (3.1)$$

where ω is the angular frequency and ϵ_0 the vacuum permittivity and plotted in Figure 3.2a. For both MA-based MHPs a clear maximum is observed, while FAPbI₃ and FAMA show almost no temperature dependence.

We note that absorption of microwaves by MHPs can have multiple origins, including the presence of mobile charge carriers, of mobile ions and/or dipolar reorientation related losses. For this reason, we conducted additional IS measurements on MAPbI₃ and FAPbI₃ over a wide frequency range, from 20 Hz to 2 MHz. At frequencies of 10 kHz and above ϵ'' is already influenced by series resistance resulting from the electrical contacts ITO and Au (see Appendix 3.B Figure 3.B.2). Therefore, the resulting relative value of ϵ'' as function of temperature at 1 kHz is shown for FAPbI₃ and MAPbI₃ in Figure 3.2b. In contrast to the MC results, the temperature dependence of ϵ'' determined by IS for MAPbI₃ and FAPbI₃ are similar and the specific maximum observed at 220 K in the GHz regime for MAPbI₃ (Figure 3.2a) is not present at kHz frequencies (Figure 3.2

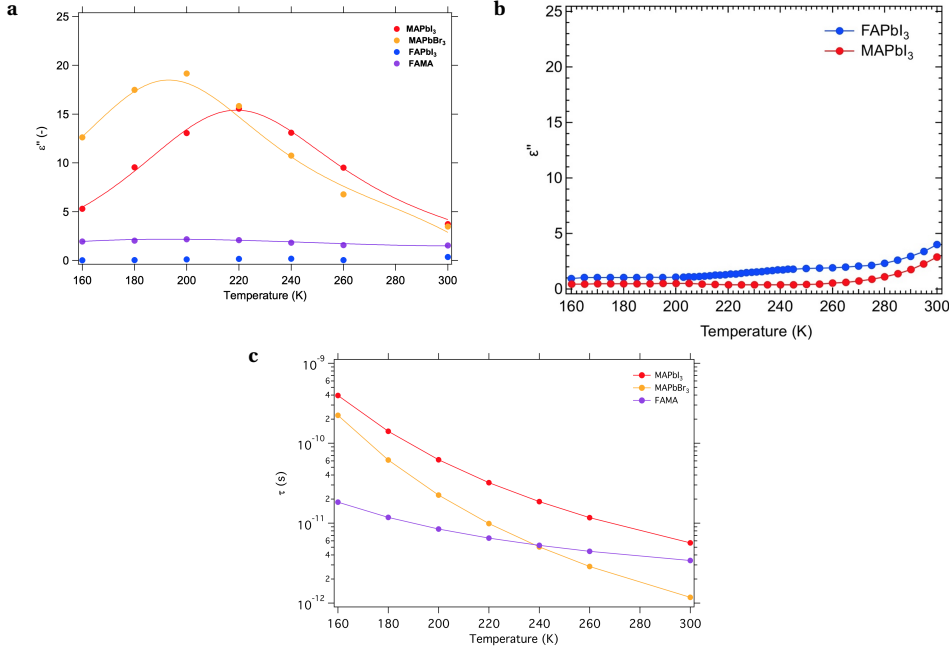


Figure 3.2: Imaginary part of the complex dielectric constant (a) from MC measurements at 8.6 GHz, and (b) at 1 kHz obtained by impedance spectroscopy. (c) Relaxation times for the MA⁺ containing MHPs.

b). In addition, we observe an increase of ϵ'' with temperature for both devices in the kHz regime, which we ascribe to temperature activated ionic conductivity and which is not observed in MC.^{30,31} These dissimilarities between the MC and IS measurements provide evidence against the hypothesis that temperature dependent dielectric losses in the GHz range are due to mobile species such as charges or mobile ions. The observation that only the MA-based MHPs show a considerably different dielectric behavior than that of a quartz reference substrate, implies that the dipolar reorientation of the MA dipolar cation is responsible for the distinctive temperature dependence of ϵ'' shown in Figure 3.2a.

3.3. DIELECTRIC CONSTANTS AND RELAXATION TIME

Previously the dielectric behavior of the MA⁺ based MHPs has been modelled successfully to extract relaxation times and activation energies of MA reorientation using the Cole-Cole model,²⁸ in which the complex dielectric constant ϵ^* is defined as:

$$\epsilon^* = \epsilon_\infty + \frac{\epsilon_S - \epsilon_\infty}{1 + (i\omega\tau)^{(1-\alpha)}} \quad (3.2)$$

where ϵ_∞ and ϵ_S represent the high frequency and static dielectric constants, respectively, τ the specific relaxation time, and α , a parameter reflecting the width of the relaxation time distribution. The specific expressions for the real and imaginary part are

given in Appendix 3.A. The temperature dependence of the static and high frequency dielectric constants are derived from the IS (at 1 kHz) and MC (fitting in the range 8.6-8.7 GHz) measurements, respectively. Values are collected in Table 3.A.1 in Appendix 3.A. The relaxation time, τ is defined as:

$$\tau = \tau_0 \exp \frac{E_A}{k_B(T - T_0)} \quad (3.3)$$

in which, τ_0 is the relaxation time at high temperatures, E_A is the activation energy and T_0 the temperature at which the relaxation time could be considered as “infinitely slow”.^{32,33}

The experimental ϵ'' data points are fitted with the Cole-Cole equation and the resulting fits are added in Figure 3.2a showing excellent overlap for both MAPbI₃ and MAPbBr₃. We notice that for MAPbBr₃ the model is able to fit the results even in the cubic phase, ($T > 235$ K) with minimal discrepancies. By including a pre-factor of 0.41 for the FAMA sample, a proper match between experimental data points and fit is observed. This experimentally obtained number accounts for different factors, i.e. the reduced MA⁺ concentration in the sample, MA⁺-FA⁺ interactions and influence of mixed halide. Proper quantification of each of these factors in such complex system would require analyses and computational studies that go beyond the scope of this work. Despite the fact that τ of the FA cations should be in the same range as those of MA cations,¹² our analysis could not be applied to the FAPbI₃ results, due to the low magnitude of the dielectric losses. The difference with MA⁺ based MHPs can be explained on the basis of the reduced dipolar character of FA compared to MA cations, which implies a significantly reduced response to the applied electric field in the former system.

The temperature-dependent relaxation times for the MA⁺ based MHPs are shown in Figure 3.2c. Values at room temperature vary from 1 ps MAPbBr₃ to 6 ps for MAPbI₃ and are comparable to those previously determined on compressed powders by neutron scattering¹⁷ and dielectric measurements.^{11,22} Activation energies of 114, 135 and 37 meV were determined for the rotational motion of MAPbI₃, MAPbBr₃ and FAMA, respectively. The increase in E_A , from MAPbI₃ to MAPbBr₃ can be related to the increased hydrogen bonding strength and reduction of the octahedral cavity size,¹² as confirmed by XRD measurements (see Appendix 3.A Figure 3.A.1b). DFT calculations (see computational details section in Appendix 3.C) also confirm the stronger hydrogen bond between MA cations and the inorganic framework in MAPbBr₃ than in MAPbI₃ (0.06 eV difference in MA binding energy in favor of MAPbBr₃). Notably, FA experiences a higher rotational freedom compared to MA, as evidenced by ab initio molecular dynamics simulations,³⁴ consistent with the reduced activation energy for cation reorientation observed here. Despite such trend, the relaxation times are shorter at all temperatures for MAPbBr₃ in comparison with MAPbI₃. This has been previously reported by Selig et al.,³⁵ and has been attributed to a higher probability of large angle jumps combined with tilting of the inorganic cage.^{12,35} In contrast to previous findings,³⁵ for the mixed cation/halide, FAMA, we observe a much lower activation energy and relaxation times comparable to MAPbI₃ at room temperature. Furthermore, the relaxation times for FAMA do not show an evident temperature dependence, while, as expected, for both MAPbI₃ and MAPbBr₃, τ is considerably slowed down upon cooling. We attribute the FAMA results to a com-

combined effect of the rotational freedom in a larger crystal structure induced by the predominant presence of FA^+ cations, and a reduced dipolar interaction between the MA ions.

Next, we can use the experimentally found relaxation times, to calculate the frequency dependent values of ϵ'' using the Cole-Cole equation (see Figures 3.A.5 for ϵ' versus frequency). For MAPbI_3 and MAPbBr_3 , these extrapolations are shown as solid lines for different temperatures in Figure 3.3, crossing our experimental values at 8.6 GHz. Interestingly the maximum in dielectric loss shifts with temperature from frequencies much lower than 8.6 GHz to values much higher than 8.6 GHz. This behavior explains our observed peaks for the dielectric loss at 220 and 200 K for MAPbI_3 and MAPbBr_3 , respectively. The present interpretation agrees with the IS measurements; that is, ϵ'' continuously decreases with lower frequencies and drops below 2 at 4 kHz for all investigated temperatures (see Figure 3.B.3). Furthermore, at these frequencies we observe a huge difference in ϵ' between MAPbI_3 and FAPbI_3 (see Figure 3.B.2). Thus, we conclude that large, temperature-dependent variations in the real and imaginary part of the dielectric constant are observed specifically in the GHz regime for MA-based MHPs.

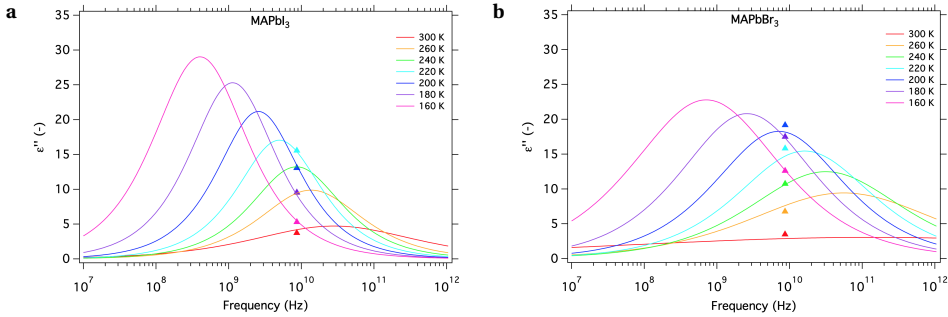


Figure 3.3: Calculated values of the dielectric losses at different temperatures versus frequency for (a) MAPbI_3 and (b) MAPbBr_3 by applying the Cole-Cole equation. The triangles indicate the experimental data points.

3.4. IMPACT ON CHARGE CARRIER DYNAMICS

As previously mentioned, the motion of the MA cation has been subject of research to understand the exceptional opto-electronic properties of MAPbI_3 . In particular, the possibility of enhanced charge carrier diffusion lengths as a result of weaker trapping,^{7,11} and slower recombination due to defect and electronic screening^{11,36} are still debated. Over the years we have investigated the charge carrier decay kinetics of several MHPs, differing in composition and fabrication method.^{37–40} On the basis of the results obtained, some of us previously concluded that the organic cation does not play a major role in the charge carrier kinetics.^{6,38} In agreement with these findings, charge/lattice response due to formation of large polarons was found to have a similar sub-ps time scale in both MA- and Cs-PbBr₃ perovskites.⁴¹ To verify if the rotational relaxation times affect the charge carrier dynamics, time resolved microwave photo-conductance (TRMC) traces are recorded at different temperatures and shown in Figure 3.4. Generally, all the MHP layers analyzed above (CsPbI_3 in Appendix 3.A), show similar trends on increas-

ing the temperature from 160 to 300 K: *i*) lower charge carrier mobilities and *ii*) shorter charge carrier lifetimes. A detailed discussion of these findings can be found in previously published papers.^{42,43}

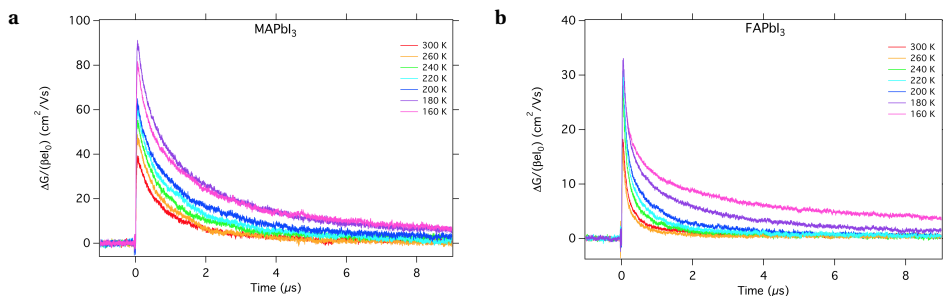


Figure 3.4: TRMC traces recorded on laser pulses with intensities of ca. $1\text{-}3 \times 10^9$ photons/cm² at 650 nm for (a) MAPbI₃, and (b) FAPbI₃.

With respect to the above discussion on the dielectric losses we can conclude the following: the temperature dependent TRMC traces confirm that the changes in the dielectric losses observed with MC for the MA-based MHPs are not due to mobile charge carriers. If the changes in dielectric loss were due to mobile electrons and/or holes, the decay kinetics of MA-based samples should have been greatly affected, especially around 200 to 220 K. However, such behavior is not observed for MAPbI₃ as shown in Figure 3.4. More importantly, the results reported here support the conclusion of a negligible impact of the nature of the A-site cation on the decay kinetics. In fact, despite the large change in dielectric loss, the temperature-dependent trend in mobility and lifetime of excess charge carriers in MA- and FA-based MHPs is very similar. On the other hand, no direct similarities can be found between MAPbI₃ and MAPbBr₃,^{40,42} for which charge carrier mobility and recombination are substantially different (Figure 3.4a and Figure 3.A.4a, respectively). Hence, from the present data no indications of reduced charge carrier recombination and/or defect screening by the MA is observed. A similar effect was previously discussed in the context of exciton screening, finding that the low-energy MA rotational dynamics barely affects the exciton binding energy in MAPbI₃, which is instead significantly affected by phonons in the THz region.⁴

3.5. CONCLUSIONS

In this work, we have investigated the temperature-dependent microwave conductivity of several metal halide perovskite materials in the dark. Interestingly, all MA-based samples showed high dark conductivities in the GHz regime with distinctive temperature variations. In contrast, no appreciable dark conductivity can be observed at frequencies of 1 kHz using IS measurements, which excludes ionic and electronic contributions. Therefore, we attribute the conductivities observed in the GHz regime to dielectric losses related to the rotation dynamics of the MA cation. Using the Cole-Cole model, we determined the activation energies and temperature-dependent relaxation times for different MA-based samples. On comparison of these results with the temperature-

dependent photoconductivity, no correlation between dipolar rotational dynamics and light-induced charge carrier dynamics in MHPs were found. These results show that the huge changes in the dielectric constant at GHz frequencies do not impact the carrier dynamics due to the different time scales involved. Hence, we conclude that the fast carriers do not feel the slow-moving MA cations, despite the fact that the latter contribute to the overall value of the dielectric constant.

SAMPLE PREPARATION

The FAPbI₃ precursor solution has been prepared starting from PbI₂ (600 mg), CH₅N₂I (FAI) (224 mg) and Dimethylsulfoxide (DMSO) (102 mg) dissolved in 1 mL N,N-Dimethyl-formamide (DMF). For the MAPbI₃ solution, we used PbI₂ (600 mg), CH₃NH₃I (MAI) (207 mg), Dimethylsulfoxide (DMSO) (102 mg) dissolved in 1 ml N,N-Dimethylformamide (DMF). Samples for IS measurements are fabricated on patterned indium tin oxide (ITO) covered glass substrates. Perovskite films were synthesized over a modified "Fast Deposition-Crystallization Procedure".⁴⁴ The Perovskite film was produced by spin coating the precursor solution at 4000 rpm for 30 s. During this step 200 uL Chlorobenzene was given on top of the wet film 10 s after the spin coating process has started, then the sub-strate was annealed for 15 minutes at 100°C (MAPI)/140°C (FAPbI₃). After forming the per-ovskite layer, a Polystyrene- layer was spin casted from o-Dichlorobenzene (DCB) solution (1 mg/mL) at 6000 rpm for 30 s, followed by 5 minutes annealing at 100°C. In the last step, the substrates were transferred into an evaporation chamber in order to apply a 60 nm gold (Au) layer as back contact. The same procedure has been followed for MC samples, only on bare quartz as substrate. The data reported in this study have been measured on quartz/perovskite only layers.

BIBLIOGRAPHY

- (1) Sun, J.; Wu, J.; Tong, X.; Lin, F.; Wang, Y.; Wang, Z. M. *Advanced Science* **2018**, 5, DOI: [10.1002/advs.201700780](https://doi.org/10.1002/advs.201700780).
- (2) Wolf, S. D.; Holovsky, J.; Moon, S. J.; Löper, P.; Niesen, B.; Ledinsky, M.; Haug, F. J.; Yum, J. H.; Ballif, C. *Journal of Physical Chemistry Letters* **2014**, 5, 1035–1039.
- (3) Savenije, T. J.; Ponseca, C. S.; Kunneman, L.; Abdellah, M.; Zheng, K.; Tian, Y.; Zhu, Q.; Canton, S. E.; Scheblykin, I. G.; Pullerits, T.; Yartsev, A.; Sundström, V. *Journal of Physical Chemistry Letters* **2014**, 5, 2189–2194.
- (4) Umari, P.; Mosconi, E.; Angelis, F. D. *Journal of Physical Chemistry Letters* **2018**, 9, 620–627.
- (5) Bi, Y.; Hutter, E. M.; Fang, Y.; Dong, Q.; Huang, J.; Savenije, T. J. *Journal of Physical Chemistry Letters* **2016**, 7, 923–928.
- (6) Hutter, E. M.; Eperon, G. E.; Stranks, S. D.; Savenije, T. J. *Journal of Physical Chemistry Letters* **2015**, 6, 3082–3090.
- (7) Frost, J. M.; Butler, K. T.; Walsh, A. *APL Materials* **2014**, 2, DOI: [10.1063/1.4890246](https://doi.org/10.1063/1.4890246).
- (8) Frost, J. M.; Butler, K. T.; Brivio, F.; Hendon, C. H.; van Schilfgaarde, M.; Walsh, A. *Nano letters* **2014**, 14, 2584–90.
- (9) Herz, L. M. *Journal of Physical Chemistry Letters* **2018**, 9, 6853–6863.
- (10) Ma, J.; Wang, L. W. *Nano Letters* **2015**, 15, 248–253.
- (11) Anusca, I.; Balčiūnas, S.; Gemeiner, P.; Svirskas, Š.; Sanlialp, M.; Lackner, G.; Fetschenhauer, C.; Belovickis, J.; Samulionis, V.; Ivanov, M.; Dkhil, B.; Banyas, J.; Shvartsman, V. V.; Lupascu, D. C. *Advanced Energy Materials* **2017**, 7, 31278–31286.
- (12) Gallop, N. P.; Selig, O.; Giubertoni, G.; Bakker, H. J.; Rezus, Y. L.; Frost, J. M.; Jansen, T. L.; Lovrincic, R.; Bakulin, A. A. *Journal of Physical Chemistry Letters* **2018**, 9, 5987–5997.
- (13) Mattoni, A.; Filippetti, A.; Saba, M. I.; Delugas, P. *Journal of Physical Chemistry C* **2015**, 119, 17421–17428.
- (14) Kanno, S.; Imamura, Y.; Saeki, A.; Hada, M. *Journal of Physical Chemistry C* **2017**, 121, 14051–14059.
- (15) Kanno, S.; Imamura, Y.; Hada, M. *Journal of Physical Chemistry C* **2017**, 121, 26188–26195.
- (16) Govinda, S.; Kore, B. P.; Bokdam, M.; Mahale, P.; Kumar, A.; Pal, S.; Bhattacharyya, B.; Lahnsteiner, J.; Kresse, G.; Franchini, C.; Pandey, A.; Sarma, D. D. *The Journal of Physical Chemistry Letters* **2017**, 3, [acs.jpclett.7b01740](https://doi.org/10.1021/acs.jpclett.7b01740).

- (17) Chen, T.; Foley, B. J.; Ipek, B.; Tyagi, M.; Copley, J. R.; Brown, C. M.; Choi, J. J.; Lee, S. H. *Physical Chemistry Chemical Physics* **2015**, *17*, 31278–31286.
- (18) Li, J.; Bouchard, M.; Reiss, P.; Aldakov, D.; Pouget, S.; Demadrille, R.; Aumaitre, C.; Frick, B.; Djurado, D.; Rossi, M.; Rinke, P. *Journal of Physical Chemistry Letters* **2018**, *9*, 3969–3977.
- (19) ONODA-YAMAMURO, N.; MATSUO, T.; SUGA, H. *Journal of Physical Chemistry Solids* **1990**, *51*, 1383–1395.
- (20) Quarti, C.; Mosconi, E.; Angelis, F. D. *Chemistry of Materials* **2014**, *26*, 6557–6569.
- (21) Hoque, M. N. F.; Yang, M.; Li, Z.; Islam, N.; Pan, X.; Zhu, K.; Fan, Z. *ACS Energy Letters* **2016**, *1*, 142–149.
- (22) Poglitsch, A.; Weber, D. *The Journal of Chemical Physics* **1987**, *87*, 6373–6378.
- (23) Quarti, C.; Grancini, G.; Mosconi, E.; Bruno, P.; Ball, J. M.; Lee, M. M.; Snaith, H. J.; Petrozza, A.; Angelis, F. D. *Journal of Physical Chemistry Letters* **2014**, *5*, 279–284.
- (24) Yaffe, O.; Guo, Y.; Tan, L. Z.; Egger, D. A.; Hull, T.; Stoumpos, C. C.; Zheng, F.; Heinz, T. F.; Kronik, L.; Kanatzidis, M. G.; Owen, J. S.; Rappe, A. M.; Pimenta, M. A.; Brus, L. E. *Physical Review Letters* **2017**, *118*, 1–6.
- (25) Stroppa, A.; Quarti, C.; Angelis, F. D.; Picozzi, S. *Journal of Physical Chemistry Letters* **2015**, *6*, 2223–2231.
- (26) Piet, J. J.; Schuddeboom, W.; Wegewijs, B. R.; Grozema, F. C.; Warman, J. M. *Journal of the American Chemical Society* **2001**, *123*, 5337–5347.
- (27) Fravventura, M. C.; Deligiannis, D.; Schins, J. M.; Siebbeles, L. D. A.; Savenije, T. J. *Journal of Physical Chemistry C* **2013**, *117*, 8032–8040.
- (28) Cole, K. S.; Cole, R. H. *Journal of Chemical Physics* **1941**, *9*, 341–351.
- (29) Schins, J. M.; Talgorn, E. *Review of Scientific Instruments* **2011**, *82*, DOI: [10.1063/1.3600062](https://doi.org/10.1063/1.3600062).
- (30) Azpiroz, J. M.; Mosconi, E.; Bisquert, J.; Angelis, F. D. *Energy and Environmental Science* **2015**, *8*, 2118–2127.
- (31) Frost, J. M.; Walsh, A. *Accounts of Chemical Research* **2016**, *49*, 528–535.
- (32) Küçükçelebi, H.; Durmuş, H.; Deryal, A.; Taşer, M.; Karakaya, N. *Applied Clay Science* **2012**, *62–63*, 70–79.
- (33) Davidson, D.; Cole, R. *Journal of Chemical Physics* **1951**, *19*, 1484.
- (34) Quarti, C.; Mosconi, E.; Angelis, F. D. *Physical Chemistry Chemical Physics* **2015**, *17*, 9394–9409.
- (35) Selig, O.; Sadhanala, A.; Müller, C.; Lovrincic, R.; Chen, Z.; Rezus, Y. L.; Frost, J. M.; Jansen, T. L.; Bakulin, A. A. *Journal of the American Chemical Society* **2017**, *139*, 4068–4074.
- (36) Milot, R. L.; Eperon, G. E.; Snaith, H. J.; Johnston, M. B.; Herz, L. M. *Advanced Functional Materials* **2015**, *25*, 6218–6227.

- (37) Hutter, E. M.; Sutton, R. J.; Chandrashekar, S.; Abdi-Jalebi, M.; Stranks, S. D.; Snaith, H. J.; Savenije, T. J. *ACS Energy Letters* **2017**, acsenergylett.7b00591.
- (38) Hu, Y. et al. *Advanced Energy Materials* **2018**, 1703057, 1–11.
- (39) Abdi-Jalebi, M. et al. *Nature* **2018**, 555, 497–501.
- (40) Guo, D.; Bartesaghi, D.; Wei, H.; Hutter, E.; Huang, J.; Savenije, T. *Journal of Physical Chemistry Letters* **2017**, 8, DOI: [10.1021/acs.jpclett.7b01642](https://doi.org/10.1021/acs.jpclett.7b01642).
- (41) Trinh, M. T.; Miyata, K.; Joshi, P. P.; Jones, S. C.; Angelis, F. D.; Mosconi, E.; Zhu, X.-Y.; Meggiolaro, D. *Science Advances* **2017**, 3, e1701217.
- (42) Hutter, E.; Gélvez-Rueda, M.; Osherov, A.; Bulović, V.; Grozema, F.; Stranks, S.; Savenije, T. *Nature Materials* **2017**, 16, 115–120.
- (43) Osherov, A.; Hutter, E. M.; Galkowski, K.; Brenes, R.; Maude, D. K.; Nicholas, R. J.; Plochocka, P.; Bulović, V.; Savenije, T. J.; Stranks, S. D. *Advanced Materials* **2016**, 28, 10757–10763.
- (44) Xiao, M.; Huang, F.; Huang, W.; Dkhissi, Y.; Zhu, Y.; Etheridge, J.; Gray-Weale, A.; Bach, U.; Cheng, Y. B.; Spiccia, L. *Angewandte Chemie - International Edition* **2014**, 53, 9898–9903.

APPENDICES

3.A. SAMPLE CHARACTERIZATION

XRD AND UV-VIS

The absorption measurements have been performed with a *PerkinElmer Lambda 1050 UV/vis/NIR* spectrophotometer. The results for the MHPs samples analyzed are shown in Figure 3.A.1a. X-ray diffraction patterns have been obtained with a *Brüker D8 diffractometer* (Co Kalfa-1, 1.78 Å) and are shown in Figure 3.A.1b.

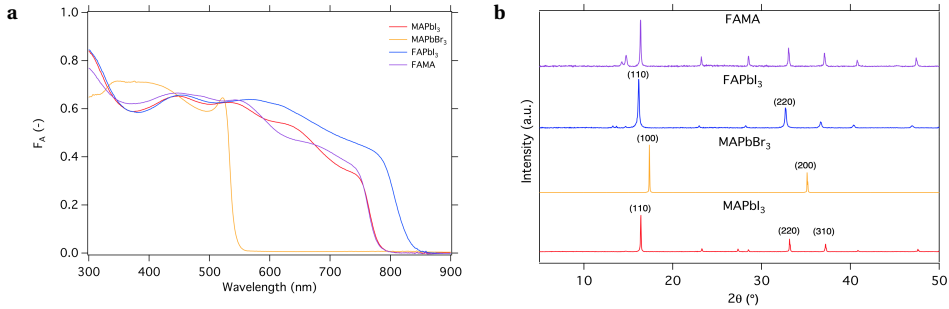


Figure 3.A.1: (a) Absorption spectra and (b) XRD patterns for MAPbI₃ (red), MAPbBr₃ (orange), FAPbI₃ (blue) and the mixed cation/halide FAMA (purple).

MICROWAVE CONDUCTANCE (MC)

Frequency scans have been recorded for all the samples at different temperatures. As it is possible to observe from Figure 3.A.2, only for methylammonium-based samples a minimum of R_0 is observed at temperatures 220 and 200 K for -I₃ and -Br₃. All the traces have been normalized with the frequency scan of a fully reflective end plate (results shown in Figure 3.1 in main text). The conductivity has been then evaluated by fitting the dips at the resonance frequency. The fitting model takes into account several parameters: dimensions of the cavity, thickness of the layers and quartz substrate, resistive losses in the cavity itself and dielectric properties of the media inside.

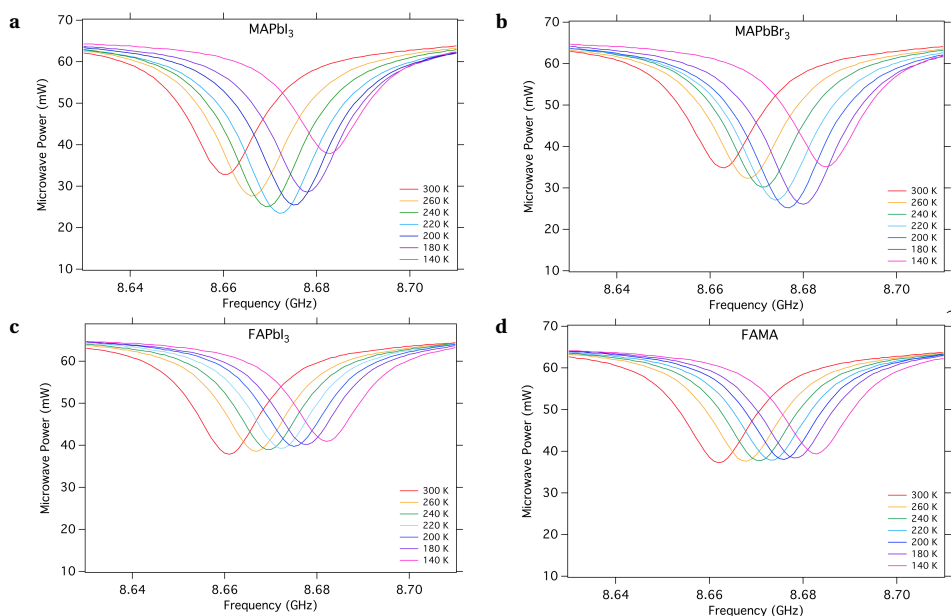


Figure 3.A.2: MC results showing the variation in detected microwave power at the resonance frequencies of different MHPs. Data recorded in the dark and at different temperatures for (a) MAPbI₃, (b) MAPbBr₃, (c) FAPbI₃ and (d) FA_{0.85}MA_{0.15}Pb(I_{0.85}Br_{0.15})₃ (FAMA).

Vapor deposited CsPbI₃ thin film has also been measured as the inorganic A-cation does not have any dipole. Results are shown in Figure 3.A.3a. TRMC traces upon photoexcitation at 650 nm are shown in Figure 3.A.3b.

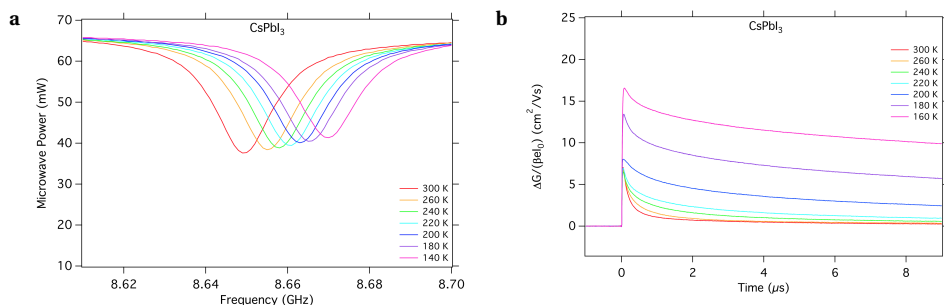


Figure 3.A.3: Temperature dependent (a) MC and (b) TRMC results of thin films of CsPbI₃. TRMC traces recorded upon photoexcitation at 650 nm (5×10^{10} photons/cm²).

The temperature-dependent TRMC traces of the MAPbBr₃ and FAMA samples are shown in Figure 3.A.4.

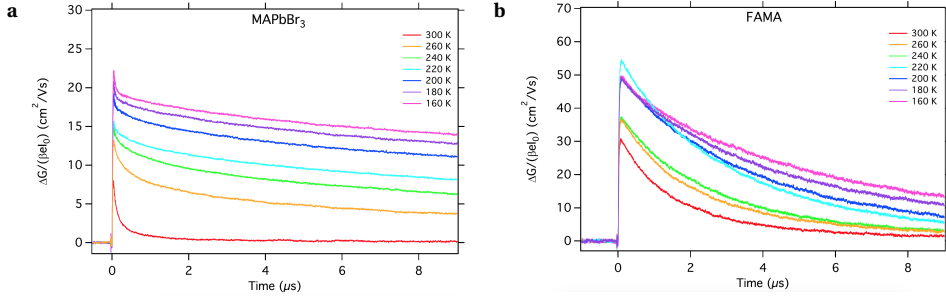


Figure 3.A.4: TRMC traces recorded on laser pulses with intensities of ca. $1\text{-}3 \times 10^9$ photons/cm² at 650 nm for (a) MAPbBr₃, and (b) FAMA.

DIELECTRIC MODEL EQUATIONS AND PARAMETERS

The dielectric response at high frequency has been modelled with the Cole-Cole equation that defines the complex dielectric constant as:

$$\epsilon^* = \epsilon_\infty + \frac{\epsilon_S - \epsilon_\infty}{1 + (i\omega\tau)^{(1-\alpha)}} \quad (3.A.1)$$

The real and imaginary part are given by:

$$\epsilon' = \epsilon_\infty + \frac{\Delta\epsilon [1 + (\omega\tau)^{1-\alpha} \sin(\frac{1}{2}\alpha\pi)]}{1 + 2(\omega\tau)^{1-\alpha} \sin(\frac{1}{2}\alpha\pi) + (\omega\tau)^{2(1-\alpha)}} \quad (3.A.2)$$

$$\epsilon'' = \frac{\Delta\epsilon (\omega\tau)^{1-\alpha} \cos(\frac{1}{2}\alpha\pi)}{1 + 2(\omega\tau)^{1-\alpha} \sin(\frac{1}{2}\alpha\pi) + (\omega\tau)^{2(1-\alpha)}} \quad (3.A.3)$$

Fits have been performed by applying Equation 3.A.3. The dielectric constants and alpha values are summarized in Table 3.A.1 for the MA-based samples analyzed.

Table 3.A.1: Temperature dependent dielectric constants and alpha values for MAPbI₃, MAPbBr₃ and FAMA.¹

T (K)	ϵ_S^*			ϵ_∞^{**}			α		
	MAPbI ₃	MAPbBr ₃	FAMA	MAPbI ₃	MAPbBr ₃	FAMA	MAPbI ₃	MAPbBr ₃	FAMA
300	50	60	29	30.14	15.96	8.78	0.46	0.78	0
260	60	65	28	29.98	17.55	9.26	0.22	0.54	0
240	65	70	27.5	29.98	17.95	10.30	0.18	0.41	0
220	70	80	27	29.96	22.40	11.38	0.13	0.27	0
200	75	90	27	29.94	23.66	12.55	0.07	0.33	0
180	95	100	27	29.96	24.85	15.14	0.09	0.36	0
160	105	115	27	29.96	22.95	18.14	0.19	0.40	0

Figure 3.A.5 reports the real dielectric constant variations as function of frequency in the temperature range analyzed. The results have been obtained by applying Equation 3.A.2, using the experimental and calculated values.

¹ * 1 kHz from IS analysis, ** Fitting results in GHz regime

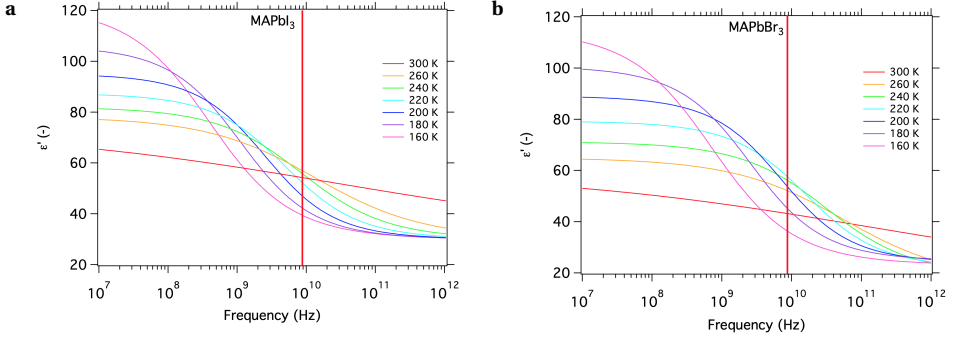


Figure 3.A.5: Calculated values of the real dielectric constant at different temperatures versus frequency for (a) MAPbI₃ and (b) MAPbBr₃ by applying Eq. 3.A.2. The red line represents the MC probing frequency.

3.B. IMPEDANCE SPECTROSCOPY

Impedance measurements were realized in a closed helium contact gas cryostat without exposure to ambient air using Agilent E4980A Precision LCR Meter. It is possible to link the complex valued impedance, Z , at a specific angular frequency, ω , to the dielectric function. Therefore, one can assume an ideal capacitor suffering from resistive losses and different models can be used, depending on where the losses occur: C_p and C_s models are described in Table 3.B.1.

Table 3.B.1: Description of series, parallel models. Note that if $\text{Re}(Z) = 0 \rightarrow C_s = C_p$, which means that if no resistive losses present both equations return the same result.

	Circuit-Model	Impedance	$C(\omega)$
C_s -Mode		$Z = R_s + \frac{1}{i\omega C_s}$	$C_s = \frac{-1}{\omega \text{Im}(Z)}$
C_p -Mode		$\frac{1}{Z} = \frac{1}{R_p} + i\omega C_p$	$C_p = \frac{1}{\omega} \text{Im}\left(\frac{1}{Z}\right) = \frac{1}{\omega} \text{Im}\left(\frac{Z^*}{ZZ^*}\right) = \frac{-\text{Im}(Z)}{\omega Z ^2}$

While R_p represents an intrinsic material parameter, R_s is considered to be a parasitic effect originating from wiring and contact resistances arising at high frequencies. In thin films like in our samples, the assumption of a plate capacitor of area A and thickness d is sufficiently fulfilled so that $C_p = \epsilon_r \epsilon_0 A / d$ holds. In this case the dielectric function is calculated from the C_p -Mode using:

$$\left(\frac{d}{i\omega A} \frac{1}{Z}\right) = \epsilon = \epsilon_r \epsilon_0 + i \frac{\sigma}{\omega} = \epsilon_0(\epsilon'_r + i\epsilon''_r) \quad (3.B.1)$$

We note, that this approach neglects the influence of the series resistance. In our samples this becomes only problematic for frequencies above ≈ 10 kHz so that measured ϵ''_r in this

range is then governed by R_s (see Figure 3.B.1).

The capacitance of the samples are obtained for phases close to $\pi/2$, when the real part of the impedance disappears (no resistive losses) so that C_p and C_s will lead to the same result. Under this condition ε_s can be determined precisely from the measured capacitance, independent of the underlying circuit model. Results are shown in Figure 3.B.1.

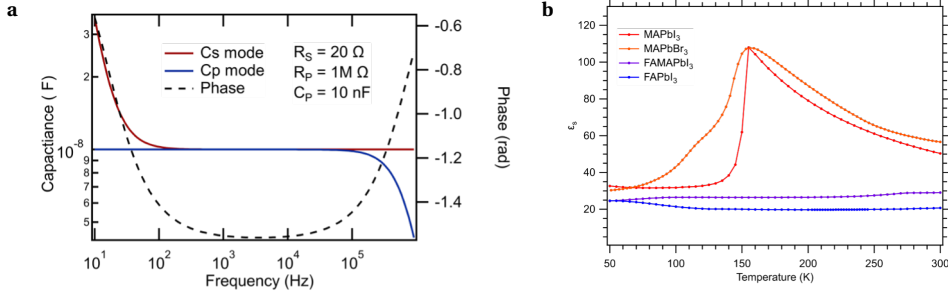


Figure 3.B.1: (a) Simulated results of a circuit containing both R_s and R_p measured in C_s and C_p mode. At intermediate frequencies the capacitance is determined correctly in both modes, owing to the fact that the phase angle is close to $\pi/2$. (b) The resulting ε_s for the different perovskites as function of temperature.

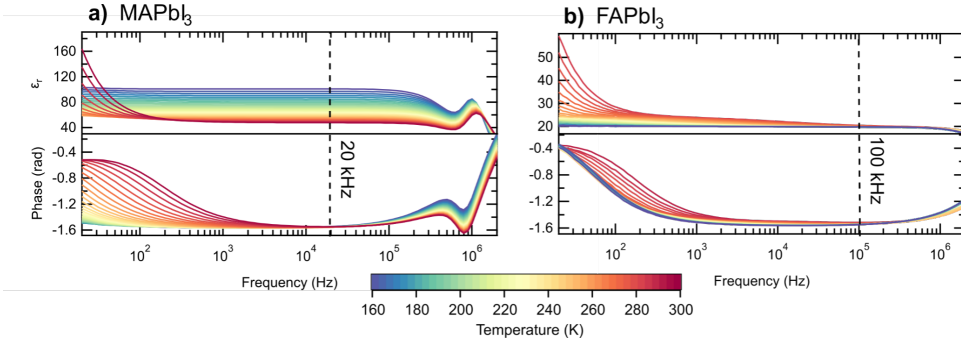


Figure 3.B.2: Measured dielectric function by IS for (a) MAPbI₃ and (b) FAPbI₃ at different temperatures.

Attempts to investigate ε_r'' for MAPbBr₃ and FAMA devices by IS failed due to low shunt resistances most probably caused by the formation of pin holes in the perovskite layer which made those devices unsuitable for a reliable study.

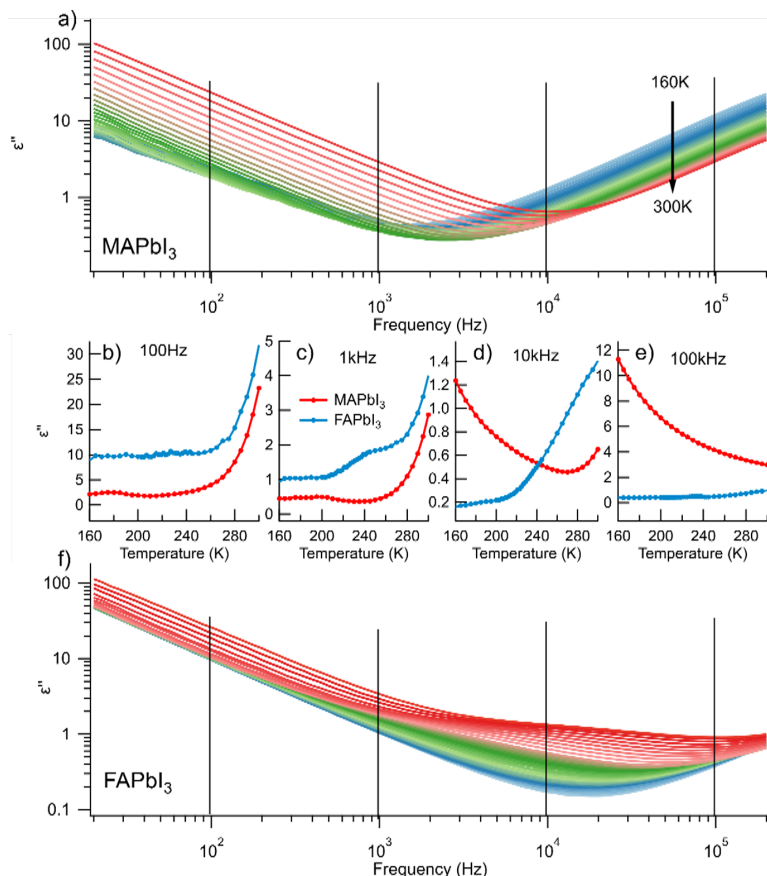
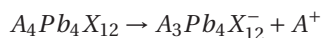


Figure 3.B.3: Measured imaginary part of the dielectric function by IS for (a) MAPbI₃ and (f) FAPbI₃ at different temperatures. The graphs (b), (c), (d) and (e) showing the temperature dependence of MAPbI₃ and FAPbI₃ at different frequencies. The minimum in (a) and (f) indicates where the series resistance starts to dominate the ac response.

3.C. COMPUTATIONAL DETAILS

Computational simulation have been carried out with the Quantum Espresso program package along with the PBE-GGA functional and ultrasoft pseudo potential with electrons from I 5s, 5p; Br 4s 4p, N, C, O 2s, 2p; H 1s; Pb, 6s, 6p, 5d shells explicitly included in calculations. For MAPbI₃ and MAPbBr₃ the experimental cell parameters for the tetragonal phase have been used, while for the FAPbI₃ the same cell and parameters of MAPbI₃ have been employed. Plane-wave basis set cutoffs for the smooth part of the wave functions and the augmented density were 25 and 200 Ry, respectively. The model used is the minimal 4-units (48 atoms) tetragonal system with a k-point sampling with a 4x4x4 grid.

To evaluate the interaction energy between the cation and the inorganic cage the ΔE of the following reaction has been calculated:



where A is the cation and X is the halogen.

The ΔE values were corrected considering the difference of the potential between the negative and neutral systems. As we can see in Table 3.C.1, the results show that, as expected, removing one A^+ cation is an unfavorable process ($\Delta E > 0$).

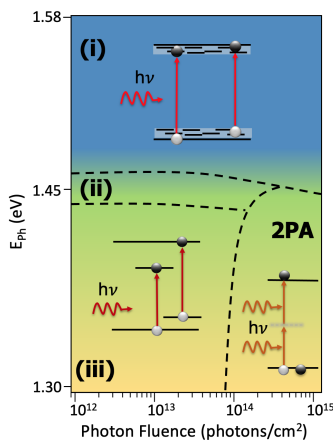
Table 3.C.1: Reaction energy in eV calculated for different cations (A = MA, FA) and halogen (X = I, Br). The values calculated with and without the potential correction have been reported.

A	X	ΔE (eV)	ΔE_{corr} (eV)
MA	I	9.61 (0.00)	10.18 (0.00)
	Br	9.75 (0.14)	10.24 (0.06)
FA	I	9.46 (-0.15)	10.01 (-0.17)

4

INTRA-BANDGAP REGIONS IN MAPbI₃: URBACH TAIL AND DEFECTS

In this chapter, the results of time-resolved microwave conductivity measurements upon sub-bandgap excitation in MAPbI₃ are presented. Three regimes have been identified from changes in the decay dynamics as a function of excitation energy and intensity: (i) band-like charge transport at photon energies above 1.48 eV; (ii) a transitional regime between 1.48 and 1.40 eV; and (iii) below 1.40 eV localized optically active defects ($8 \times 10^{13} \text{ cm}^{-3}$) dominate the absorption at low intensities, while two-photon absorption is observed at high intensities.



This chapter is based on:

Valentina M. Caselli, Zimu Wei, Marnix M. Ackermans, Eline M. Hutter, Bruno Ehrler, and Tom J. Savenije, Charge Carrier Dynamics upon Sub-bandgap Excitation in Methylammonium Lead Iodide Thin Films: Effects of Urbach Tail, Deep Defects, and Two-Photon Absorption, ACS Energy Lett. 2020, 5, 3821-3827

4.1. TRAP STATES AND URBACH TAIL

SINCE the discovery that metal halide perovskites (MHPs) are excellent materials for opto-electronic applications, such as photovoltaics,¹ the interest in these materials has grown rapidly. More recently, MHPs have been proven to be suitable candidates as active materials in photodetectors,² light emitting diodes,³ X-ray detectors,^{4,5} and even nonlinear photonics.⁶ Although these materials are typically produced via wet chemical techniques, semiconductors with a relatively low density of defects can be produced. However, to improve the efficiency of e.g. solar cells it is important to identify states within the bandgap. Via those states, non-radiative recombination can occur, leading to a reduced open circuit voltage (V_{OC}). The electronic quality of a photoactive material for solar cells application is often assessed by comparing its bandgap with the obtainable voltage, i.e. by the bandgap-voltage offset (E_{BG}/q) - V_{OC} .⁷ However, the absorption onset of a material is not always sharp due to the presence of defects. As such, an in depth study of its absorption edge and sub-bandgap absorption would lead to valuable knowledge to assess its suitability and potential for photovoltaic application.⁷

States in the bandgap are often classified as deep or shallow states, depending on whether trapped charges can be released by thermal energy or not. Experimental⁸⁻¹⁰ and in particular a huge amount of theoretical¹⁰⁻¹² work has been devoted to the origin of these defects and their ability to act as trapping centers for excess charge carriers. Their impact on recombination is to a large extent related to the energy difference between the band edges and the energetic position of the defect state.¹³⁻¹⁸ In addition to trap states, tailing of the bands by the formation of an exponential distribution of states close to the valence band (VB) maximum and conduction band (CB) minimum can occur. This leads to an exponential increase in the absorption just below the band-gap in semiconductor materials, which has been described by Urbach in 1953.¹⁹ This distribution of states has been attributed to various types of lattice disorder. These can be structural, e.g. due to intrinsic defects or induced via doping or stoichiometric variations, compositional, e.g. atomic substitution, or thermal, i.e. lattice vibrations.²⁰ If a material shows such an Urbach tail, the spectral and temperature dependence of its absorption coefficient, α , below the bandgap can be expressed as:

$$\alpha(h\nu, T) = \alpha_0 \exp \left[\frac{h\nu - E_{BG}}{E_U(T)} \right] \quad (4.1)$$

where α_0 is a constant, E_{BG} the bandgap energy, and E_U the Urbach energy.²¹ Previously the temperature dependence of E_U has been described by a summation of a temperature independent, static part, $E_U(0)$, and a temperature-dependent part, defined as:

$$E_U(T) = E_U(0) + \frac{2E_U(0)}{e^{\Theta_E/T} - 1} \quad (4.2)$$

in which Θ_E is the Einstein phonon temperature.²² The E_U has been characterized for a variety of semiconductors, including GaAs,²³ crystalline and amorphous Si.^{24,25} For MAPbI₃ the E_U has been determined by Fourier-transform photocurrent spectroscopy (FTPS),²² photothermal deflection spectroscopy (PDS),^{22,26} photoluminescence spectroscopy (PL),^{22,27} and external quantum efficiency (EQE) measurements.²⁷ The values of E_U range between 14-25 meV, which can be attributed to the MAPbI₃ sample quality and

technique applied. Interestingly, Ledinsky et al. reported a very small value of 3.8 meV for the static component, and a total value of 14.3 meV for E_U at room temperature.²²

We measured the photoconductance transients using the time-resolved microwave conductivity technique (TRMC) to investigate the behaviour of carriers in MAPbI₃ upon sub-bandgap excitation. As detailed in Chapter 2, one of the advantages of this technique is that we can record the charge carrier dynamics at different excitation wavelengths. Therefore we can relate the energetic position of the state within the bandgap and the nature of the excited charge carrier. In contrast to FTPS and EQE, the TRMC technique is contactless, thus unwanted contributions of the contacts or field interference to the photoconductivity signal are avoided. Contrarily to PL, but complementary to PDS, the TRMC technique allows us to investigate radiative and non-radiative decay kinetics or even electron transfer processes of the photo-excited charge carriers.

From our study on the charge carrier dynamics induced by sub-bandgap excitation ($E_{Ph} < E_{BG}$), we were able to identify three distinct regions for MAPbI₃. In the first, ranging between $1.48\text{ eV} < E_{Ph} < E_{BG}$, the carrier dynamics are identical to above-bandgap excitation. In this energy range we observed an exponential increase of the absorption coefficient, α , which can be related to the band tailing effect described by the Urbach rule.²⁰ For energies between $1.40\text{ eV} < E_{Ph} < 1.48\text{ eV}$, a transition from band tailing to defect-related absorption is observed. At $E_{Ph} < 1.40\text{ eV}$ and using low laser intensities, the photoexcitation and charge carrier dynamics are fully defect-related. Upon increasing the laser intensity, i.e. photon fluences $I_0 > 2 \times 10^{14}\text{ photons/cm}^2$ per pulse, two-photon absorption (2PA) occurs as we have described recently.²⁸ On deposition of an electron (C60) or hole (Spiro-OMeTAD) selective transport layer on top of MAPbI₃, we observe efficient charge transfer for photon energies as low as 1.44 eV. These results imply that for MAPbI₃, excess carriers occupying the Urbach tail still contribute to photocurrent generation.²⁷

4.2. SUB-BANDGAP LINEAR ABSORPTION REGION

To study the sub-bandgap absorption in MAPbI₃ thin films, we first performed TRMC measurements at low intensities to avoid two photon absorption (2PA).²⁸ The results for selected excitation energies are shown in Figure 4.1. On visible excitation at 1.90 eV the photoconductivity shows a fast rise due to the formation of mobile carriers, followed by a decay due to charge recombination or trapping as discussed and modelled before.²⁹ The initial magnitude scales with the excitation intensity, indicating that higher order decay processes are not affecting the initial signal. Interestingly, upon excitation at 1.50 eV, 80 meV below the bandgap ($E_{BG} = 1.58\text{ eV}$, as determined using a Tauc plot accounting for a direct allowed transition, Figure 4.A.2 in Appendix 4.A) we observe similar charge carrier dynamics, with lifetimes in excess of multiple microseconds (compare Figures 4.1a and 4.1b). This implies that even at 1.50 eV, mobile electrons and holes can be generated. Note that the photon fluences as well as the y-axes used in 4.1a and 4.1b are different because of the much higher absorption coefficient at 1.90 eV compared to 1.50 eV. More specifically, the laser intensities used for below-bandgap excitation (Figure 4.1b) are more than two orders of magnitude higher than for above the bandgap (Figure 4.1a). Nevertheless, the TRMC kinetics observed on excitation at 1.50 and 1.90 eV are comparable, implying the same decay processes are operating on the excess charge carriers.

On excitation at 1.46 and 1.44 eV, Figures 4.1c and 4.1d, a gradual transition can be observed. First of all, the TRMC signal size reduces. The substantial difference compared to the 1.50 eV excitation can be related to a much lower absorption. Moreover, as the number of excess carriers is considerably reduced, the impact of charge carrier trapping on the kinetics becomes more pronounced. At low photon fluences the charge carrier decay is less than 200 ns, while with higher intensities we observe a gradual increase in the signal lifetime, which indicates that the fraction of long-lived mobile carriers increases.

For excitation energies far below the bandgap the decay becomes faster and the long-lived component is no longer present. Interestingly, for $E_{ph} < 1.40$ eV, both magnitude and kinetics are the same at similar intensities (see Figures 4.1e and 4.1f). Moreover, it can be noted that the maximum signal is only linear at low intensities, but reaches a plateau at approximately 2×10^{13} photons/cm² per pulse. This indicates that there is a maximum number of possible excitations for the sub-bandgap linear absorption (SLA) process. These observations point to a generation mechanism related to the absorption from/to a finite number of localized defect states.

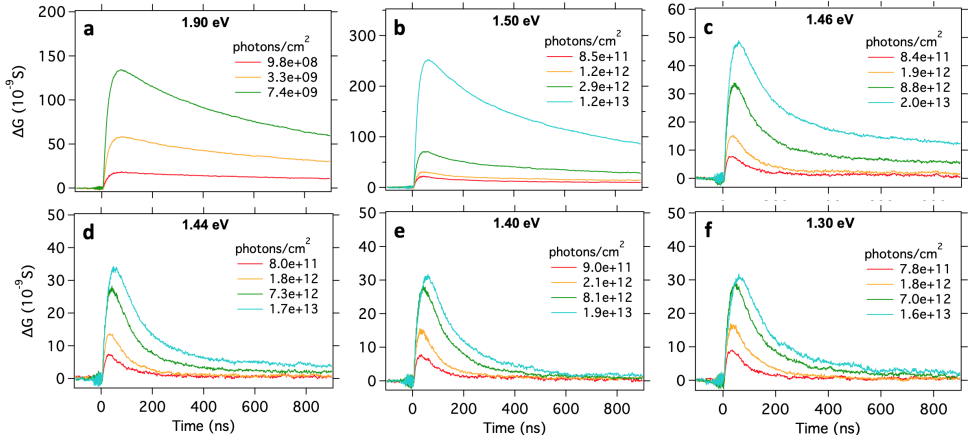


Figure 4.1: MAPbI₃ thin film photoconductance signals for excitations at different photon energies and laser intensities. Note that from (a) above the bandgap, to (b) below the bandgap the photon fluence is more than two orders of magnitude higher.

4.3. TWO PHOTON ABSORPTION REGION

In previous work, we have performed an in-depth study of the two photon absorption (2PA) process. Commonly the 2PA process has been investigated by Z-scan measurements, both in single crystals and thin films.^{30–32} However, the accuracy of this technique in the quantification of the 2PA absorption coefficient, β , is affected by the influence of free carrier absorption on the measured transmitted light. By probing the carriers by microwaves this issue is avoided.²⁸ For the sample shown in Figure 4.2, we experimentally find that at $I_0 > 2 \times 10^{14}$ photons/cm², charge carriers can be generated by the simultaneous absorption of two photons ($E_{ph}=1.30$ eV). This value is in agreement with our previous findings at similar excitation energies.²⁸ This process results in a gradual increase of the intensity-normalized photoconductance signal ($\Delta G/(\beta e I_0)$) with intensity, as shown in Figure 4.2 for $E_{ph} = 1.30$ eV. At this energy, we have previously determined a β coefficient of approximately 11 cm/MW,²⁸ which implies that above approximately 2×10^{14} photons/cm² the 2PA process will start to dominate the photo-conductance. Despite the low excitation energy, charges are now generated by the absorption of two photons, hence the combined energy is sufficient for band-to-band excitation. Most importantly, this 2PA process results in charge carrier decay kinetics similar to those we observed in Figures 4.1a and 4.1b, i.e. for above and close to the band-gap excitation, respectively.

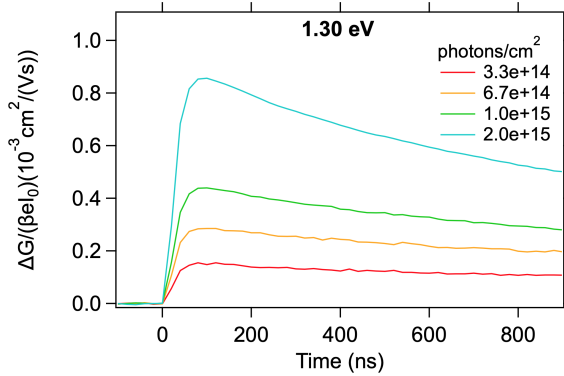


Figure 4.2: TRMC-intensity-normalized photoconductance signals of MAPbI₃ thin film upon 1.30 eV excitation at high laser intensities.

4.4. SURFACE AND BULK DEFECTS

In order to examine if an excitation close to the bandgap is due to surface defects, samples have been analyzed before and after a light soaking treatment (LST), performed as described by Brenes et al.³³ By this treatment passivation of surface defect states occurs.³³ As shown in Figure 4.3, the treated samples show an increase in lifetime to multiple microseconds, independent of the excitation energy (1.90–1.45 eV). The improved lifetime indicates a reduced recombination rate, which can be related to the passivation of the surface states, as reported before. In contrast, the signal magnitude is not affected by the LST. From this observation we conclude that the TRMC signal at 1.45 eV is most

likely due to sub-bandgap absorption in the bulk of the film, on which LST has no effect. If the absorption would originate from surface defects, passivation is expected to lower the height of the TRMC signal. The absence of any change in signal size hints again to a charge generation process in the bulk of the film. Moreover, this result confirms our previous conclusion that photo-excitations at this wavelength lead to band-like transport.

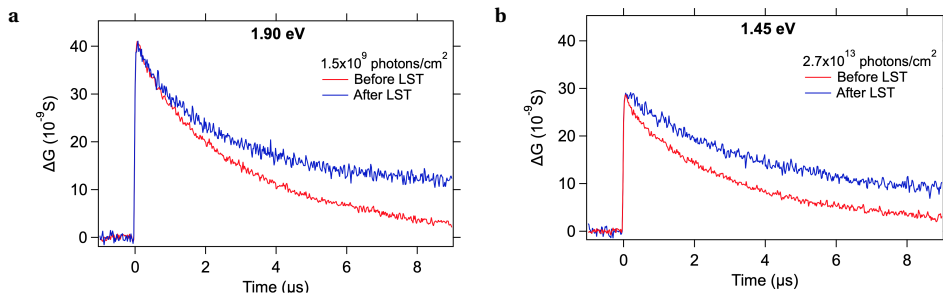


Figure 4.3: Photoconductance signal of MAPbI₃ thin film before and after light soaking treatment (LST) for excitations at (a) 1.90 eV at 1.5×10^9 photons/cm², (b) 1.45 eV at 2.7×10^{13} photons/cm².

4.5. CHARGE TRANSFER TO C60 AND SPIRO-OMeTAD

In order to obtain more knowledge on the nature of the excited carriers on sub-bandgap excitation, we extended our investigations to TRMC measurements on MAPbI₃ samples covered with a thin, thermally evaporated C60 layer, or a thin spin-coated 2,2',7,7'-Tetrakis[N,N-di(4-methoxyphenyl)amino]-9,9'-spirobifluorene (Spiro-OMeTAD) layer, acting as an electron- or hole-selective transport layer (ETL/HTL), respectively. As reported before, on optical excitation of such a bilayer system, CB electrons/VB holes can undergo electron/hole transfer to the specific TL.³⁴ Due to the relatively long response time of the TRMC measurement of 18 ns, the charge transfer process itself cannot be revealed but only the result of the charge transfer. As detailed in the Introduction, the observed TRMC signal is proportional to the product of the number of carriers and their mobility. Since the electron mobility in the organic layers is more than one order of magnitude lower than in the perovskite layer,^{35,36} the contribution of the transferred charges into the TLs to the total TRMC signal is small. Hence, the major part of the observed signal is due to the mobile charge carriers remaining in the perovskite layer. This implies that, provided charge transfer occurs the TRMC signal of the bilayer is lower in magnitude as compared to the single perovskite layer.^{34,37} A TL also affects the decay kinetics: since the electrons and holes are physically separated after transfer, recombination is slowed down in the bilayer systems.

TRMC traces are shown in Figure 4.4 for both MAPbI₃/C60 (Figures 4.4a, 4.4c, 4.4e) and MAPbI₃/Spiro-OMeTAD (Figures 4.4b, 4.4d, 4.4f), and results are normalized for the maximum signal observed for the bare MAPbI₃ layer. As shown in Figures 4.4a,b, excitation at 1.90 eV leads to very similar decay of the photo-conductance signals upon changing from the neat MAPbI₃ layer to a bilayer for both HTL and ETL, i.e. a clear reduction of the signal magnitude and elongation of the charge carrier lifetime. This in-

icates that both electron and hole transfer are efficient and that interfacial recombination occurs on longer timescales than the decay in the single layers. Most importantly, for $E_{ph} = 1.50$ eV (Figures 4.4c and 4.4d) both electron and hole transfer are almost as efficient as for above-bandgap excitation. If the sub-bandgap excitation would involve optical excitation from or to a localized defect state, the immobile charge carrier could not contribute to the TRMC signal, but also could not lead to charge transfer. In fact, only photo-excitations close to interface would lead to charge transfer. From our observation that charge transfer occurs efficiently, we conclude that for $E_{ph} = 1.50$ eV photo-excited charges are thermally excited into the transport bands from where charge transport and subsequent transfer can occur efficiently. The efficient electron transfer to an ETL is in contrast to previous studies using spin-coated ETLs,^{34,38} in which either no transfer³⁸ or fast interfacial recombination³⁴ was observed. Vacuum deposition of C60 as used in this work seems to provide a more reliable method for efficient electron collection.

4.6. URBACH ENERGY IN MAPbI₃

As introduced above, tailing of the bands can lead to an exponential absorption profile in the region just below the E_{BG} . Here, we calculated the photon energy dependence of the absorption coefficient from TRMC results in the following way. From the measured ΔG and the known value for the mobility, the number of excitations, n , can be derived. Accounting for reflection losses, we can determine the effective photon fluence, (I_{eff}), which after normalization yields the transmittance value, T_{TRMC} defined by

$$T_{TRMC} = \frac{I_{eff} - nL}{I_{eff}} \quad (4.3)$$

Taking the negative natural logarithm of T_{TRMC} and dividing by the thickness, yields the absorption coefficient, α . A more detailed description is given in Appendix 4.C. The natural logarithm of α as function of E_{ph} is shown in Figure 4.5, together with the results of the PDS measurements. The TRMC and PDS measurements show excellent agreement for $E_{ph} > 1.50$ eV, which substantiates our assumption that the charge carrier generation yield and mobility for absorbed carriers in this energy range is constant, independent of the excitation energy.

As mentioned, at $E_{ph} < 1.48$ eV the long-lived contribution to the TRMC signals becomes gradually smaller. By analysis of these TRMC traces we are able to differentiate between charge carriers resulting from excitation into the band tail (red squares in Figure 4.5) and charge carriers excited to localized defect states (red circles in Figure 4.5). This differentiation has been accomplished by comparing the TRMC traces, with those recorded at 1.50 eV (band-like transport) and at 1.40 eV (excitation from/to defect state), as detailed in Appendix 4.C. In this way, the value of α for $1.40 \text{ eV} < E_{ph} < 1.48 \text{ eV}$ can be determined more accurately, since we can account for the mobility of two (band like transport) or one charge carrier. From the inverse of the slope of the straight line in the log-linear plot, an Urbach energy of approximately 16 meV for MAPbI₃ was found from PDS measurements, in agreement with previously reported values,^{22,26,27} while 11.3 meV was determined from the corrected tail contribution of the TRMC signals. As it has been observed, comparing FTPS and PL results,²² the sensitivity of the technique applied and the evaluation procedure are limiting factors in the determination of the Urbach energy

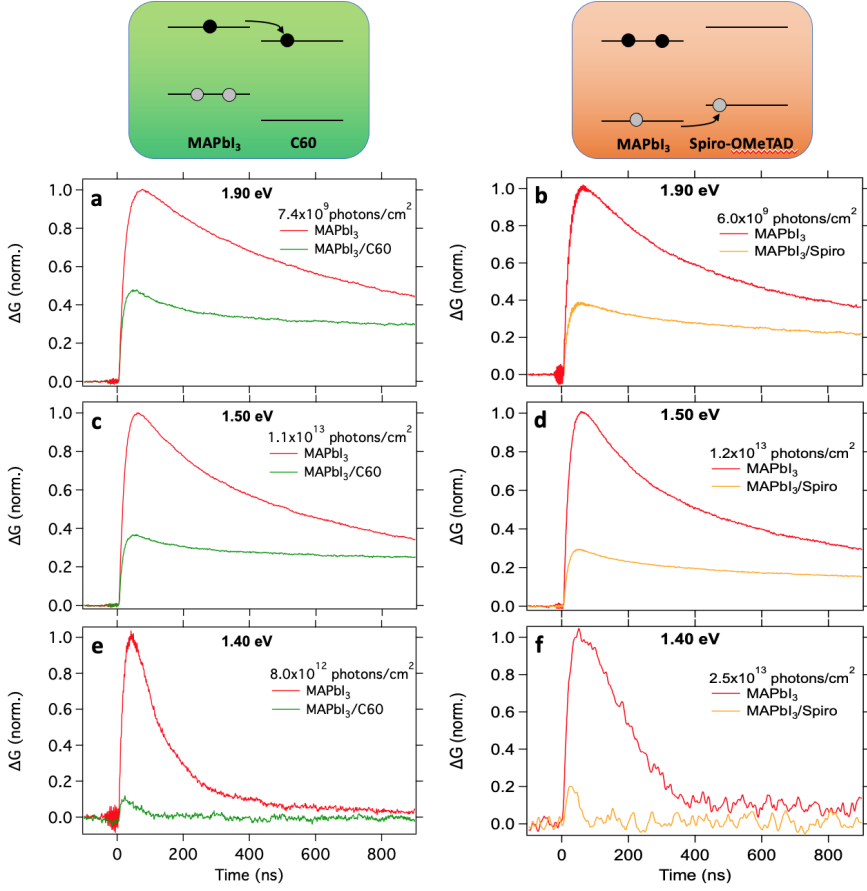


Figure 4.4: At the top schematic representations of the charge transfer processes are shown for MAPbI₃/C60 (left) and MAPbI₃/Spiro-OMeTAD (right). The process occurs within the instrumental response time (18 ns), leading to the respective MAPbI₃/C60 and MAPbI₃/Spiro-OMeTAD bilayers photoconductance signals upon front side excitation at (a,b) $E_{ph} = 1.90$ eV, (c,d) $E_{ph} = 1.50$ eV, and (e,f) $E_{ph} = 1.40$ eV.

in MAPbI₃ thin films. Owing to the higher sensitivity of our TRMC measurements, we have been able to investigate the Urbach tail region down to its lowest limit, disentangling the tail states and defects absorption contributions.

4.7. INTRA-BANDGAP REGIONS IN MAPbI₃

Our measurements show that MAPbI₃ has the following below-bandgap excitation regimes: (i) photo-excitation into the Urbach tail region ($1.48 \text{ eV} < E_{ph} < E_{BG}$) leads to charge carriers with band-like transport properties obeying the same decay processes as if they were the result of band-to-band excitation, (ii) the region $1.40 \text{ eV} < E_{ph} < 1.48 \text{ eV}$ marks a transition from band tailing to trap-related absorption, (iii) excitation below 1.40 eV is mainly due to absorption from/to a localized defect state.

The absorption profile below 1.40 eV is characterized by a small but constant absorption coefficient, due to a relatively small concentration of defect states, which can be optically accessed. On the basis of the TRMC signal we expect that the upper limit of the defect state concentration to be in the order of $8 \times 10^{13} \text{ cm}^{-3}$. Interestingly, this number is very close to the concentration of deep trap states (N_T) we find upon performing a global mathematical analysis on the TRMC traces recorded on above band gap excitation, as described previously by Hutter et al.³⁹ In this model (see Appendix 4.B, Figure 4.B.1) excess carriers decay by band-to-band recombination and in addition by deep trapping. By analyzing the traces at different intensities an estimate for N_T can be derived (see Appendix 4.B, Figure 4.B.2). In view of the similarities of this number and the number of carriers as deduced from our sub band-gap excitation measurements, we tend to conclude that these are the same defects. In view of the fast decay of these charges, these states are most likely detrimental for solar cell performance. Above 1.46 eV the Urbach tail starts to dominate the absorption coefficient. Excitation into this tail yields charge carriers with similar dynamics as above-bandgap excitation implying that charges excited into the tail are pushed towards the bands by thermal energy. These tail states are present within the bulk and cannot be affected by surface treatments. From the fact that efficient charge transfer towards both C60 and Spiro-OMeTAD is observed, we conclude that the Urbach tail, does not negatively affect the voltage or the photovoltaic performance of MAPbI₃ based solar cells. Furthermore, the similar efficiencies for electron and hole transfer upon excitation in the Urbach tail indicates that the tailing of the VB and CB is rather symmetric.

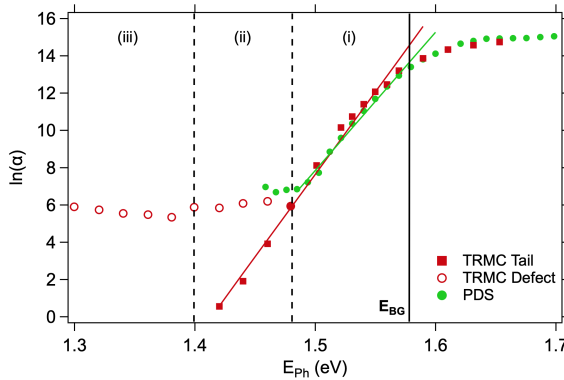


Figure 4.5: Logarithm of the absorption coefficient, α , determined by TRMC as function of photon energy. The solid black line corresponds to the bandgap energy, i.e. 1.58 eV for the MAPbI₃ film. The green and red fit lines have been used to determine the Urbach energy from PDS and TRMC measurements respectively.

4.8. CONCLUSIONS

Owing to its high sensitivity, the TRMC technique demonstrated to be a valid alternative to commonly established methods to investigate the sub-bandgap absorption properties of thin films. On basis of the changes in the charge carrier dynamics, and consecutive charge transfer studies into C60 or Spiro-OMeTAD we were able to identify different sub-bandgap absorption regimes. We demonstrated that excitation into the Urbach tail leads to mobile carriers that can be efficiently transferred into the TLs. These charge carriers are thermally excited into the transport bands. Surface passivation by a light soaking treatment did not affect the magnitude of the signals, but it improved the carrier lifetime. As such, we believe that band tail states cannot be considered as detrimental for photovoltaic performance. In contrast, absorption from/to states below the Urbach tail leads to immobile, quickly decaying charge carriers. This observation hints towards a defect-related absorption. On the basis of the TRMC results, we can estimate the deep defect concentration to be in the order of $8 \times 10^{13} \text{ cm}^{-3}$. This study provides a comprehensive overview of the generation and recombination processes in MAPbI₃ thin films, and opens the path to revealing the effective role of lattice vibrations and defects on charge carrier dynamics.

SAMPLE PREPARATION

For TRMC measurements, a 37 wt% MAPbI₃ precursor solution has been prepared dissolving MAI (synthesized following a standard procedure)⁴⁰ and Pb(Ac)₂•3H₂O (Sigma-Aldrich) powders (3:1 ratio) in DMF. The solution has been stirred for 1 hour, and then spin-coated onto plasma cleaned quartz plates at 2000 rpm for 45 s in a nitrogen filled glovebox. The films have been dried 15 minutes at room temperature and then annealed at 100°C for 5 minutes. The thickness of the film resulted to be $252 \pm 4 \text{ nm}$. A 30 nm C60 layer has been thermally evaporated on a quartz plate for characterization and on top of the spin-coated MAPbI₃. A 75 mg/mL solution of Spiro-OMeTAD in chlorobenzene has been spin-coated on a quartz plate for characterization and on top of the MAPbI₃ thin film at 1500 rpm for 45 s. The samples have been let to dry at room temperature for 30 minutes and then heated for 1 hour at 60°C.

The samples for PDS analysis have been prepared by spin-coating a stoichiometric solution of MAI (TCI, >99%) and PbI₂ (TCI, 99.99%, trace metals basis) at 1.1 M in a 4:1 v:v DMF (Sigma Aldrich anhydrous, >99%):DMSO (Sigma Aldrich anhydrous, >99.9%) solvent mixture on quartz substrates. Halfway during the 30 seconds of spin-coating at 9000 rpm, chlorobenzene (Sigma Aldrich anhydrous, >99%) was dropped onto the precursor solution as an anti-solvent.

BIBLIOGRAPHY

- (1) Kojima, A.; Teshima, K.; Shirai, Y.; Miyasaka, T. *Journal of the American Chemical Society* **2009**, *131*, 6050–6051.
- (2) Li, C.; Wang, H.; Wang, F.; Li, T.; Xu, M.; Wang, H.; Wang, Z.; Zhan, X.; Hu, W.; Shen, L. *Light: Science and Applications* **2020**, *9*, DOI: [10.1038/s41377-020-0264-5](https://doi.org/10.1038/s41377-020-0264-5).
- (3) Zou, Y.; Yuan, Z.; Bai, S.; Gao, F.; Sun, B. *Materials Today Nano* **2019**, *5*, 100028.
- (4) Mescher, H.; Schackmar, F.; Eggers, H.; Abzieher, T.; Zuber, M.; Hamann, E.; Baumbach, T.; Richards, B. S.; Hernandez-Sosa, G.; Paetzold, U. W.; Lemmer, U. *ACS Applied Materials and Interfaces* **2020**, *12*, 15774–15784.
- (5) Tsai, H.; Liu, F.; Shrestha, S.; Fernando, K.; Tretiak, S.; Scott, B.; Vo, D. T.; Strzalka, J.; Nie, W. *Science Advances* **2020**, *6*, 1–8.
- (6) Ferrando, A.; Pastor, J. P. M.; Suárez, I. *Journal of Physical Chemistry Letters* **2018**, *9*, 5612–5623.
- (7) Wolf, S. D.; Holovsky, J.; Moon, S. J.; Löper, P.; Niesen, B.; Ledinsky, M.; Haug, F. J.; Yum, J. H.; Ballif, C. *Journal of Physical Chemistry Letters* **2014**, *5*, 1035–1039.
- (8) Baumann, A.; Vöth, S.; Rieder, P.; Heiber, M. C.; Tvingstedt, K.; Dyakonov, V. *The Journal of Physical Chemistry Letters* **2015**, *6*, 2350–2354.
- (9) Motti, S. G.; Gandini, M.; Barker, A. J.; Ball, J. M.; Kandada, A. R. S.; Petrozza, A. *ACS Energy Letters* **2016**, *1*, 726–730.
- (10) Meggiolaro, D.; Motti, S. G.; Mosconi, E.; Barker, A. J.; Ball, J.; Perini, C. A. R.; Deschler, F.; Petrozza, A.; Angelis, F. D. *Energy and Environmental Science* **2018**, *11*, 702–713.
- (11) Yin, W.-J.; Shi, T.; Yan, Y. *Applied Physics Letters* **2014**, *104*, 063903.
- (12) Kim, J.; Lee, S. H.; Lee, J. H.; Hong, K. H. *Journal of Physical Chemistry Letters* **2014**, *5*, 1312–1317.
- (13) Kirchartz, T.; Krückemeier, L.; Unger, E. L. *APL Materials* **2018**, *6*, 100702.
- (14) Das, B.; Aguilera, I.; Rau, U.; Kirchartz, T. *Physical Review Materials* **2020**, *4*, 1–14.
- (15) Jin, H.; Debroye, E.; Keshavarz, M.; Scheblykin, I. G.; Roeffaers, M. B.; Hofkens, J.; Steele, J. A. *Materials Horizons* **2020**, *7*, 397–410.
- (16) Hall, R. *Phys. Rev.* **1951**, *83*.
- (17) Shockley, W.; Read, W. T. *Physical Review* **1952**, *87*, 835–842.
- (18) Motti, S. G.; Meggiolaro, D.; Martani, S.; Sorrentino, R.; Barker, A. J.; Angelis, F. D.; Petrozza, A. *Advanced Materials* **2019**, *31*, 1–11.
- (19) Urbach, F. *Physical Review* **1953**, *92*, 1324.

- (20) Studenyak, I.; Kranj, M.; Kurik, M. *International Journal of Optics and Applications* **2014**, 4, 76–83.
- (21) Baník, I.; Kubliha, M.; Labaš, V.; Lukovičová, J.; Pavlendová, G.; Šín, P. *AIP Conference Proceedings* **2016**, 1752, DOI: [10.1063/1.4955232](https://doi.org/10.1063/1.4955232).
- (22) Ledinsky, M.; Schönfeldová, T.; Holovský, J.; Aydin, E.; Hájková, Z.; Landová, L.; Neyková, N.; Fejfar, A.; Wolf, S. D. *Journal of Physical Chemistry Letters* **2019**, 10, 1368–1373.
- (23) Johnson, S. R.; Tiedje, T. *Journal of Applied Physics* **1995**, 78, 5609–5613.
- (24) Cody, G. D. *Journal of Non-Crystalline Solids* **1992**, 141, 3–15.
- (25) Cody, G. D.; Tiedje, T.; Abeles, B.; Brooks, B.; Goldstein, Y. *Physical Review Letters* **1981**, 47, 1480–1483.
- (26) Sadhanala, A.; Deschler, E.; Thomas, T. H.; Dutton, S. E.; Goedel, K. C.; Hanusch, F. C.; Lai, M. L.; Steiner, U.; Bein, T.; Docampo, P.; Cahen, D.; Friend, R. H. *Journal of Physical Chemistry Letters* **2014**, 5, 2501–2505.
- (27) Sutter-Fella, C. M.; Miller, D. W.; Ngo, Q. P.; Roe, E. T.; Toma, F. M.; Sharp, I. D.; Loneragan, M. C.; Javey, A. *ACS Energy Letters* **2017**, 2, 709–715.
- (28) Wei, Z.; Guo, D.; Thieme, J.; Katan, C.; Caselli, V. M.; Even, J.; Savenije, T. J. *Nature Communications* **2019**, 10, 1–8.
- (29) Savenije, T. J.; Guo, D.; Caselli, V. M.; Hutter, E. M. *Advanced Energy Materials* **2020**, 10, 1–12.
- (30) Zhang, R.; Fan, J.; Zhang, X.; Yu, H.; Zhang, H.; Mai, Y.; Xu, T.; Wang, J.; Snaith, H. J. *ACS Photonics* **2016**, 3, 371–377.
- (31) Kalanoor, B. S.; Gouda, L.; Gottesman, R.; Tirosh, S.; Haltzi, E.; Zaban, A.; Tischler, Y. R. *ACS Photonics* **2016**, 3, 361–370.
- (32) Saouma, F. O.; Park, D. Y.; Kim, S. H.; Jeong, M. S.; Jang, J. I. *Chemistry of Materials* **2017**, 29, 6876–6882.
- (33) Brenes, R.; Guo, D.; Oshero, A.; Noel, N. K.; Eames, C.; Hutter, E. M.; Pathak, S. K.; Niroui, F.; Friend, R. H.; Islam, M. S.; Snaith, H. J.; Bulović, V.; Savenije, T. J.; Stranks, S. D. *Joule* **2017**, 1, 155–167.
- (34) Hutter, E. M.; Hofman, J. J.; Petrus, M. L.; Moes, M.; Abellón, R. D.; Docampo, P.; Savenije, T. J. *Advanced Energy Materials* **2017**, 7, 1–8.
- (35) MacKenzie, R. C.; Frost, J. M.; Nelson, J. *Journal of Chemical Physics* **2010**, 132, DOI: [10.1063/1.3315872](https://doi.org/10.1063/1.3315872).
- (36) Tiazkis, R.; Paek, S.; Daskeviciene, M.; Malinauskas, T.; Saliba, M.; Nekrasovas, J.; Jankauskas, V.; Ahmad, S.; Getautis, V.; Nazeeruddin, M. K. *Scientific Reports* **2017**, 7, 1–9.
- (37) Bouduban, M. E.; Queloz, V. I.; Caselli, V. M.; Cho, K. T.; Kirmani, A. R.; Paek, S.; Roldan-Carmona, C.; Richter, L. J.; Moser, J. E.; Savenije, T. J.; Nazeeruddin, M. K.; Grancini, G. *Journal of Physical Chemistry Letters* **2019**, 10, 5713–5720.

- (38) Leijtens, T.; Eperon, G. E.; Barker, A. J.; Grancini, G.; Zhang, W.; Ball, J. M.; Kandada, A. R. S.; Snaith, H. J.; Petrozza, A. *Energy and Environmental Science* **2016**, 9, 3472–3481.
- (39) Hutter, E. M.; Eperon, G. E.; Stranks, S. D.; Savenije, T. J. *Journal of Physical Chemistry Letters* **2015**, 6, 3082–3090.
- (40) Kim, H. S.; Lee, C. R.; Im, J. H.; Lee, K. B.; Moehl, T.; Marchioro, A.; Moon, S. J.; Humphry-Baker, R.; Yum, J. H.; Moser, J. E.; Grätzel, M.; Park, N. G. *Scientific Reports* **2012**, 2, 1–7.

APPENDICES

4.A. OPTICAL AND STRUCTURAL CHARACTERIZATION

Absorption and reflection measurements have been performed with a *PerkinElmer Lambda 900 UV/vis/NIR* spectrophotometer, equipped with an integrating sphere. The resulting spectra are reported in Figure 4.A.1.

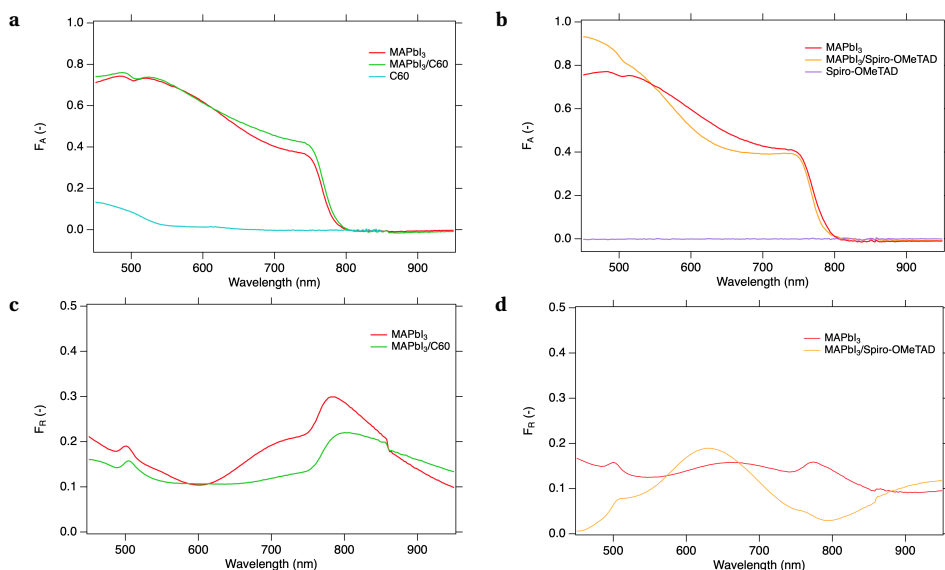


Figure 4.A.1: Fraction of absorbed light of the single and bilayers for sample of (a) MAPbI₃-C60 series and (b) MAPbI₃-Spiro-OMeTAD series. Fraction of reflected light of (c) MAPbI₃ and MAPbI₃/C60, and (d) MAPbI₃ and MAPbI₃-Spiro-OMeTAD thin films.

The optical bandgap has been determined from the Tauc plot (shown in Figure 4.A.2) for direct allowed transition, i.e. the r term in the exponent (cf equation 4.A.1) has a value of 0.5. By fitting the linear part (black line in Figure 4.A.2), a bandgap of 1.58 eV has been determined for the MAPbI₃ thin film, in agreement with previously reported values. The Tauc relation is commonly expressed as:

$$\alpha h\nu = A(h\nu - E_{BG})^r \quad (4.A.1)$$

Where α is the absorption coefficient, h the Planck's constant, ν the photon frequency, E_{BG} the bandgap energy, and A a constant called band tailing parameter.

X-ray diffraction patterns have been obtained with a *Brüker D8* diffractometer (Co K α -1, 1.78 Å) and are shown in Figure 4.A.3.

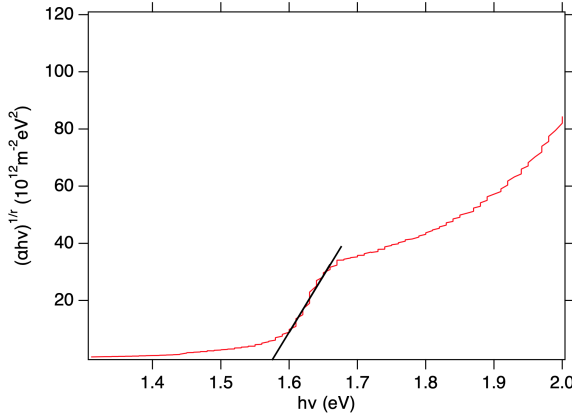


Figure 4.A.2: Tauc plot of MAPbI₃ thin film. The fitting line in the linear regime of the spectrum is shown in black.

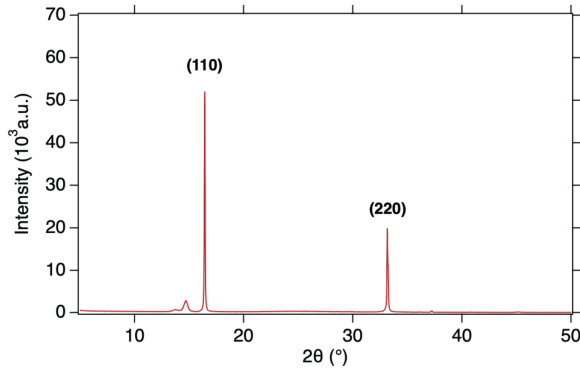


Figure 4.A.3: XRD diffraction spectrum of MAPbI₃ thin film.

4.B. TRMC TRACES FITS

The TRMC traces have been fitted accounting for charge carrier generation, and band-to-band and trap assisted recombination processes, as schematically depicted in Figure 4.B.1. The time-dependent electron, hole and trapped carriers concentrations have been fitted applying the set of equations 4.B.1-4.B.3. The results are shown in Figure 4.B.2 together with the corresponding TRMC traces. The extracted kinetic parameters are summarized in Table 4.B.1.

$$\frac{dn_e}{dt} = G_C - k_2 n_e (n_h + p_0) - k_T n_e (N_T - n_T) \quad (4.B.1)$$

$$\frac{dn_h}{dt} = -G_C + k_2 n_e (n_h + p_0) + k_D n_t (n_h + p_0) \quad (4.B.2)$$

$$\frac{dn_T}{dt} = k_T n_e (N_T - n_T) - k_D n_t (n_h + p_0) \quad (4.B.3)$$

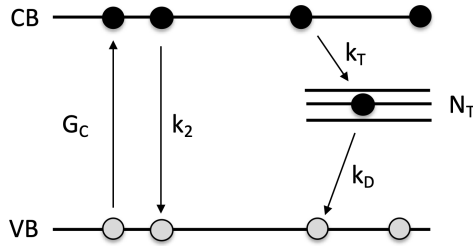


Figure 4.B.1: Schematic representation of charge carrier generation and recombination processes in the perovskite film.

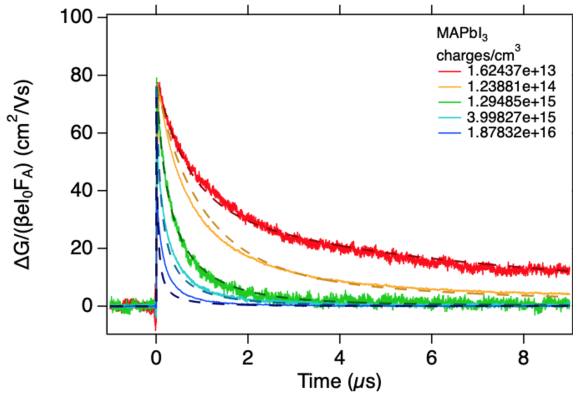


Figure 4.B.2: TRMC traces (solid lines) and fits (dashed lines) of the MAPbI₃ thin film from the MAPbI₃-C60 series.

Table 4.B.1: Kinetic parameters for the MAPbI₃ thin film from the MAPbI₃-C60 series.

	MAPbI ₃
k_2 ($\times 10^{-9} \text{ cm}^3 \text{ s}^{-1}$)	2.0
k_T ($\times 10^{-9} \text{ cm}^3 \text{ s}^{-1}$)	11
k_D ($\times 10^{-9} \text{ cm}^3 \text{ s}^{-1}$)	6.0
N_T ($\times 10^{14} \text{ cm}^{-3}$)	1.4
p_0 ($\times 10^{12} \text{ cm}^{-3}$)	9.0
μ_e ($\text{cm}^2 \text{ V}^{-1} \text{ s}^{-1}$)	90
μ_h ($\text{cm}^2 \text{ V}^{-1} \text{ s}^{-1}$)	70

4.C. MAPBI₃ BELOW THE BANDGAP ABSORPTION COEFFICIENT

The absorption coefficient for above and below the bandgap excitation has been derived from the results of the TRMC measurements. The maximum photoconductance value, ΔG_{MAX} , has been extrapolated from the initial rise of the signals, right after excitation. The response time of the instrument is 18 ns. In order to account for the effective number of photons passing through the sample, the signal has been normalized by the incident photon fluence, I_0 , corrected by a factor $(1-F_R)$, with F_R being the fraction of photons reflected at the sample surface (see Figure 4.A.1c). The effective incident photon fluence is referred to as I_{Eff} . If the mobility values for electrons and holes is known, we can determine the number photoexcited electrons/holes in the MAPBI₃ layer, n , as:

$$n = \frac{\Delta G_{MAX}}{e\beta I_{Eff} L \sum \mu} \quad (4.C.1)$$

Where e is the elementary charge, β a geometrical factor, $\sum \mu$ the sum of electrons and holes mobilities, and L the sample thickness. $\sum \mu$ has been determined from the analysis of above the bandgap excitation (see Table 4.B.1). Since the absorption below the bandgap is extremely low, it is possible to a homogeneous absorption profile though all the sample thickness. As such, a transmittance value based on TRMC results can be then calculated as:

$$T_{TRMC} = \frac{I_{Eff} - nL}{I_{Eff}} \quad (4.C.2)$$

The absorption coefficient is therefore:

$$\alpha_{TRMC} = -\frac{\ln T_{TRMC}}{L} \quad (4.C.3)$$

In the transition region, i.e. $1.40 < E_{ph} < 1.48$ eV, we have distinguished in between tail states and defects contribution to the signals. The distinction has been based on the decay kinetics of the traces recorded at ca. 2×10^{13} photons/cm² per pulse. More attention has been paid to the matching of the long living component. In fact, the long living signal is a clear indication of the contribution of absorption from/to tail states. On the other hand, the actual initial magnitude is strongly influenced by the incident photon fluence. Moreover, for short living signals, the rapid initial decay can be also affected by the instrumental set-up. In Figure 4.C.1 we show the results of the trace addition accounting for the tail states and defects absorption contribution for the trace recorded upon 1.46 eV excitation. The combined trace, dark green dashed line in Figure 4.C.1, has been obtained upon multiplying the 1.50 (red) and 1.40 eV (orange) traces by the pre-factors C1 and C2, respectively representing the contribution factors of tail states and defects absorptions. The values are summarized in Table 4.C.1 for all the traces recorded in the transition region.

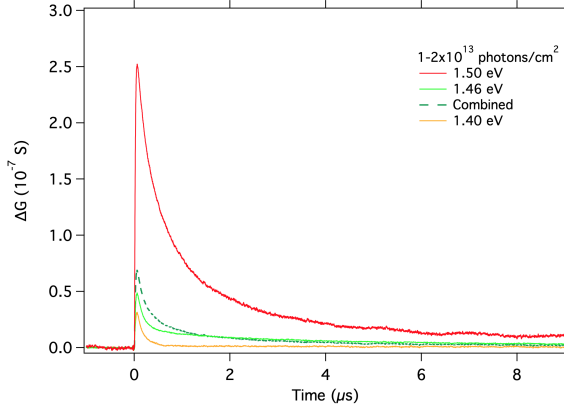


Figure 4.C.1: Original TRMC traces (solid lines) and result of the combination (dark green dashed line) accounting for tail (1.50 eV) and defects (1.40 eV) contributions to the 1.46 eV trace.

Table 4.C.1: C1 and C2 pre-factors at different photon energies.

	C1	C2
1.48 eV	0.6	0.4
1.46 eV	0.17	0.83
1.44 eV	0.03	0.97
1.42 eV	0.01	0.99

In order to account for the generation of only one mobile carrier due to defect absorption, the contribution to n has been estimated assuming a mobility of $\Sigma \mu/2$ (cf Eq. 4.C.1). This choice has been dictated by the fact that we cannot yet distinguish between electron and hole contribution. Nevertheless, the mobilities values for electrons and holes are not very different from each others (see Table 4.B.1). As such, the error in the estimation of n has been considered acceptable for the purpose of this analysis.

4.D. PHOTOTHERMAL DEFLECTION SPECTROSCOPY

For the photothermal deflection spectroscopy (PDS) measurement, the MAPbI₃ thin films on quartz were loaded into a cell containing degassed FC-72 (3M) liquid. The excitation source was monochromatic light from a tunable light source (*TLS-55-X300, ScienceTech*), which was focused on the sample. Excitations that recombine non-radiatively will lead to a temperature gradient near the excited spot. A chopper set at 23 Hz was placed between the light source and the sample. Since the refractive index of FC-72 is highly temperature-dependent, this heat gradient will result in a gradient in refractive index of the FC-72 liquid. A focused laser beam ($\lambda = 632$ nm) was used to probe this change in refractive index, by detecting its deflection. The resulting periodic displacement was detected using a quadrant detector (*Thorlabs PDQ80A*) and a lock-in amplifier (*SR830*). The data were corrected for the incident light intensity (I_0), which was measured simultaneously on a Si photodiode (*Thorlabs SM1PD1A*). The deflection scales

with the generated heat, which is a function of the fraction of absorbed photons (F_A), the incident photon energy (E_{Ph}) and the yield of heat versus radiative recombination ($1-Q_E$). Here, we assumed that thermalization to the bandgap ($\Delta E = E_{Ph} - E_{BG}$) always leads to heat emission. The deflection scales with the F_A according to:

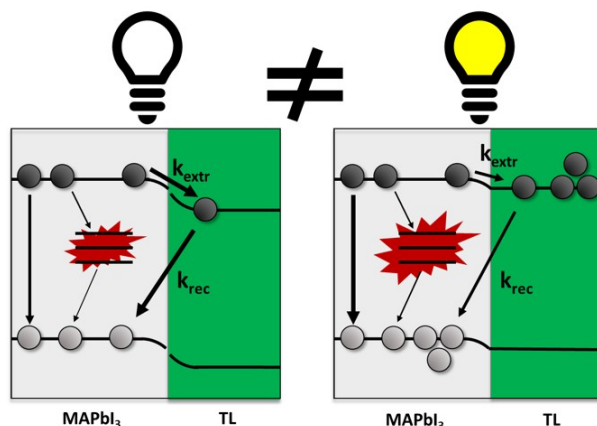
$$\frac{\text{deflection}}{I_0} = \frac{F_A(E_{Ph} - E_{BG}Q_E)}{E_{Ph}} \quad (4.D.1)$$

Hence, the deflection signal gives the wavelength-dependent trend in F_A . In order to obtain an absolute value, we scaled the PDS signal at 750 nm to the F_A determined from UV-VIS measurements in an integrating sphere.

5

RECOMBINATION LOSSES IN MAPbI₃ SINGLE AND BILAYERS UNDER BIAS ILLUMINATION

To further investigate the origin of the open circuit voltage losses in perovskite solar cells, in this study the charge carrier dynamics in bilayers of methylammonium lead iodide (MAPbI₃) with C60 or Spiro-OMeTAD are investigated with and without bias illumination (BI). Under BI, the density of deep traps increases in bare MAPbI₃, substantially enhancing trap mediated losses. This reversible process is prevented in a bilayer with C60 but not with Spiro-OMeTAD. While under BI extraction rates reduce significantly in both bilayers, only in MAPbI₃/Spiro-OMeTAD also interfacial recombination increases, substantially reducing the quasi-Fermi-level-splitting.



This chapter is based on:

Valentina M. Caselli and Tom J. Savenije, Quantifying Charge Carrier Recombination Losses in MAPbI₃/C60 and MAPbI₃/Spiro-OMeTAD with and without Bias Illumination, J. Phys. Chem. Lett. 2022,13, 7523-7531

5.1. REDUCING RECOMBINATION LOSSES IN PEROVSKITE SOLAR CELLS

METAL halide perovskite-based solar cells (PSCs) have improved significantly over the past years, reaching device efficiencies over 25%.¹ This impressive progress can be attributed to different optimization procedures. The perovskite layer properties have been perfected by optimizing the synthesis and deposition methods to obtain more stable and highly crystalline perovskite layers.^{1–4} At the device level, many approaches have been proposed to improve the interface properties between the perovskite absorber layer and the selective transport layers (TLs).⁵ Poor band-alignment, defect states at the interfaces, and instability of the used transport materials lead to a reduction in device performance, typically in the form of a reduction of the open circuit voltage (V_{OC}).⁶ To overcome these issues many different materials, organic and inorganic, have been examined as electron or hole transport layers.^{7–11} However, for rational design of efficient perovskite-based solar cells with a high V_{OC} , it is essential to obtain information regarding the rates for the charge extraction and recombination processes occurring at the perovskite/TL interfaces.

5.2. QUANTIFYING RECOMBINATION LOSSES AT THE INTERFACE: A NEW APPROACH

Different experimental methods have been used to characterise the interface of the perovskite layer with the TLs.^{5,8,12,13} Increasing photoluminescence yield and enhanced device stabilities and efficiencies have been often related to improved interfacial properties. Nonetheless, only a few research groups have been able to provide a quantitative analysis of the rate constants for charge extraction and interfacial recombination.^{14–19} In all these studies, the charge carrier dynamics has been investigated by means of time-resolved techniques using pulsed illumination sources. However, the kinetic parameters that can be extracted from a time-resolved analysis are not always representative of the dynamics under steady state illumination.²⁰ In addition, it has been reported that e.g. MAPbI₃ is unstable under continuous illumination. More specifically ion migration has been found to be the cause of several instability issues and hysteresis in the J-V curves of MAPbI₃-based devices.^{5,7,9,21} It can be expected that ion migration influences not only the charge carrier dynamics in the perovskite layer, but also the efficiency of the charge extraction process by the TLs.^{7,22} For these reasons, quantitatively studying the charge carrier extraction in perovskite/TL bilayers under steady-state illumination is relevant to fully characterize the interfacial processes.

In this study we provide a quantitative analysis to extract the rates of charge carrier extraction and recombination processes for methylammonium lead iodide (MAPbI₃) with selective TLs (see Figure 5.1a) under bias illumination (BI). C60 and Spiro-OMeTAD are chosen as electron transport layer (ETL) and hole transport layer (HTL), respectively, as they are the most commonly applied materials in the corresponding p-i-n and n-i-p cell structures. The dynamics are revealed by time-resolved microwave photoconductance (TRMC) measurements in presence or absence of continuous bias illumination with an intensity comparable to 0.3 suns. The analysis has been carried out by

first investigating the opto-electronic properties of the bare MAPbI₃ layer, followed by the MAPbI₃/C60 and MAPbI₃/Spiro-OMeTAD bilayers. The contactless TRMC measurements are performed over a broad intensity range from 10^{13} - 10^{15} cm⁻³, allowing us to quantify the various rate constants (see Figure 5.1a). Unless specified otherwise, the samples have been illuminated from the quartz side, referred to as back side (BS) in Figure 5.1b, in order to reduce parasitic absorption of BI by the TLs.

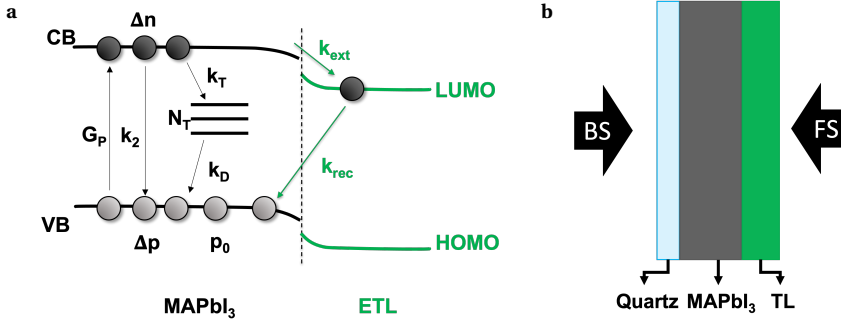


Figure 5.1: (a) Schematic representation of a MAPbI₃/ETL heterojunction and relevant kinetic processes occurring under illumination. The processes in the MAPbI₃ film are shown in black, while the charge carrier extraction and back recombination due to the presence of the ETL are shown in green. (b) Schematic representation of the sample configuration and excitation side. Front side (FS) excitation is performed by illuminating the sample from the perovskite/TL side, back side (BS) illuminating through the quartz substrate.

Confirming previous findings, we observe in MAPbI₃/C60 bilayers fast and efficient charge extraction by the C60 layer on pulsed illumination.^{8-10,23} However, while a bare MAPbI₃ layer shows fully reversible degradation under BI, the introduction of C60 suppresses this degradation process. On the other hand, the MAPbI₃/Spiro-OMeTAD bilayer is characterized by the formation of an internal electric field affecting the charge extraction. Furthermore, under BI the concentration defect states at the MAPbI₃/Spiro-OMeTAD interface increases substantially, which leads to partially irreversible changes in charge carrier dynamics. Finally, we calculate the concentrations of carriers under BI using the found kinetic parameters extracted from the TRMC analysis.²⁴ From these concentrations, quantification of the recombination losses and the quasi Fermi level splitting corresponding to the upper limit of qV_{OC} of a device are determined and discussed.

5.3. METHODOLOGY

MAPbI₃ thin films have been spin-coated onto quartz substrates following a previously reported procedure.²³ Optical and morphological characterisation is reported in Appendix 5.B. A 30 nm thick C60 layer has been added via physical vapor deposition, while Spiro-OMeTAD has been spin-coated on top of the MAPbI₃ film, as described at the end of this chapter. First the TRMC signals observed upon 650 nm photoexcitation of single and bilayers of MAPbI₃ (red) and MAPbI₃/TL (with ETL in green and HTL in orange) without BI are shown in Figures 5.2a,b. In agreement with our previous reports, two characteristics can be observed: the magnitude of the TRMC signal of the bilayers is reduced with respect to the signal of the bare MAPbI₃ and, at the same time, part of the photoconductance signal shows a slower decay.²³ Both these effects can be explained by efficient charge carrier extraction by the TLs. As the electron and hole mobilities in the TLs are more than one order of magnitude lower than in the perovskite layer, the extracted carriers have a negligible contribution to the measured photoconductance signal (see equations 2.1 and 2.2 in Chapter 2). This results in lower signals for the bilayers compared to the bare MAPbI₃ layer. Furthermore, if efficient extraction occurs the charge concentration of one type of carrier in the bands is less, reducing the decay by (non) radiative second order recombination, and thus long-lived photoconductance signals are observed.

The TRMC results obtained under BI are shown in Figures 5.2c and 5.2d, displaying overall faster decays. This is expected because the higher excess charge carrier concentrations under BI enhance second order recombination. Most interestingly, the dynamics in the MAPbI₃/C60 bilayer is almost identical to that in the MAPbI₃ single layer as is evident from Figure 5.2c, suggesting reduced charge extraction. Also, for the MAPbI₃/Spiro-OMeTAD bilayer faster decays are observed on BI and the decay does not show any long-lived tail. Nonetheless, in comparison to the single MAPbI₃ layer under BI, the lifetimes for the bilayer are still substantially longer (see Figure 5.2d). This might imply that part of the excess carriers is still extracted by the Spiro-OMeTAD, although less extensively than without BI. As shown in Figure 5.C.2, similar trends can be observed upon FS excitation of the bilayers. The independence of the excitation side implies that neither the initial excitation profile nor the period involved with diffusion of charges through the MAPbI₃ dominates the decay kinetics on the used time scales.

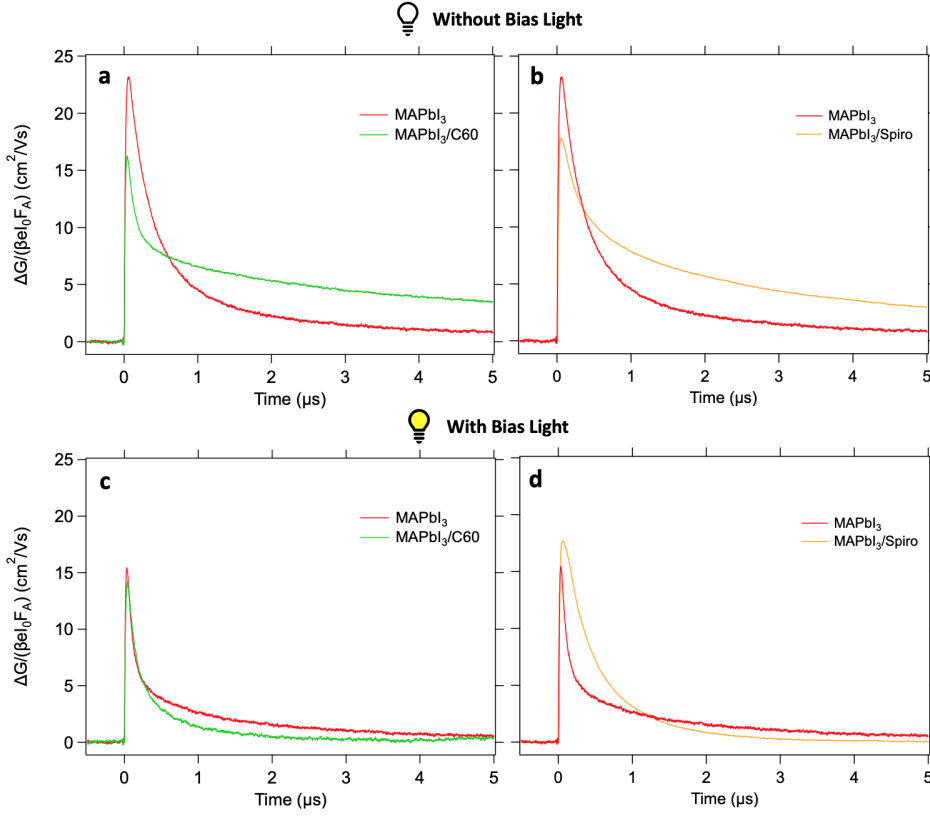


Figure 5.2: TRMC results upon excitation at 650 nm yielding an initial excitation density of 10^{15} charges/cm³/pulse for MAPbI₃ (red), MAPbI₃/C60 (green), and MAPbI₃/Spiro-OMeTAD (orange) in absence (a,b), and presence (c,d) of a 0.3 sun bias illumination.

In order to deduce the charge carrier extraction rates with and without BI, we adapted the kinetic model presented by Hutter et al.²⁵ The model accounts for all the processes provided in Figure 5.1a, and it allows us to determine the time-dependent charge carriers concentrations by solving four coupled differential equations (equations 5.1-5.4 for perovskite/ETL heterojunctions, and equations 5.C.2-5.C.5 in Appendix 5.C for a perovskite/HTL bilayer).

$$\frac{dn_e}{dt} = G_P - k_2 n_e (n_h + p_0) - k_T n_e (N_T - n_T) - k_{ext} n_e \quad (5.1)$$

$$\frac{dn_h}{dt} = G_P - k_2 n_e (n_h + p_0) - k_D n_t (n_h + p_0) - k_{rec} n_h \quad (5.2)$$

$$\frac{dn_T}{dt} = k_T n_e (N_T - n_T) - k_D n_T (n_h + p_0) \quad (5.3)$$

$$\frac{dn_{ETL}}{dt} = k_{ext} n_e - k_{rec} n_h \quad (5.4)$$

These equations include generation and recombination terms for electrons, n_e , and holes, n_h . G_P is the pulsed generation term, k_2 is the second order rate constant, and k_T and k_D are the trapping and de-trapping rate constants, respectively. It is important to notice that the second order recombination revealed by TRMC measurements accounts for both radiative and non-radiative contributions, as discussed in a previous study.²⁶ These parameters, together with the total number of trap states, N_T , and background carrier concentration, p_0 , are characteristic of spin-coated MAPbI₃. Due to the p-type character of MAPbI₃ n_0 is negligible and this term is not included in the coupled differential equations. Charge carrier extraction is characterized by the extraction and back recombination rate constants, k_{ext} and k_{rec} , respectively.

Typically, TRMC results are modelled taking into account the temporal laser pulse profile and its intensity (Figure 5.3a), resulting in the G_P term used in equations 5.1 and 5.2. The modelled photoconductance signals, fits to the TRMC traces, result from the sum of the time-dependent electron and hole contributions times their individual mobilities at specific intensities. In Figure 5.3b, the modelled electron (orange), hole (red), and trapped electron (green) concentrations are shown for the specific case of a 9.8×10^{13} excitations/cm³/pulse of the bare MAPbI₃ layer. In the next step we use the kinetic parameters obtained from the TRMC analysis to model the concentration of electrons and holes in the perovskite material under BI.²⁴ This is achieved by replacing the temporal profile of the laser pulse with a continuous illumination profile, G_{Bias} as shown in Figure 5.3c (see Appendix 5.B for calculation of the calculation of G_{Bias}). The results for the MAPbI₃ single layer, presented in Figure 5.3d, show that an equilibrium is reached in the perovskite film within 6 μ s, after which electron and hole concentrations remain constant. In order to model the laser pulse induced TRMC traces under BI, both the continuous bias illumination and laser pulse are combined in the generation term, G_{Com} , as shown in Figure 5.3e. The calculated concentration profiles from the model are shown in the inset of Figure 5.3f. Since, as discussed in Chapter 2, the TRMC set-up records only the AC part of the photo-conductance, the modelled traces are vertically shifted providing only the AC contributions as exemplified in Figure 5.3f. These calculated traces show the characteristic decays of a pulsed laser experiment, but take into account the charge carrier concentrations induced by the BI.

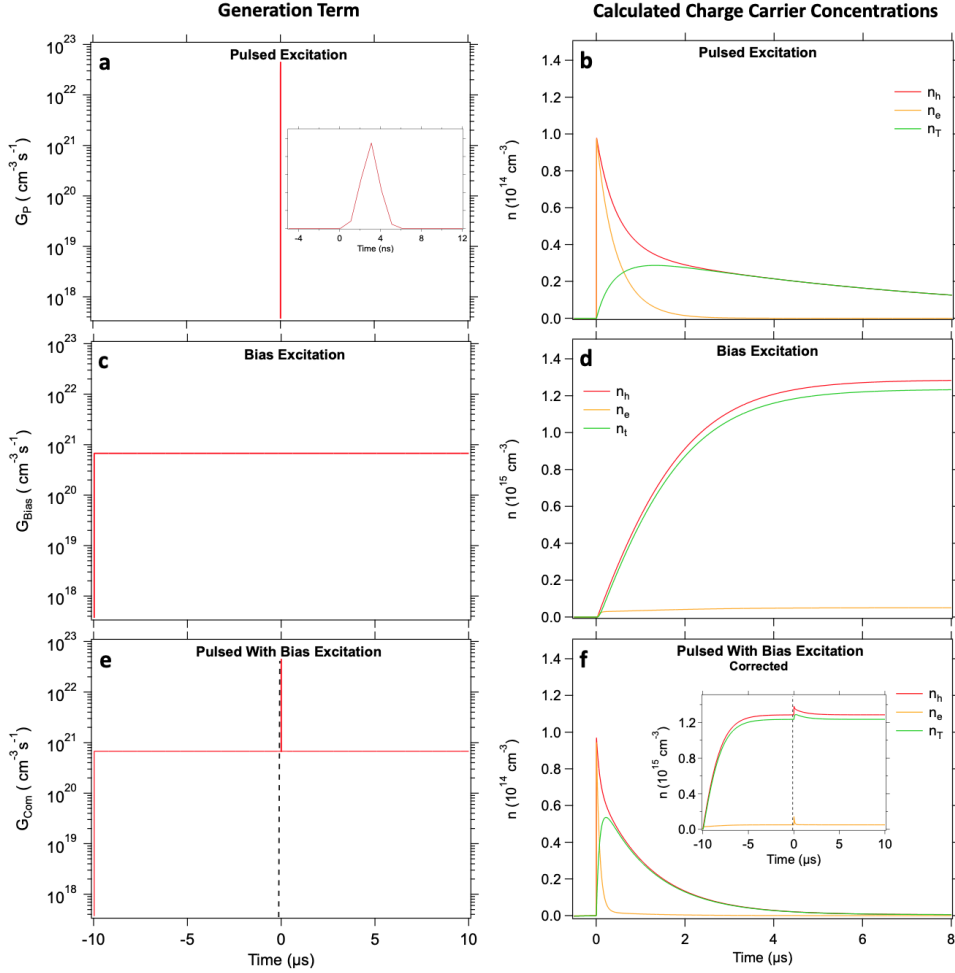


Figure 5.3: Simulation of the charge carrier concentrations using different illumination sources for a bare MAPbI₃ layer. When only pulsed excitation is used, the generation term, G_P , represents the temporal generation profile of the laser pulse and its intensity (here 9.8×10^{13} charges/cm³ per pulse) shown in (a), which results in the electron (orange), hole (red), and trapped carrier (green) concentrations shown in (b). The steady states carrier concentrations can be modelled with a continuous generation profile, as represented in (c), leading to the modelled concentrations shown in (d). For the analysis of the TRMC traces in presence of bias illumination, the two generation terms are combined to G_{Com} as shown in (e). After subtraction of the DC contribution, we can extract the relevant concentrations, as presented in (f). The magnitude of G_{Bias} for the bias illumination is derived from the LED power as described in Appendix 5.B.

5.4. MODELLING OF THE TRMC TRACES WITH AND WITHOUT BIAS ILLUMINATION

The above model and fitting procedure were applied to the three systems under investigation, i.e. bare MAPbI₃, MAPbI₃/C60, and MAPbI₃/Spiro-OMeTAD for many laser intensities. The protocol to obtain values for the various parameters by fitting the TRMC traces is described in Appendix 5.C. The TRMC results (dashed lines) and corresponding fits (solid lines) are shown in Figure 5.4, while the kinetic parameters are reported in Table 5.1. The iterative and global analysis of the three systems in parallel allows a detailed and accurate quantification of the opto-electronic properties of MAPbI₃. The fact that the excitation profile and corresponding charge diffusion within the MAPbI₃ have no effect on the TRMC signal, justifies the use of homogeneous differential equations on a clearly non-homogeneous system. Electron and hole mobilities in MAPbI₃ were found to be 30 and 25 cm²/(Vs), respectively, in agreement with previously reported values.²⁷ Furthermore, in absence of BI, the results revealed the presence of 10¹⁴ cm⁻³ deep trap states, N_T , in bare MAPbI₃, while the dark carrier concentration, p_0 , was found to be 6.5 x10¹⁴ cm⁻³ (5.4a and Table 5.1). For laser intensities yielding an excess charge density < N_T , the traces overlap, while for higher intensities 2nd order recombination becomes the dominant factor in the decay kinetics.

Interestingly, we observed a strong reduction of p_0 to a value of 6.0x10¹³ cm⁻³ in the MAPbI₃/Spiro-OMeTAD bilayer (Figure 5.4e), while for MAPbI₃/C60 no change in p_0 was observed. This can be explained by assuming that the Fermi level of the MAPbI₃ is below that of Spiro-OMeTAD. Note that the Spiro-OMeTAD in this study was not intentionally doped nor exposed to oxygen. Equilibration of the Fermi levels on contacting MAPbI₃ and Spiro-OMeTAD leads to transfer of positive carriers to the latter. This implies that our bare MAPbI₃ layer deposited on quartz is to some extent p-doped, which is in line with recent studies.^{28,29} To corroborate this explanation, we performed steady state microwave conductance (SSMC) measurements on bare and bilayers in the dark. As discussed in Chapter 2, an SSMC experiment provides information on the background conductivity of a semiconductor layer.³⁰ On comparison of the MAPbI₃ to the MAPbI₃/Spiro-OMeTAD bilayer we observed an appreciable reduction of the background conductivity in the bilayer (see Appendix 5.C Figure 5.C.1). In analogy to the reasoning above on equilibration of the Fermi levels, holes are transferred from the MAPbI₃ to the Spiro-OMeTAD layer. Due to the decreased hole mobility in the Spiro-OMeTAD, an overall reduction in conductivity is expected in agreement with our SSMC experiments. This result supports the conclusion regarding the type of the doping in MAPbI₃. Apart from this change in p_0 the MAPbI₃/Spiro-OMeTAD bilayer, we can use for fitting the bilayers, the kinetic parameters found for the MAPbI₃ layer completed by introduction of a first order extraction and a recombination process (see Table 5.1). Interestingly the presented kinetic model captures the reversed intensity dependencies for both bilayers very well (compare Figures 5.4c with 5.4e). For the MAPbI₃/Spiro-OMeTAD a higher intensity leads to longer lifetimes, while for the MAPbI₃/C60 higher intensities lead to faster decays. As previously discussed,^{23,25} the different behaviors are related to the nature of the deep trap states in MAPbI₃ which have been proven to be electron traps.

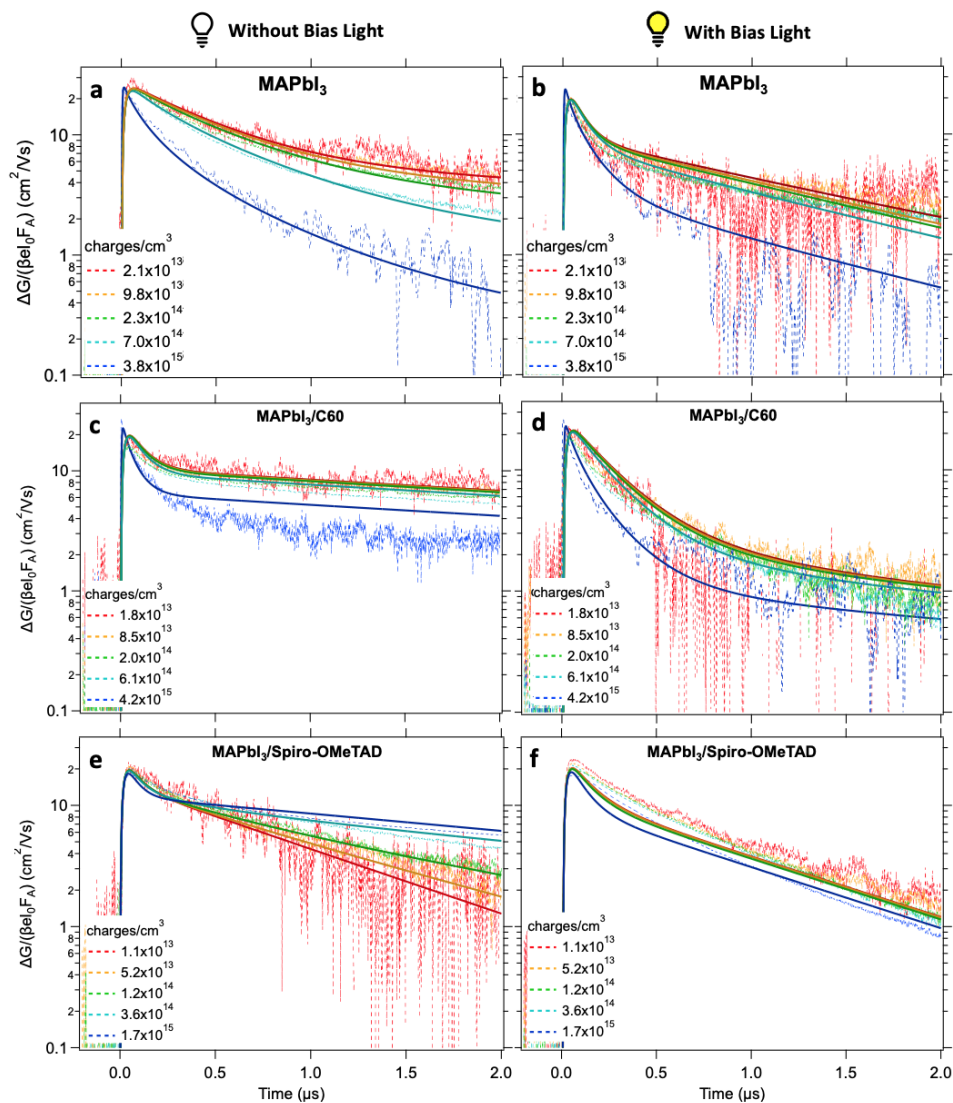


Figure 5.4: TRMC traces (dashed lines) and fits (solid lines) upon 650 nm pulsed excitation without (left) and with (right) bias illumination for MAPbI₃ single layer (a,b), MAPbI₃/C60 (c,d), and MAPbI₃/Spiro-OMeTAD (e,f).

Table 5.1: Rate constants and trap densities used for the fits to the TRMC signals of bare MAPbI₃, MAPbI₃/C60 and MAPbI₃/Spiro-OMeTAD without and with bias illumination.

	Without Bias			With Bias		
	MAPbI ₃	MAPbI ₃ / C60	MAPbI ₃ / Spiro	MAPbI ₃	MAPbI ₃ / C60	MAPbI ₃ / Spiro
k_2 (10^{-9} cm ³ /s)	2.0	2.0	1.8	2.0	2.0	1.8
k_T (10^{-9} cm ³ /s)	9.8	9.8	9.8	9.8	9.8	9.8
k_D (10^{-9} cm ³ /s)	0.20	0.20	0.20	0.20	0.20	0.20
N_T (10^{14} cm ⁻³)	1.0	1.0	1.0	22	3.0	22
p_0 (10^{14} cm ⁻³)	6.5	6.5	0.6	6.5	6.5	0.6
k_{ext} (10^6 s ⁻¹)	-	9.0	15	-	1.0	8.0
k_{rec} (10^6 s ⁻¹)	-	0.20	0.23	-	0.20	1.0

Now we turn to the experiments with BI and start with the bare MAPbI₃ shown in Figure 5.4c. The fast recombination is followed by a small but long-lived tail. Fits on the TRMC signals with BI (Figure 5.4b) reveal that, most importantly, the same parameters can be used except for the trap state concentration, N_T , which increases by more than 1 order of magnitude, reaching 22×10^{14} cm⁻³. This increment can be related to ionic motion in the MAPbI₃ film, induced by the BI. Interestingly after storage of the MAPbI₃ film in the dark for 3h, N_T reverts back to its original value, which demonstrates the reversibility of this degradation process (see Figure 5.C.4a in Appendix 5.C). Taking this light instability into account, the model can accurately fit the TRMC traces without any further modification of the fitting parameters given in Table 5.1, as can be seen from Figure 5.4b.

As mentioned, BI of the MAPbI₃/C60 bilayer leads to decay kinetics comparable to those of MAPbI₃ under BI. However, the MAPbI₃/C60 bilayer does not show any sign of a tail (see Figure 5.3c) implying no major increase in N_T under BI, i.e. N_T does not substantially vary in strong contrast with the value found in bare MAPbI₃. In fact, from the fitting the TRMC traces of the MAPbI₃/C60 bilayer with BI, we observe only a minor increment of the trap state concentration, reaching 3×10^{14} cm⁻³. Hence, we can conclude that the C60 layer hinders the formation of additional deep trap states under BI, presumably at the surface of the MAPbI₃. This is in line with previous research arguing that C60 is able to passivate the surface of perovskite materials, resulting in efficient charge carrier extraction and high device efficiencies.^{8–10,23} From Table 5.1 we notice that the only parameter that changes under BI is k_{ext} . We suggest that k_{ext} is reduced under BI because of pilling up of electrons in the C60. This leads to formation of an electric field over the interface impeding the extraction process of electrons into C60.

For the MAPbI₃/Spiro-OMeTAD bilayer measured under BI a combination of both effects are observed. In contrast to MAPbI₃/C60 bilayers, the presence of Spiro-OMeTAD does not prevent the degradation process leading to an increase of N_T . Furthermore, the extraction process is reduced by the presence of the bias illumination, in combination with a fourfold increase of k_{rec} (see Table 5.1). As previously mentioned, the instability of MAPbI₃ under BI can be related to ionic motion in the perovskite layer. During BI of the MAPbI₃/Spiro-OMeTAD bilayer, holes are collected and accumulate in the HTL,

attracting negatively charged iodine ions toward the interface. Ion accumulation at the interface has been indicated as one of the reasons of hysteresis in the J-V curves,^{5,7,9,21} and could explain the changes in extraction (reduced) and interfacial recombination (increased) rate constants. In addition, TRMC measurements performed after the BI was turned off, showed much faster decay kinetics, which only partially recovered after 24h, as shown in Figure Figure 5.C.4c. It has been reported that some of the iodine ions can chemically interact with the Spiro-OMeTAD molecule, leading to irreversible degradation of the HTL,¹⁸ in line with the only partial recovery that we observe. The results presented here provide a strong link between the surface/interface properties and the instability of the perovskite under steady state illumination.

5.5. AM1.5 SIMULATION

Although the model presented in Figure 5.1 might not include all processes in full detail, the combined set of processes can be used to describe the main trends of the charge carrier dynamics in MAPbI₃ and bilayers under BI. Knowing the rate constants enables us to calculate a number of interesting aspects including the various loss factors and the quasi Fermi level splitting (*QFLS*) under simulated sun light. We calculated the steady state carrier concentrations described by the coupled differential equations. The generation term, G_{Bias} , comprises the intensity corresponding to illumination of the MAPbI₃ layer with 0.3 suns. The evolution of the various concentrations in time until steady state is achieved, are shown in Figures 5.C.3. Furthermore, the calculated concentrations are compared to the results of SSMC experiments for MAPbI₃ and MAPbI₃/C60 samples (see Figure 5.5a for MAPbI₃ data). From the fits (solid lines) to the data points (markers) the concentration of charge carriers as function of the light intensity can be derived (see Figure 5.5b).^{24,30} The SSMC results on MAPbI₃/Spiro-OMeTAD have not been included due to the light instability of the bilayer at higher illumination densities. In Figure 5.5b, these SSMC results are compared with the calculated concentrations of mobile charges at 0.3 suns showing perfect agreement. However, the calculated values at 1 sun are a factor of 2-3 too high, exceeding $2.0 \times 10^{15} \text{ cm}^{-3}$ in MAPbI₃ and $3.0 \times 10^{15} \text{ cm}^{-3}$ in the bilayer. For MAPbI₃, this can be attributed to the intensity-dependent light degradation, which makes the N_T value extracted at 0.3 suns inaccurate for simulations at higher intensities. In addition, for MAPbI₃/C60 it is likely that at higher intensities the extraction and recombination rates become even closer.

In view of the fact that our model can accurately describe the concentrations at 0.3 suns, the losses for each decay channel can now be quantified and are presented in Table 5.2. For MAPbI₃ the decay via trap mediated recombination is rather large, mainly due to the substantial rise in N_T related to the light instability of MAPbI₃ and absence of a surface passivating agent. For the MAPbI₃/C60 bilayer we notice that the charge extraction is limited (<25%) and the carriers mainly decay in the MAPbI₃ bulk via second order and trap-assisted recombination. On the contrary, hole extraction and back recombination dominates the kinetics in the MAPbI₃/Spiro-OMeTAD bilayer. The majority of the light induced holes (75%) decays by getting first extracted by the Spiro-OMeTAD followed by recombination with excess electrons. Despite the higher concentration of trap states under bias illumination, trap assisted recombination is relatively small due to the fast saturation of almost all N_T , followed by slow recombination.

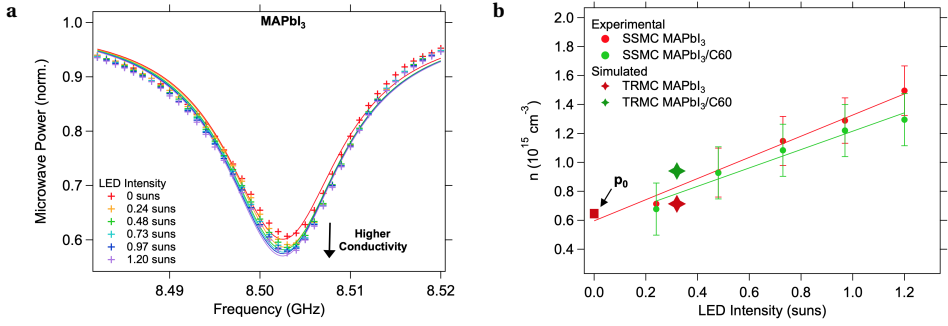


Figure 5.5: (a) Evolution of the steady-state microwave conductance dip under various LED light intensity. The experimental data points are indicated by the markers. The solid lines represent the fits from which the conductivity, and corresponding carrier concentrations, have been derived. A decrease of the normalized microwave power is related to an increased conductivity in the sample, i.e. higher charge carrier concentration under illumination. (b) The charge carrier concentrations in MAPbI₃ (red) and MAPbI₃/C60 (green) experimentally determined by SSMC measurements (circles) are compared to the simulated concentrations at 0.3 suns (diamonds), showing excellent agreement. The background concentration of charge carriers, p_0 , determined from the fits is also shown as red square at the LED intensity of 0 suns.

Table 5.2: Calculated loss fractions using the kinetic parameters from the TRMC fits at 0.3 suns. The values are obtained using the "with bias" fitting parameters of Table 5.1. The values in brackets are obtained using the "without bias" parameters and are provided for comparison.

	2 nd Order (%)	Trap assisted (%)	Charge extraction (%)	Populated N_T (%)	$QFLS$ (eV)
MAPbI ₃	29 (97)	71 (3)	-	56 (93)	1.12 (1.16)
MAPbI ₃ /C60	54 (36)	11 (3.5)	23 (60.5)	84 (45)	1.15 (1.13)
MAPbI ₃ /Spiro	16 (40)	8 (0.30)	75 (59.7)	99 (100)	1.11 (1.13)

From the concentration curves calculated and shown in Figures 5.C.3, also the quasi Fermi level splitting, $QFLS$, corresponding to the upper limit of qV_{OC} of a device, can be calculated using:

$$QFLS = \frac{kT}{q} \ln \left(\frac{(n_0 + \Delta n)(p_0 + \Delta p)}{n_i^2} \right) \quad (5.5)$$

In equation 5.5, k is the Boltzmann constant, T the temperature, q the elementary charge; n_0 and p_0 represent the thermal equilibrium concentrations of electrons and holes, respectively, while Δn and Δp are the photoexcited excess charge carrier concentrations. The intrinsic carrier concentration, n_i , has been evaluated to be ca $1 \times 10^5 \text{ cm}^{-3}$. The calculated $QFLS$ values in bare MAPbI₃, in MAPbI₃/C60 and in MAPbI₃/Spiro-OMeTAD bilayers under 0.3 suns are reported in Table 5.2. A larger splitting is observed in MAPbI₃/C60 than for the bare MAPbI₃, while a clear reduction is obtained for MAPbI₃/Spiro-OMeTAD. This can be expected on the basis of the C60 passivation effect and ionic

motion towards the Spiro-OMeTAD interface mentioned in the above discussion. For the latter, reducing the value of k_{rec} is a logical step in order to improve the V_{OC} . Therefore, designing TLs giving rise to an active heterojunction capable of accepting one type and repelling the counter charge is essential. Alternatively reduction of k_{rec} could be achieved, e.g. by introducing an interlayer between the perovskite and TL.^{31–34} Furthermore, careful tuning of the band offsets might be a way to influence the rate constants involved.

Lastly, our study reveals that the determination of the kinetic parameters under bias illumination is of utmost importance if we want to understand the loss mechanisms under device operation. Since some of the kinetic parameters are varying with light intensity in MAPbI₃ and MAPbI₃/TL, these parameters cannot be used for the simulation of device performance directly. As given in brackets in Table 5.2, the loss fractions and $QFLS$ values are substantially different in case the "without bias" parameters of Table 5.1 are used for the steady-state simulation at 0.3 suns. In MAPbI₃, the strong underestimation of the trap density would lead to an underestimation of the trap-assisted recombination contribution, ultimately leading to a higher V_{OC} . For the bilayers, the interfacial processes are the most affected by BI. Despite the passivation effect of C60, the electron extraction in MAPbI₃/C60 is substantially reduced under BI. For the MAPbI₃/Spiro-OMeTAD the ionic migration towards the interface with Spiro-OMeTAD enhances the interfacial recombination under BI. Moreover, as concluded from the SSMC results, these effects are likely to be even more pronounced at higher illumination intensities.

5.6. CONCLUSIONS

To summarize, in this paper we performed time-resolved microwave photoconductance measurements in presence and absence of bias illumination in single and bilayers. A kinetic model was used to describe the kinetics including the charge generation, charge recombination and extraction. Owing to the iterative analysis of the three systems using a broad range of laser intensities, we were able to accurately determine the kinetic parameters for bare MAPbI₃, MAPbI₃/C60 and MAPbI₃/Spiro-OMeTAD in presence and absence of BI. For MAPbI₃ we found that the same parameters can be used under BI except for the trap state concentration, N_T , which increases by more than one order of magnitude, reaching $22 \times 10^{14} \text{ cm}^{-3}$. This increment is related to ionic motion in the MAPbI₃ film. Interestingly, after storing the MAPbI₃ film in the dark for three hours, N_T reverts back to its original value, which demonstrates the reversibility of this degradation process. For the MAPbI₃/C60 bilayer under BI, we observe only a minor increment of N_T , which shows that C60 hinders the formation of additional deep trap states. Under BI only the extraction rate k_{ext} is reduced due to pilling up of electrons in the C60, which leads to formation of an electric field over the interface impeding the extraction process of electrons into C60.

In contrast to MAPbI₃/C60 bilayers, the presence of Spiro-OMeTAD does not prevent the degradation process leading to an increase of N_T . Furthermore, under BI the extraction process is reduced, in combination with a fourfold increase of k_{rec} , which are related to ion accumulation at the interface. Moreover, we show that to calculate carrier concentrations for deducing device parameters, like the $QFLS$, it is important to use the kinetic parameters found under BI. This study adds to the understanding of both the heterojunctions interfacial properties, as well as the origin of the light instability in MAPbI₃, crucial factors for the performance of perovskite-based devices.

SAMPLE PREPARATION

215 nm thick MAPbI₃ thin films have been prepared by spin-coating a 37 wt% solution of MAI (synthesized following standard procedure)³⁵ and $Pb(Ac)_2 \cdot 3H_2O$ (Sigma-Aldrich) powders (3:1 ratio) in DME. The solution was spin-coated on plasma cleaned quartz plates at 2000 rpm for 45 s in a nitrogen filled glovebox and left to dry for 15 minutes at room temperature. The films have been annealed at 100°C for 5 minutes.

Selective transport materials have been deposited on top of the MAPbI₃ films via the following procedures: 30 nm C60 layer has been thermally evaporated, while a 75 mg/mL solution of Spiro-OMeTAD in chlorobenzene has been spin-coated at 1500 rpm for 45 s. The samples been then dried for 1 hour at 60°C to remove the remaining solvent.

BIBLIOGRAPHY

- (1) Jeong, J. et al. *Nature* **2021**, 592, 381–385.
- (2) Zhao, J.; Caselli, V. M.; Bus, M.; Boshuizen, B.; Savenije, T. J. *ACS Applied Materials and Interfaces* **2021**, 13, 16309–16316.
- (3) Zhang, W.; Pathak, S.; Sakai, N.; Stergiopoulos, T.; Nayak, P. K.; Noel, N. K.; Haghighi-irad, A. A.; Burlakov, V. M.; Dequillettes, D. W.; Sadhanala, A.; Li, W.; Wang, L.; Ginger, D. S.; Friend, R. H.; Snaith, H. J. *Nature Communications* **2015**, 6, 1–9.
- (4) Hu, Y. et al. *Advanced Energy Materials* **2018**, 1703057, 1–11.
- (5) Chen, J.; Park, N. G. *ACS Energy Letters* **2020**, 5, 2742–2786.
- (6) Wolff, C. M.; Caprioglio, P.; Stolterfoht, M.; Neher, D. **2019**, 1902762, DOI: [10 . 1002/adma.201902762](https://doi.org/10.1002/adma.201902762).
- (7) Kim, T.; Lim, J.; Song, S. *Energies* **2020**, 13, 1–16.
- (8) Wolff, C. M.; Zu, F.; Paulke, A.; Toro, L. P.; Koch, N.; Neher, D. *Advanced Materials* **2017**, 29, 1700159.
- (9) Shao, Y.; Xiao, Z.; Bi, C.; Yuan, Y.; Huang, J. *Nature Communications* **2014**, 5, 1–7.
- (10) Chen, B.; Rudd, P. N.; Yang, S.; Yuan, Y.; Huang, J. *Chemical Society Reviews* **2019**, 48, 3842–3867.
- (11) Arumugam, G. M.; Karunakaran, S. K.; Liu, C.; Zhang, C.; Guo, F.; Wu, S.; Mai, Y. *Nano Select* **2021**, 2, 1081–1116.
- (12) Sarritzu, V.; Sestu, N.; Marongiu, D.; Chang, X.; Masi, S.; Rizzo, A.; Colella, S.; Quochi, F.; Saba, M.; Mura, A.; Bongiovanni, G. *Scientific Reports* **2017**, 7, 1–10.
- (13) Caprioglio, P.; Stolterfoht, M.; Wolff, C. M.; Unold, T.; Rech, B.; Albrecht, S.; Neher, D. *Advanced Energy Materials* **2019**, 9.
- (14) Pydzńska, K.; Karolczak, J.; Kosta, I.; Tena-Zaera, R.; Todinova, A.; Idígoras, J.; Anta, J. A.; Ziólek, M. *ChemSusChem* **2016**, 9, 1647–1659.
- (15) Ponseca, C. S.; Hutter, E. M.; Piatkowski, P.; Cohen, B.; Pascher, T.; Douhal, A.; Yartsev, A.; Sundström, V.; Savenije, T. J. *Journal of the American Chemical Society* **2015**, 137, 16043–16048.
- (16) Makuta, S.; Liu, M.; Endo, M.; Nishimura, H.; Wakamiya, A.; Tachibana, Y. *Chem. Commun.* **2015**, 52, 673–676.
- (17) *Phys. Chem. Chem. Phys.* **2015**, 17, 14674–14684.
- (18) Brauer, J. C.; Lee, Y. H.; Nazeeruddin, M. K.; Banerji, N. *J. Mater. Chem. C* **2016**, 4, 5922–5931.

- (19) Levine, I.; Al-Ashouri, A.; Musiienko, A.; Hempel, H.; Magomedov, A.; Drevilka-uskaite, A.; Getautis, V.; Menzel, D.; Hinrichs, K.; Unold, T.; Albrecht, S.; Dittrich, T. *Joule* **2021**, 1–19.
- (20) Levine, I.; Gupta, S.; Bera, A.; Ceratti, D.; Hodes, G.; Cahen, D.; Guo, D.; Savenije, T. J.; Ávila, J.; Bolink, H. J.; Millo, O.; Azulay, D.; Balberg, I. *Journal of Applied Physics* **2018**, 124, DOI: [10.1063/1.5037637](https://doi.org/10.1063/1.5037637).
- (21) Futscher, M. H.; Lee, J. M.; McGovern, L.; Muscarella, L. A.; Wang, T.; Haider, M. I.; Fakhruddin, A.; Schmidt-Mende, L.; Ehrler, B. *Materials Horizons* **2019**, DOI: [10.1039/c9mh00445a](https://doi.org/10.1039/c9mh00445a).
- (22) Carrillo, J.; Guerrero, A.; Rahimnejad, S.; Almora, O.; Zarazua, I.; Mas-Marza, E.; Bisquert, J.; Garcia-Belmonte, G. *Advanced Energy Materials* **2016**, 6, 1–7.
- (23) Caselli, V. M.; Wei, Z.; Ackermans, M. M.; Hutter, E. M.; Ehrler, B.; Savenije, T. J. *ACS Energy Letters* **2020**, 5, 3821–3827.
- (24) Guo, D.; Caselli, V. M.; Hutter, E. M.; Savenije, T. J. *ACS Energy Letters* **2019**, 4, 855–860.
- (25) Hutter, E. M.; Hofman, J. J.; Petrus, M. L.; Moes, M.; Abellón, R. D.; Docampo, P.; Savenije, T. J. *Advanced Energy Materials* **2017**, 7, 1–8.
- (26) Brenes, R.; Guo, D.; Oshero, A.; Noel, N. K.; Eames, C.; Hutter, E. M.; Pathak, S. K.; Niroui, F.; Friend, R. H.; Islam, M. S.; Snaith, H. J.; Bulović, V.; Savenije, T. J.; Stranks, S. D. *Joule* **2017**, 1, 155–167.
- (27) Savenije, T. J.; Guo, D.; Caselli, V. M.; Hutter, E. M. *Advanced Energy Materials* **2020**, 10, 1–12.
- (28) Olthof, S.; Meerholz, K. *Scientific Reports* **2017**, 7, 1–10.
- (29) Caputo, M. et al. *Scientific Reports* **2019**, 9, 1–11.
- (30) Caselli, V. M.; Fischer, M.; Meggiolaro, D.; Mosconi, E.; Angelis, F. D.; Stranks, S. D.; Baumann, A.; Dyakonov, V.; Hutter, E. M.; Savenije, T. J. *Journal of Physical Chemistry Letters* **2019**, 10, 5128–5134.
- (31) Bouduban, M. E.; Queloz, V. I.; Caselli, V. M.; Cho, K. T.; Kirmani, A. R.; Paek, S.; Roldan-Carmona, C.; Richter, L. J.; Moser, J. E.; Savenije, T. J.; Nazeeruddin, M. K.; Grancini, G. *Journal of Physical Chemistry Letters* **2019**, 10, 5713–5720.
- (32) Zhao, R.; Zhang, K.; Zhu, J.; Xiao, S.; Xiong, W.; Wang, J.; Liu, T.; Xing, G.; Wang, K.; Yang, S.; Wang, X. *Nanoscale Advances* **2021**, 3, 2305–2315.
- (33) Li, H.; Tao, L.; Huang, F.; Sun, Q.; Zhao, X.; Han, J.; Shen Yan Wang, M. *ACS Applied Materials and Interfaces* **2017**, 9, 38967–38976.
- (34) Koushik, D.; Verhees, W. J.; Kuang, Y.; Veenstra, S.; Zhang, D.; Verheijen, M. A.; Creatore, M.; Schropp, R. E. *Energy and Environmental Science* **2017**, 10, 91–100.
- (35) Kim, H. S.; Lee, C. R.; Im, J. H.; Lee, K. B.; Moehl, T.; Marchioro, A.; Moon, S. J.; Humphry-Baker, R.; Yum, J. H.; Moser, J. E.; Grätzel, M.; Park, N. G. *Scientific Reports* **2012**, 2, 1–7.

APPENDICES

5.A. STRUCTURAL CHARACTERISATION

The XRD spectrum of the MAPbI₃ thin film is shown in Figure 5.A.1. XRD measurements have been performed with a Brüker D8 diffractometer (Co K α -1, 1.78Å).

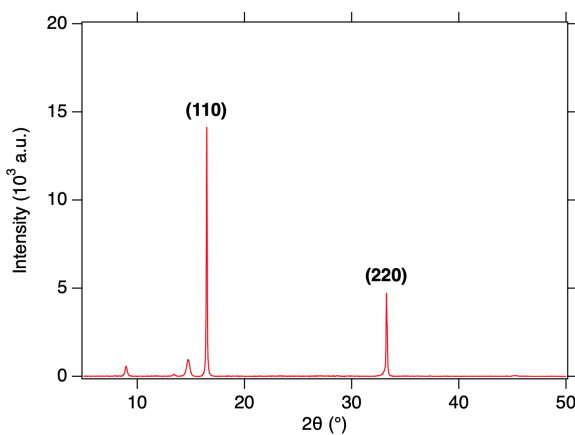


Figure 5.A.1: MAPbI₃ thin film XRD spectrum.

5.B. BIAS ILLUMINATION

The LED intensity has been estimated from the AM1.5 spectrum accounting for the lamp emission range and absorption of the films analysed, as described in Chapter 2. The light intensity at the sample position has been measured with a Silicon photodiode (Coherent, OP-2/LM-2 VIS), yielding a value of 13.5 mWatt cm⁻². This intensity matches to the total number of integrated photons of the white light LED. Next, we integrated the number of photons over the wavelength emission range of the LED, however now corrected for the fraction of absorbed photons yielding values for G_{Bias} of 6.74, 6.79 and 6.46×10^{20} cm⁻³s⁻¹ in the pristine MAPbI₃, MAPbI₃/C60 and MAPbI₃/Spiro-OMeTAD, respectively. The absorbance spectra are shown in Figure 5.B.1b. To relate the observed values of G_{Bias} to AM1.5 we corrected the LED spectrum for the solar emission spectrum and the absorbance spectrum of the photoactive layer (shown in Figs 5.B.1c). After integration this corrected emission spectrum over the wavelength, the G_{Bias} profile corresponding to AM1.5 is found.

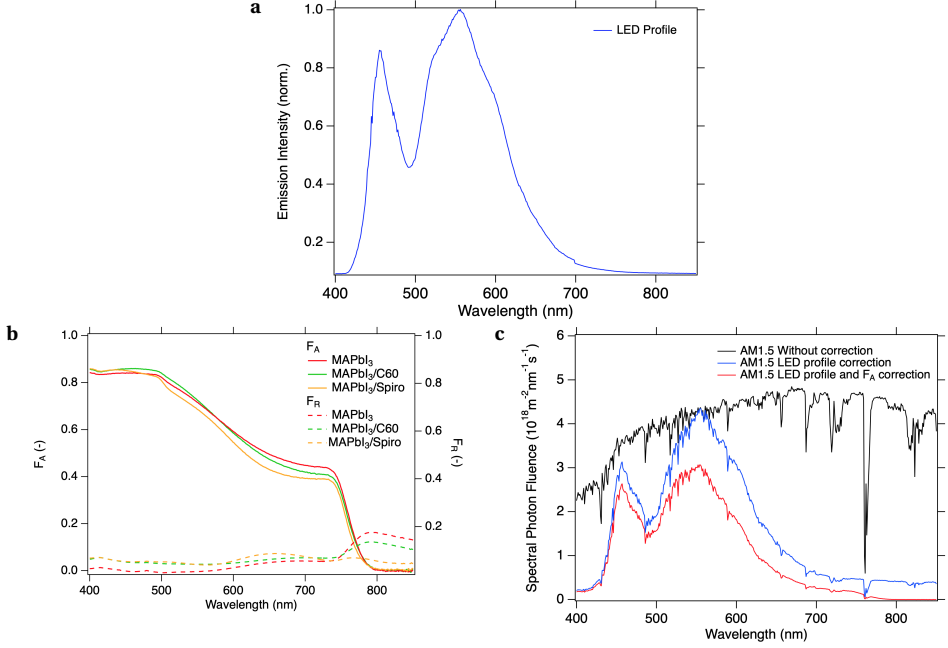


Figure 5.B.1: (a) LED emission profile; (b) fraction of absorbed (solid lines), F_A , and reflected (dashed lines), F_R , of pristine MAPbI₃ (red), MAPbI₃/C60 (green), and MAPbI₃/Spiro-OMeTAD (orange) films; (c) AM1.5 spectra not corrected (black), corrected for LED emission profile (blue), and F_A of the MAPbI₃ sample used in this study.

5.C. ADDITIONAL MICROWAVE CONDUCTANCE DATA

In the study presented in Chapter 5, we have performed SSMC measurements in the dark, see Figure 5.C.1, and in presence of bias illumination, as shown in Figure 5.4d in the main text. From Figure 5.C.1 it is possible to notice a higher microwave power detected at the resonance frequency for MAPbI₃/Spiro-OMeTAD compared to pristine MAPbI₃. As discussed in the main text, this is an indication of reduced background conductivity in the bilayer. On the other hand, from the fittings of the SSMC results under bias illumination we have estimated the conductivity of the MAPbI₃ layer, and estimated the number of charge carriers, n , in the material according to:

$$n = \frac{\sigma}{e \sum \mu} \quad (5.C.1)$$

where e is the elementary charge and $\sum \mu$ the sum of electron and hole mobilities. From this analysis it is not possible to directly discriminate the electron and hole contributions. Nonetheless, we can use the estimated values to validate the TRMC model, as described in the main text.

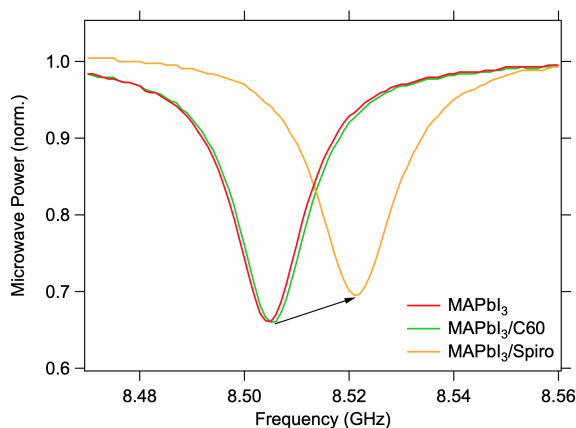


Figure 5.C.1: SSMC results in the dark for pristine MAPbI₃ (red), MAPbI₃/C60 (green), and MAPbI₃/Spiro-OMeTAD (orange).

5

The homogeneity of excitation throughout the sample has been tested by performing the same experiments upon FS illumination, i.e. from the perovskite and TM side. The results are shown in Figure 5.C.2. The lower magnitude of MAPbI₃/C60 sample in Figure 5.C.2b compared to the single layer can be explained by the increased fraction of absorbed bias light in the TM layer, which is now directly irradiated.

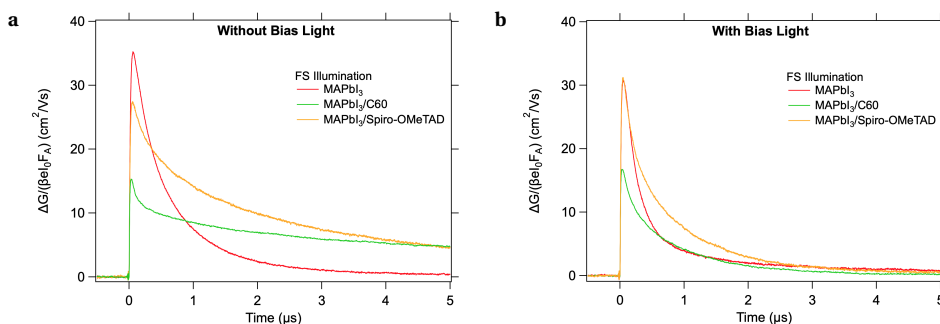


Figure 5.C.2: (MAPbI₃ (red), MAPbI₃/C60 (green) and MAPbI₃/Spiro-OMeTAD traces recorded at 650 nm FS illumination (ca. 7×10^9 photons/cm²) (a) without and (b) with bias illumination.

The time-dependent concentrations obtained from a steady state simulation at 0.3 suns are shown in Figure S6 for MAPbI₃ (a), MAPbI₃/C60 (b) and MAPbI₃/Spiro-OMeTAD (c).

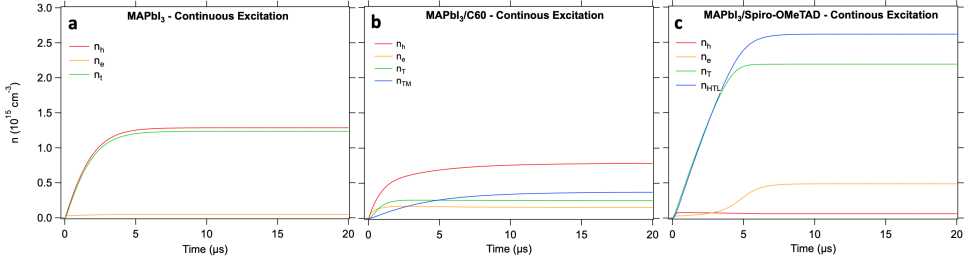


Figure 5.C.3: Simulated time-dependent concentrations under continuous (0.3 suns) illumination of free electrons and holes, n_e and n_h , trapped carriers, n_T and transferred electrons/holes into the selective transport materials, $n_{ETL/HTL}$ in (a) MAPbI₃, (b) MAPbI₃/C60, and (c) MAPbI₃/Spiro-OMeTAD.

Lastly, the bias illumination effects during and after illumination are shown Figure 5.C.4 for MAPbI₃ (a), MAPbI₃/C60 (b), and MAPbI₃/Spiro-OmeTAD (c).

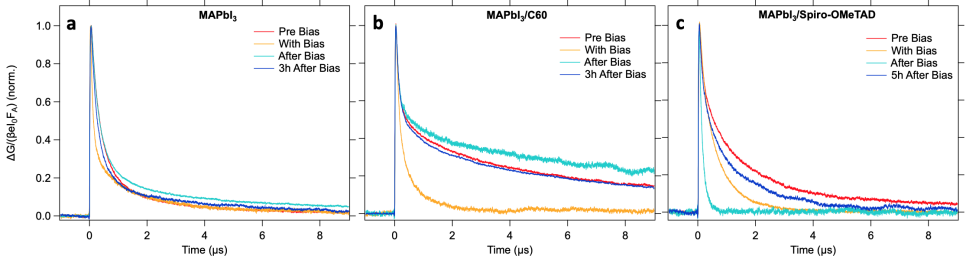


Figure 5.C.4: Normalised TRMC traces recorded at a laser intensity of ca. $3.5 \times 10^{14} \text{ cm}^{-3}$ per pulse, showing the effect of bias light on (a) MAPbI₃, (b) MAPbI₃/C60 and (c) MAPbI₃/Spiro-OMeTAD bilayer during and after illumination. No further changes have been observed in the next 24h.

MODELLING TRMC MEASUREMENTS

Similar to equations 5.1-5.4 in the main text, the differential equations used to fit the TRMC traces of the MAPbI₃/Spiro-OMeTAD heterojunction are:

$$\frac{dn_e}{dt} = G_P - k_2 n_e (n_h + p_0) - k_T n_e (N_T - n_T) - k_{rec} n_e \quad (5.C.2)$$

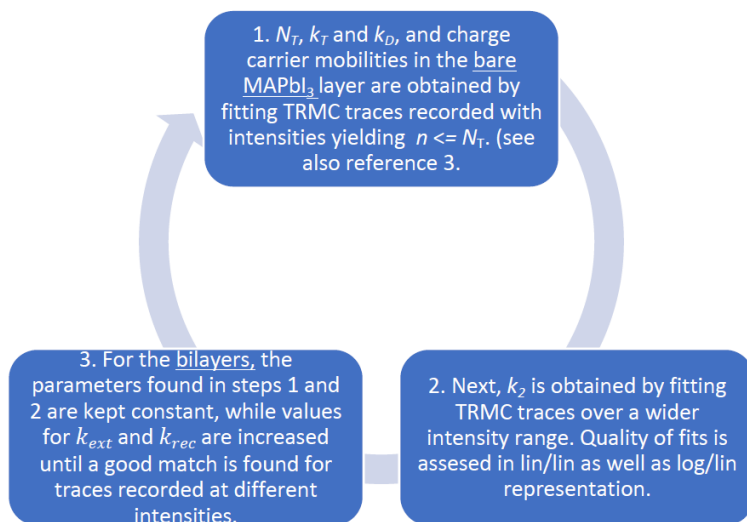
$$\frac{dn_h}{dt} = G_P - k_2 n_e (n_h + p_0) - k_D n_t (n_h + p_0) - k_{ext} n_h \quad (5.C.3)$$

$$\frac{dn_T}{dt} = k_T n_e (N_T - n_T) - k_D n_T (n_h + p_0) \quad (5.C.4)$$

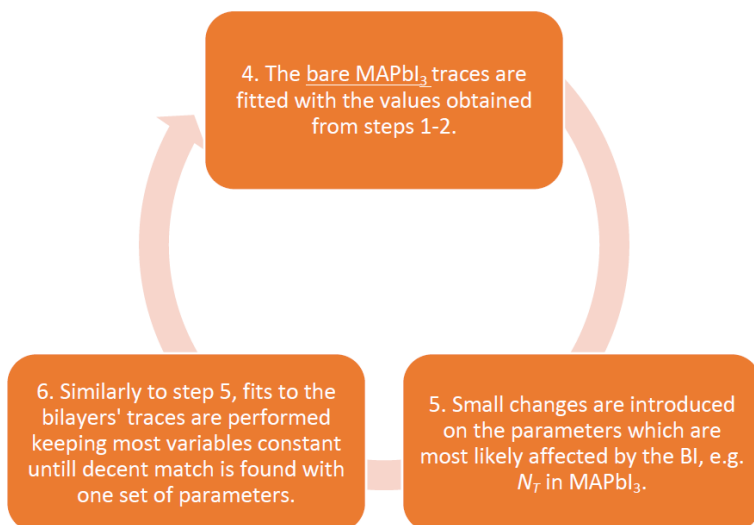
$$\frac{dn_{HTL}}{dt} = k_{ext} n_h - k_{rec} n_e \quad (5.C.5)$$

The global, iterative fitting procedure can be summarized as follows:

- In absence of bias illumination (only pulsed excitation, G_P):



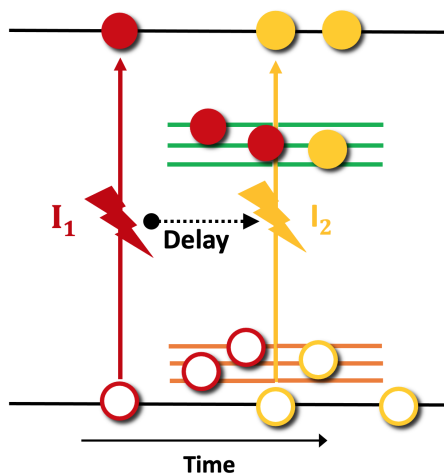
- In presence of bias illumination (G_{com}):



6

CS₂AGBIBR₆'S TRAPS IN THE SPOTLIGHT

In this chapter, the attention moves toward lead-free perovskites and their suitability as candidates for photovoltaic applications. To elucidate the loss mechanisms in devices, the charge dynamics in Cs₂AgBiBr₆ films has been investigated by double pulse excitation time-resolved microwave conductivity (DPE-TRMC). Modeling the DPE-TRMC results, complemented by photoluminescence and transient absorption, we reveal the presence of deep emissive electron traps, while shallow hole trapping is responsible for the long-living transient absorption signals.



This chapter is based on:

Valentina M. Caselli, Jos Thieme, Huygen J. Jöbsis, Sohan A. Phadke, Jiashang Zhao, Eline M. Hutter and Tom J. Savenije, Traps in the Spotlight: How Traps Affect the Charge Carriers Dynamics in Cs₂AgBiBr₆ Perovskite, Cell Reports Physical Science 2022, 3, 101055

6.1. TOWARDS LEAD-FREE PEROVSKITES

SINCE their discovery as versatile semiconductors for photovoltaic applications, perovskite materials, with general formula ABX_3 , have been intensively studied. Tuning of their opto-electronic properties make it possible to reach remarkable power conversion efficiencies, currently topping at 25.6%,¹ in roughly a decade of development. However, a rising concern regarding the use of lead in the photoactive layer has pushed research into lead-free alternative candidates. Attempts have been made to substitute the bivalent Pb^{2+} with alkaline metals^{2,3} and homovalent Sn^{2+} or Ge^{2+} . Unfortunately, devices made with these elements show lower performances compared to their Pb analogues, and fast degradation.⁴⁻⁷ Nonetheless, impressive efficiencies have been recently obtained with mixed Pb/Sn-based perovskites, despite the fast oxidation of the metal into Sn^{4+} .^{8,9} Thanks to the flexibility of the perovskite structure also double metal $\text{A}_2\text{B}'\text{B}''\text{X}_6$ perovskites can be synthesized. In these materials, the Pb^{2+} is replaced by a monovalent, B', and a trivalent, B'', metal, present in the structure in an alternate fashion. Among them, $\text{Cs}_2\text{AgBiBr}_6$ is one of the most studied candidate not only for photovoltaic applications, but also for X-ray detection and photocatalysis.¹⁰⁻¹⁵ This material can be synthesized via solution processes as well as by thermal evaporation.^{13,16-18} At room temperature, it is present in its cubic phase, and shown to be thermodynamically more stable than lead-based perovskites.^{13,17} However, power conversion efficiencies (PCE) of devices based on double metal perovskites are still below 3%.^{13,17} The high and indirect nature of its bandgap, higher density of trap states, and lower charge carrier mobilities compared to Pb-based perovskite, have been argued as limiting factors of the performance in devices.¹⁹

Recent studies have shown that the strong electron-phonon coupling in $\text{Cs}_2\text{AgBiBr}_6$, even stronger than in the commonly applied and studied methylammonium lead iodide (MAPbI_3), could potentially lead to self-trapping of the photoexcited charge carriers.²⁰ In $\text{Cs}_2\text{AgBiBr}_6$, self-trapping has been described as result of the formation of polarons, color centers, or even possibly self-trapped excitons.^{20,21} Any of these processes could be also potentially linked to the largely shifted and broad PL emission measured from $\text{Cs}_2\text{AgBiBr}_6$ samples.^{20,21} Furthermore, a recent study by Wright et al. showed an ultrafast charge carrier trapping process (1 ps time scale) into localized states.²¹ In contrast to such ultrafast dynamics in thin films, other reports have shown the presence of microsecond long-lived photoactive species by time resolved photoluminescence (TRPL), transient absorption (TA) and time-resolved microwave conductivity (TRMC) measurements in powders and crystals.^{16,22-24} In order to obtain a more complete model describing the photophysical processes in $\text{Cs}_2\text{AgBiBr}_6$, an in-depth study of the impact of these long-lived species on the charge carriers dynamics in $\text{Cs}_2\text{AgBiBr}_6$ is necessary. This work aims to provide insight into the nature of these states and their influence on the charge carrier dynamics in $\text{Cs}_2\text{AgBiBr}_6$ thin films. To do so, we investigated $\text{Cs}_2\text{AgBiBr}_6$ thin films by means of TRPL, TA measurements and double pulse excitation time-resolved microwave conductivity (DPE-TRMC), a new technique whose working principle is detailed in the methodology section. Basically, in DPE-TRMC the sample gets illuminated by two laser pulses arriving with a short time delay. By comparing the photoconductance traces induced by the second pulse in presence and absence of the first pulse, we are able to examine the effect of the long-lived species on the charge carrier dy-

namics. For these experiments we used identical excitation wavelengths for both laser pulses but varying intensities and delay times. We modelled the results introducing a comprehensive model, which accounts for the free carrier generation yield, localization of free carriers, electron trapping by color centers, and shallow trap states for holes. The iterative analysis of the DPE-TRMC experiments with different intensities and delay times reveals the presence of a high concentration of both electron (10^{15} cm^{-3}) and hole (10^{16} cm^{-3}) trap states. In addition, we show that both carriers are trapped on sub-ns timescales, while their depopulation occurs over tens of microseconds. Furthermore, we observe a higher mobility for holes compared to electrons, which amount to 5 and $0.01 \text{ cm}^2/(\text{Vs})$ respectively, in agreement with the imbalance in their effective masses.^{15,25} Localization of holes causes an effective loss in mobility for the holes, dropping to ca. $1.7 \text{ cm}^2/(\text{Vs})$, while no effect can be discerned for the electrons. Knowing these kinetic parameters allows us to predict the charge carrier dynamics under AM1.5, explaining the solar cell performance. Our new developed DPE-TRMC methodology gives direct insight on the timescales involved with population and depopulation of the various trap states in $\text{Cs}_2\text{AgBiBr}_6$, essential for the design of more efficient devices.

6.2. PEROVSKITE SYNTHESIS AND CHARACTERIZATION

$\text{Cs}_2\text{AgBiBr}_6$ thin films of about 150 nm were prepared by spin-coating a 0.5M solution of the precursor powders in DMSO onto a quartz (for TRPL and TRMC) or borosilicate (for TA) substrate, as detailed in Appendix 6.A. We confirmed the formation of the desired cubic phase, whose structure is schematically depicted in Figure 6.1a by X-ray diffraction measurements (Figure 6.A.1a). Scanning electron microscopy (SEM) imaging (Figure 6.A.1b) revealed a smooth and homogeneous coverage of the substrate with grain sizes varying from 100 to 400 nm. From absorption measurements we found an indirect and a direct bandgap at 2.57 and 3.05 eV, respectively, in line with previously reported values.^{20,26} The fraction of absorbed light, F_A , and photoluminescence, PL, are shown in Figure 6.1b in purple (left axis) and pink (right axis), respectively. Transmission and reflection spectra as well as temperature dependent absorption and PL are provided in Figures 6.A.2, and 6.A.3, respectively. The large Stokes shift observed for the PL has been associated with the radiative emission of electrons in color centers back to the valence band. Color centers are optically-active anionic vacancies which are formed in $\text{Cs}_2\text{AgBiBr}_6$ under common synthesis conditions.^{27,28}

6.3. DOUBLE PULSE TIME-RESOLVED MICROWAVE CONDUCTANCE (DPE-TRMC)

The DPE-TRMC results for 445-445 nm double excitation (above the bandgap excitation) are shown in Figure 6.2a. The red TRMC trace in the upper panel corresponds to the photoconductance trace, ΔG_1 generated using a single laser pulse at $t = 0$ with intensity I_1 . The orange trace, labelled with ΔG_2 , is induced by a single excitation at a delay time, $t_D = 500 \text{ ns}$ with intensity I_2 . Both types of excitations were performed at 445 nm (2.79 eV). As the excitation intensities of I_1 and I_2 are very close, the recorded ΔG_1 and ΔG_2 traces present similar kinetics and magnitudes. Since the photoconductivity of a

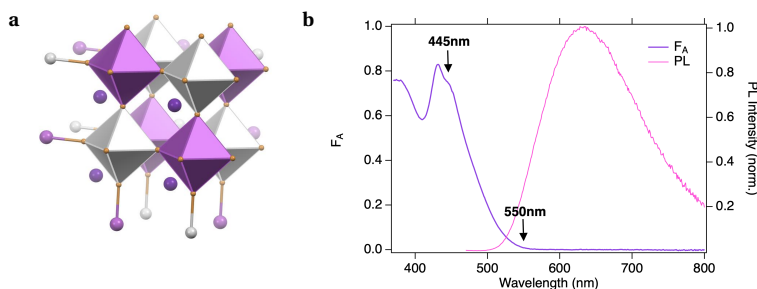


Figure 6.1: (a) General $\text{A}_2\text{B}'\text{B}''\text{X}_6$ perovskite structure, where purple and grey colors indicate the B' and B'' ions and respective octahedra. In (b) the fraction of absorbed light (F_A in purple) and photoluminescence (PL in pink) spectra are shown for the $\text{Cs}_2\text{AgBiBr}_6$ analyzed in this study. The excitation wavelengths for the main DPE-TRMC experiments are indicated by the black arrows.

material, ΔG , is proportional to the number of charge carriers and their mobilities, the observed rapid decay of the signal indicates swift recombination and/or immobilization of charge carriers. The measured lifetimes are in line with what has been previously reported regarding the fast trapping and recombination in $\text{Cs}_2\text{AgBiBr}_6$ perovskites.^{21,23,29} Figure 6.2a shows, in green, the DPE-TRMC signal, ΔG_{DPE} induced by excitation using two subsequent laser pulses with a delay of 500 ns. The ΔG_{DPE} signal shows how both laser pulses lead to two distinct signals. Interestingly, the second photoconductance signal in the ΔG_{DPE} trace is clearly larger than ΔG_2 although identical laser intensities are used. The difference is even more clear after subtracting ΔG_1 and ΔG_2 from ΔG_{DPE} , as shown in blue in the lower panel and denoted as ΔG_{Change} . A sizeable increment of the signal of approximately 10% induced by the second laser pulse is observed in the specific case of Figure 6.2a. This procedure has been repeated for multiple delay times and the results (ΔG_{Change}) are plotted as function of different delay times in Figure 6.2b. From here we can conclude that presence of the first laser pulse leads to an enhancement of the photoconductance generated by the second pulse even up to delay times of 30 μs . Note that this enhanced photoconductance is not related to a photoinduced absorption, since transient absorption measurements display a strong bleach at 445 nm. Instead, it seems that the increase is due to non-mobile photophysical products, that are still present 30 μs after the first laser pulse.

The above measurements are conducted in a resonant microwave cell, which has a response time of 18 ns. In order to further investigate the photoconductance enhancement at short delay times ($t_D = 50 - 100$ ns), we have also performed DPE-TRMC in a non-resonant TRMC cell, which has a response time of ca. 1 ns. The results, presented in Figure 6.B.1a, show how the positive effect of the first pulse on the photoconductance at short delay times is counteracted by a negative "bleaching" of the TRMC signal. Similar to transient absorption measurements, a bleaching of the TRMC signal could be due to a reduced charge carrier population in the band edge states for the second excitation. Furthermore, the excess charges induced by the first pulse will lead to an enhancement of second order recombination processes, which would lower the magnitude of the DPE-TRMC signal at short delay times.

In order to investigate if the enhancement is related to a specific excitation wave-

length, we also performed DPE-TRMC experiments exciting close to the band edges, at 550-550 nm (note here I_2 is almost two times larger than I_1). The results are shown in Figures 6.2c and 6.2d. Despite the fact that the signal heights of ΔG_1 , ΔG_2 , ΔG_{DPE} and of ΔG_{Change} are all much smaller due to the reduced optical absorption, remarkable similarities with those obtained at 445-445 nm are found. Although we cannot completely exclude some band tail absorption by the indirect bandgap, the presence of a substantial PL intensity at 550 nm wavelength, suggests that excitation at this wavelength can be related to excitation of electrons to the optically active color centers. This optical process leads to the presence of mobile holes in the valence band, obviously giving rise to similar photophysical products as for excitations at 445 nm explaining the similar observations for our DPE-TRMC experiments.

In sharp contrast to $\text{Cs}_2\text{AgBiBr}_6$, we observed negative ΔG_{Change} signals for other perovskites, like methylammonium lead iodide, MAPbI_3 . A direct comparison between $\text{Cs}_2\text{AgBiBr}_6$ and MAPbI_3 can be made by comparing Figures 6.2a with 6.2e for a 500 ns delay time, and 6.2b with 6.2f for a complete overview of the ΔG_{Change} signals as a function of varying delay times. From Figure 6.2f it is evident there is a clear match of the single pulse photoconductance decay and the decreasing trend of the maxima of the ΔG_{Change} signals. We link this behavior to the decreased charge carrier population in the band edge states and enhanced second order recombination. This behavior can be observed for over 1 μs , after which the ΔG_{Change} signal is completely reduced to zero. This means that for longer t_D values, the second excitation leads to identical results in both single and double pulse excitation modes. Similar results are obtained for the triple cation, lead halide perovskites as shown in Appendix 6.B, Figure 6.B.2. Although the charge carrier decay times are much slower than that of MAPbI_3 we observe negative ΔG_{Change} signals independent of the delay time. Most importantly, this is not the case for $\text{Cs}_2\text{AgBiBr}_6$: even after tens of microseconds after the microwave signal of the first pulse, the ΔG_{DPE} signal induced by the second laser pulse is higher than ΔG_2 only. To highlight the unicity of these results in $\text{Cs}_2\text{AgBiBr}_6$, we performed additional measurements on a sample containing a small fraction of antimony, namely $\text{Cs}_2\text{AgBi}_{0.8}\text{Sb}_{0.2}\text{Br}_6$. The characterization and DPE-TRMC results can be found in Appendix 6.B, Figure 6.B.3. As for MAPbI_3 , the ΔG_{Change} of $\text{Cs}_2\text{AgBi}_{0.8}\text{Sb}_{0.2}\text{Br}_6$ is negative at all the investigated delay times and the maxima of the ΔG_{Change} as function of the delay times follow the decay trend of the ΔG_2 signal without a first pulse.

6.4. MODELLING

Multiple phenomena could be responsible for an enhanced photoconductance during a DPE-TRMC experiment, such as *i*) an increased absorption, *ii*) release of trapped electrons/holes, *iii*) increase in temperature of the $\text{Cs}_2\text{AgBiBr}_6$ layer and/or *iv*) a higher yield of free mobile carriers due to the partial saturation of trap states by the first laser pulse. The first hypothesis, i.e. an increased absorption, is invalidated by the observation that the optical absorption is reduced (i.e. bleached) at 445 nm by transient absorption measurements on $\text{Cs}_2\text{AgBiBr}_6$.³⁰ A release of trapped carriers by the second pulse could also lead to an enhancement of the photoconductance in a DPE-TRMC measurement. We disprove this hypothesis by performing DPE-TRMC measurements with a first excitation at 445 nm (above the bandgap), followed by an intense 600 nm (below the bandgap)

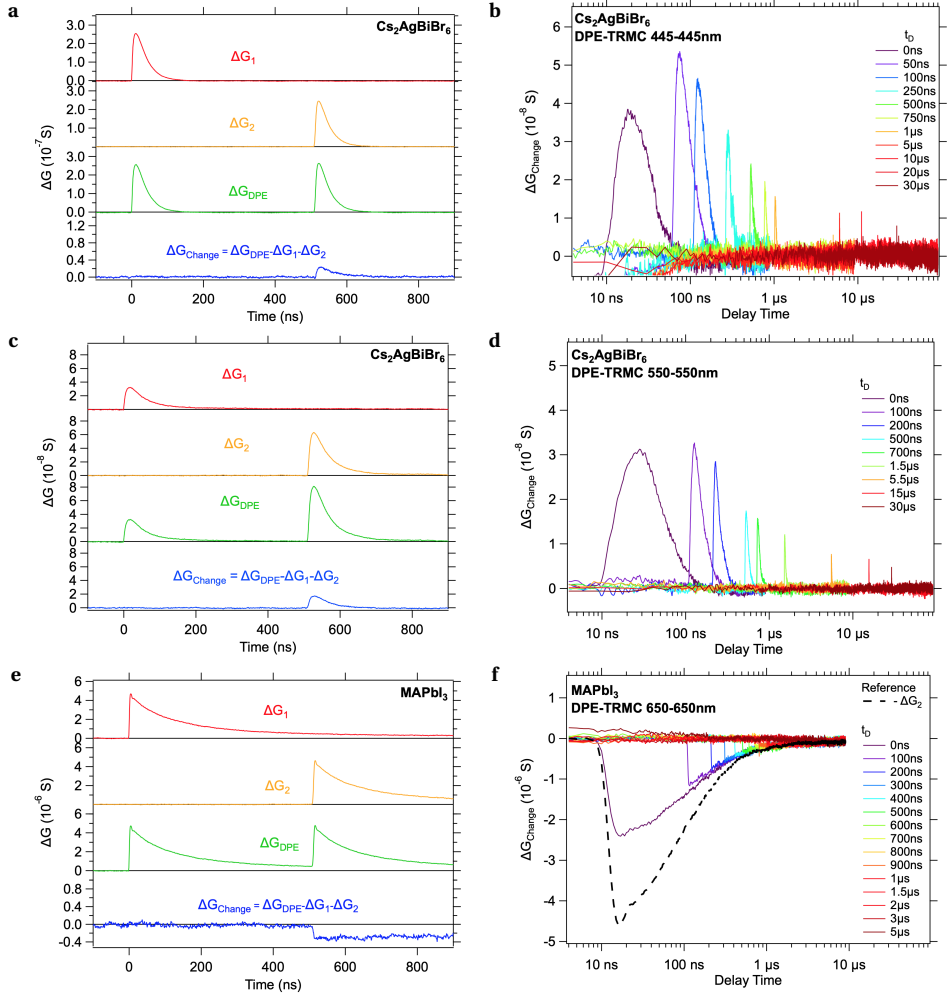


Figure 6.2: (a) $\text{Cs}_2\text{AgBiBr}_6$ upon 445-445 nm double pulsed excitation, (c) $\text{Cs}_2\text{AgBiBr}_6$ upon 550-550 nm pulsed excitation, and (e) MAPbI_3 upon 650-650 nm pulsed excitation. The red lines correspond to the traces obtained by the first pulse excitation only, the orange from the second, and the green a combination of the two. The blue traces, ΔG_{Change} , are the DPE-TRMC signals corrected for both first and second excitations. (b,d,f) Corrected DPE-TRMC signals obtained at different delay times ranging from 0 ns to 30 μ s for $\text{Cs}_2\text{AgBiBr}_6$ and MAPbI_3 . $\text{Cs}_2\text{AgBiBr}_6$ measurements have been performed using 1.4×10^{13} photons/cm² per pulse at 445 nm and 1.2×10^{14} photons/cm² at 550 nm, while a lower intensity of 2.6×10^{12} photons/cm² per pulse has been used for MAPbI_3 .

pulse. Since deep traps have energy levels within the bandgap of the material, i.e. broad photoluminescence is observed between 500 and 700 nm, a second 600 nm excitation should provide sufficient energy to release trapped carriers. If de-trapping would occur, the ΔG_{DPE} signal is expected to show changes in magnitude (increase) and in decay kinetics due to the presence of a higher concentration of mobile carriers. However, we did

not observe evidence of such process, as shown in Figure 6.B.1b. Here ΔG_{Change} is equal to zero at all delay times, indicating that no release of trapped carriers was induced by the second 600 nm laser pulse. As such, the DPE-TRMC trace is identical to the sum of ΔG_1 and ΔG_2 traces. Furthermore, we can exclude a rise in temperature as a possible explanation for the enhanced photoconductance as demonstrated in Appendix 6.B in Figure 6.B.4.

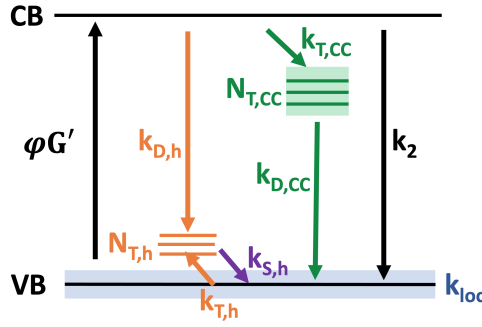


Figure 6.3: Schematic representation of the main kinetic processes and rate constants included in the TRMC and DPE-TRMC modelling. $\phi G'$ represents the charge carrier generation term. Following generation, sub-ps localization occurs whose effects can be mainly observed on the holes. This process proceeds with a specific rate constant, k_{loc} (blue). Electrons can be trapped into deep trap states, the so-called color centers (CCs), and from there recombine with holes in the valence band (green process). Trapped holes can either recombine with free electrons (orange process) or escape from shallow trapping by thermal excitation (purple arrow). Second-order band-to-band recombination is shown in black.

Having excluded options *i*), *ii*) and *iii*), we postulate a higher yield of free mobile carriers, due to relatively less trapping within the response time, since the traps are still populated from the first pulse. To verify this, we modelled the DPE-TRMC traces with a kinetic model accounting for fast localization of carriers, electron trapping into color centers, and shallow hole trapping. All these processes, schematically represented in Figure 6.3, have been separately observed in previous studies.^{20,21,23} We used a set of coupled differential equations (equations 6.1-6.5) to model the concentration of carriers in the different states. Namely, n_e is the time-dependent electron concentration in the conduction band, $n_{h,deloc}$ and $n_{h,loc}$ represent the hole concentrations before and after localization; $n_{T,CC}$ and $n_{T,h}$ are the electron and hole concentrations in their corresponding trap states. Electron localization has been excluded since it led to no effective change in neither mobility nor decay kinetics. The charge carrier generation term, G' , accounts for the intensity, I , and temporal profile of the laser pulse. Since the exciton binding energy in $\text{Cs}_2\text{AgBiBr}_6$ is appreciable,¹⁵ the excitation intensities were corrected for the free carrier generation yield, ϕ , i.e. the number of free carriers over the total number of excitations. As it will be further discussed and detailed in Appendix 6.C, this yield has been derived from the fittings to the experimental data points and related to the exciton binding energy with the help of the Saha model. In the following discussion, G'_1 will be used as generation term of ΔG_1 , G'_2 for ΔG_2 , and G'_{1+2} for ΔG_{DPE} . As shown in Figure 6.3, the trapping and de-trapping rate constants are k_T and k_D , respectively, while the localization rate constant is k_{loc} . Lastly, $k_{S,h}$ is the de-trapping rate constant accounting

for release of holes back into the valence band. In order to facilitate the visualization, the same color scheme adopted for the processes in Figure 6.3 is used in the equations.

$$\frac{dn_e}{dt} = \phi G' - k_2 n_e (n_{h,deloc} + n_{h,loc}) - k_{T,CC} (N_{T,CC} - n_{T,CC}) n_e - k_{D,h} n_{T,h} n_e \quad (6.1)$$

$$\frac{dn_{h,deloc}}{dt} = \phi G' - k_2 n_e (n_{h,deloc} + n_{h,loc}) - k_{loc} n_{h,deloc} - k_{T,h} (N_{T,h} - n_{T,h}) n_{h,deloc} \quad (6.2)$$

$$\frac{dn_{h,loc}}{dt} = k_{loc} n_{h,deloc} - k_2 n_e (n_{h,deloc} + n_{h,loc}) - k_{D,CC} n_{T,CC} n_{h,loc} + k_{S,h} n_{T,h} \quad (6.3)$$

$$\frac{dn_{T,CC}}{dt} = k_{T,CC} (N_{T,CC} - n_{T,CC}) n_e - k_{D,CC} n_{T,CC} n_{h,loc} \quad (6.4)$$

$$\frac{dn_{T,h}}{dt} = k_{T,h} (N_{T,h} - n_{T,h}) n_{h,deloc} - k_{D,h} n_{T,h} n_e - k_{S,h} n_{T,h} \quad (6.5)$$

For the fitting of the DPE-TRMC signals we multiplied the calculated concentration curves with their mobility values, μ , according to:

$$\Delta G = e\beta L (n_e \mu_e + n_{h,deloc} \mu_{h,deloc} + n_{h,loc} \mu_{h,loc}) \quad (6.6)$$

where e is the elementary charge, and β a waveguide geometrical factor, and L the sample thickness. On the basis of the different electron and hole effective masses in $\text{Cs}_2\text{AgBiBr}_6$, a major hole contribution to the ΔG signal magnitude is expected.¹⁵ A hole mobility of $5 \text{ cm}^2/(\text{Vs})$ was estimated from the model for the non-localized holes, quickly reducing to $1.7 \text{ cm}^2/(\text{Vs})$, in agreement with the sub-ns process reported by Wright et al.²¹, while the electron mobility is very low, approximately $0.01 \text{ cm}^2/(\text{Vs})$. Despite the negligible contribution of the electrons to the photoconductance signal (as per equation 6.6), their concentration has a strong impact on the observed decay kinetics.

The profiles G'_1 , G'_2 and G'_{1+2} for G' in equations 6.1 and 6.2 have been constructed on basis of the temporal profile and intensities, I_1 and I_2 of both laser pulses. The corresponding yields ϕ of free carrier generation are calculated taking into account the intensity of each laser pulse. Moreover, in case of G'_{1+2} , ϕ_2 has been determined accounting for the number of free carriers present at t_D after the first excitation. The kinetic parameters have been determined by iteratively fitting the ΔG_{DPE} traces recorded for a large variety of experiments with different intensities and delay times. Ultimately, the model is able to fit the DPE-TRMC traces accurately using the corresponding G'_{1+2} generation profile as shown in Figure 6.4. The fitting parameters are reported in Table 6.1. In Figure 6.4a, t_D has been set to 100 ns at which delay we recorded the maximum enhancement in photoconductance (see Figure 6.2b). Here, the intensity of the first pulse, I_1 has been varied from 0 to 10^{17} charges/ cm^3 , while the intensity of the second pulse, I_2 is constant. As is clear from Figure 6.4a, the higher I_1 , the larger the absolute rise in photoconductance upon the second pulse. Furthermore, the magnitude of the enhancement decreases over time as shown in Figure 6.4b for $t_D = 600$ ns and $t_D = 3 \mu\text{s}$. Also this aspect

is included in our model as clearly shown by the overlap between DPE-TRMC traces and our fits. For completeness, we also show the TRMC traces using only a single laser pulse and corresponding fits using the same model, showing decent overlap in Figure 6.B.5. Thus, variation in delay time as well as variation in intensity as presented in Figures 6.4 confirm the validity of our kinetic model, which clearly captures the main kinetic processes in $\text{Cs}_2\text{AgBiBr}_6$. From the time-dependent concentrations of the carriers in the different states (as described by equations 6.1-6.5, and reported in Figure 6.B.6), we can draw some important conclusions. Firstly, as expected, the delocalized holes do not play a relevant role in the observed photoconductance, as they disappear within the response time of our measurements. Nonetheless, their presence in the modelling is necessary, as hole trapping competes with the localization process. Secondly, in contrast to the fast localization and trapping, the de-trapping of both electrons and holes extends into the microsecond regime. As shown in Figure 6.B.6b, both carriers remain trapped for several μs after excitation. In conclusion the slow de-trapping of localized carriers in $\text{Cs}_2\text{AgBiBr}_6$ is the reason that in a double pulse experiment the second pulse yields a larger signal than in the absence of the first pulse. The fact that the DPE-TRMC measurements on MAPbI_3 show an opposite sign for ΔG_{Change} , independent of the delay time implies that population of trap states induced by the first pulse is not prevailing.

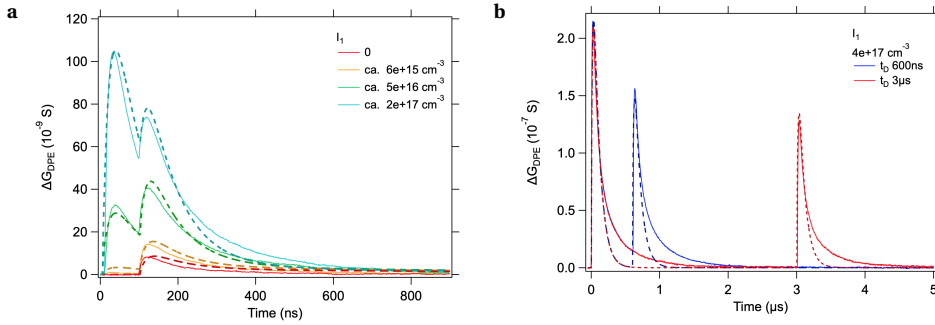


Figure 6.4: Experimental DPE-TRMC traces (solid lines) and corresponding fits (dashed lines) of $\text{Cs}_2\text{AgBiBr}_6$ (a) at variable I_1 and constant I_2 with a fixed of $t_D = 100$ ns. In (b) the same is shown for fixed laser intensities, but at $t_D = 600$ ns (blue) and $t_D = 3 \mu\text{s}$ at I_2 of $2 \times 10^{16} \text{ cm}^{-3}$.

Table 6.1: Fitting parameters for the $\text{Cs}_2\text{AgBiBr}_6$ sample analyzed in this study.

$k_{loc} (\text{s}^{-1})$	¹ 1.0×10^9
$k_2 (\text{cm}^3/\text{s})$	5.0×10^{-11}
$N_{T,CC} (\text{cm}^{-3})$	2.0×10^{15}
$k_{T,CC} (\text{cm}^3/\text{s})$	5.0×10^{-8}
$k_{D,CC} (\text{cm}^3/\text{s})$	6.0×10^{-9}
$N_{T,h} (\text{cm}^{-3})$	1.2×10^{16}
$k_{T,h} (\text{cm}^3/\text{s})$	6.5×10^{-7}
$k_{D,h} (\text{cm}^3/\text{s})$	9.0×10^{-11}
$k_{S,h} (\text{s}^{-1})$	5.0×10^5

¹At the highest intensity of I_1 a 3 times higher localisation rate is used.

6.5. DISCUSSION

In previous TRMC studies we have reported the presence of relatively high concentrations of trap states (10^{16} - 10^{17} cm^{-3}) for both electrons and holes.^{23,29} With our new model and iterative analysis of the DPE-TRMC traces at different intensities and delay times we are now able to quantify these concentrations more accurately and more importantly get insight regarding the depopulation times. To quantify the trap densities in more detail, we performed DPE-TRMC measurements with various intensities of the first and second pulse but keeping t_D constant at 100 ns. To study the changes induced by the first pulse on the second excitation, we subtracted ΔG_1 , from the ΔG_{DPE} signal.

$$\Delta G_{Cor} = \Delta G_{DPE} - \Delta G_1 \quad (6.7)$$

Next the maximum values of ΔG_{Cor} were normalized for the incident intensity of second laser pulse, I_2 , yielding the product of the free carrier generation yield, ϕ and the sum of electron and hole mobilities, $\Sigma\mu$ according to

$$\phi\Sigma\mu = \frac{\Delta G_{Cor,MAX}}{e\beta I_2 F_A} \quad (6.8)$$

and these values are plotted in Figure 6.5. From Figure 6.5 we can observe that, with $I_1 = 0$, the intensity normalized photoconductance maxima initially increase with higher I_2 , showing a maximum at $I_2 = 7 \times 10^{16}$ cm^{-3} , followed by a decrease. We have previously observed such behavior and this was explained by a dominant trap filling process at low photon fluences, while at higher intensities higher order recombination prevails.²⁹ Adding to this, it must be noted that also the yield of free carrier generation, ϕ is strongly intensity-dependent. As shown in Appendix 6.C Figure 6.C.1b, for exciton bindings energies in the range 100-200 meV, ϕ can decrease of more than a factor 4 in the intensity range analyzed.

By stepwise increasing I_1 up to 2×10^{17} cm^{-3} and keeping $t_D = 100$ ns, the trap filling process gradually disappears. The $\phi\Sigma\mu$ values obtained for maximum I_1 follow the more commonly observed intensity-dependent behavior we reported for several lead-containing perovskite thin films, i.e. lower values with higher intensities due to enhanced higher order recombination during the response time of our measurements.³¹ Since holes are the major contributors to the observed photoconductance signals, we conclude that the first laser pulse leads to rapid population of hole traps. The higher the occupation level of these states the higher the increase of the second laser pulse. The highest product of $\phi\Sigma\mu$ is approximately $0.35 \text{ cm}^2/(\text{Vs})$ (as visible from the blue points in Figure 6.5). Since the hole mobility was found to amount to $1.7 \text{ cm}^2/(\text{Vs})$, this translates into a free carrier generation yield of approximately 24% at room temperature at the lowest intensity of I_2 . As shown in Appendix 6.C Figure 6.C.1a, this implies an exciton binding energy of approximately 120-130 meV, in the range of previously reported values.^{15,32,33} However, it is important to highlight that during the fitting procedure both the mobility and ϕ values have been treated as variables. The found values were obtained only after iterative fittings with different laser intensities and delay times, as described in the above discussion.

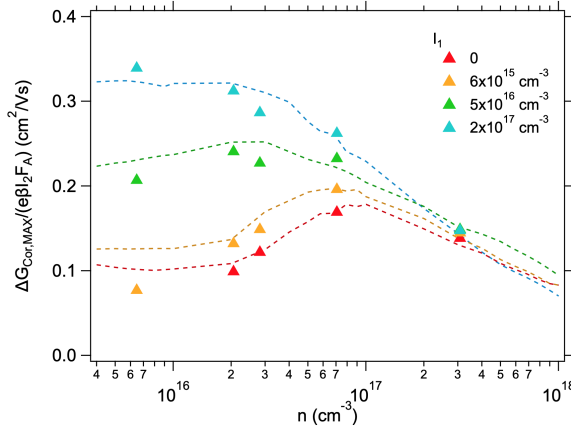


Figure 6.5: Plot of the I_2 normalized maximum ΔG_{Cor} values versus excitation density, n induced by I_2 . The vertical axis is a measure of the $\phi\Sigma\mu$ product. The intensity of the first pulse increases from red ($I_1 = 0$) to blue ($I_1 = 4 \times 10^{11}$ photons/cm² pulse). The delay time was kept constant at $t_D = 100$ ns. The dashed lines have been simulated for different I_1 over a broader range of I_2 . We note that the lowest I_1 and I_2 experimental points, i.e. red and orange at $n = 6 \times 10^{15}$ cm⁻³, are affected by poor signal-to-noise ratio. For this reason, the specific point at $I_1 = 0$ is not shown in the graph.

6.6. VERIFICATION WITH TRPL AND TA

To corroborate our observations and kinetic model, additional TRPL measurements were performed using a TRPL system using an excitation wavelength of 405 nm (red trace in Figure 6.6a). In agreement with previous studies a fast initial decay with a long-lived tail is observed.²² We simulated the TRPL signal applying our kinetic model with the rate constants mentioned in Table 6.1 and using a G' profile that represents the laser pulse with 80 ps FWHM and intensity used for the TRPL measurements. The simulations have been performed accounting for second order band-to-band recombination and emission from color centers. The normalized results are shown in Figure 6.6a. As noticeable, the simulation reveals the presence of a fast initial decay which originates from the recombination of free electrons with delocalized holes (black). However, based on the similarities in decay kinetics on longer timescales and relative magnitudes of the simulated intensities (see Appendix 6.D Figure 6.D.1), both 2^{nd} order recombination and trap-assisted recombination are expected to contribute to the observed long-living TRPL signals.

Moreover, we performed transient absorption (TA) measurements and compared the decay kinetics of the TA signal with the DPE-TRMC results. In previous work, we have performed a complementary TA/TRMC analysis revealing the pathways leading to mobility losses in Cs₂AgBiBr₆.³⁰ In the present study we focus on the charge carrier dynamics and lifetimes revealed by the two techniques. Following a similar procedure as in the analysis of TA absorption data, we normalized the maxima of ΔG_{Change} by the photoconductance maxima of ΔG_2 . The normalized DPE-TRMC trend at different delay times (blue dots-cavity), the single pulse TRMC trace (black line-open cell) and TA data (green line) are shown in Figure 6.6b. Furthermore, we accounted for the "bleaching"

effect on the DPE-TRMC signal at $t_D = 0$ ns. Most interestingly the lifetime of the TA signal matches the data of the DPE-TRMC results very well. Hence, we conclude that the long-lived trapped charges are responsible for the observed TA and DPE-TRMC signals. Since the mobile carriers are rapidly lost, the microseconds lifetimes can only originate by the slow release of holes from trap states close to the valence band (purple process in Figure 6.3 proceeding with a rate constant of $1 \times 10^5 \text{ s}^{-1}$). Accounting for the thermodynamic stability of the different defects states in $\text{Cs}_2\text{AgBiBr}_6$ reported in theoretical studies,^{27,28} we speculate the observed behavior can be caused by either silver vacancies (V_{Ag}) and/or silver-bismuth antisites (Ag_{Bi}). The fact that the same trend is not observed on partial substitution of Bi with Sb can be related to a change in electronic structure and defect stability induced by the substitution.

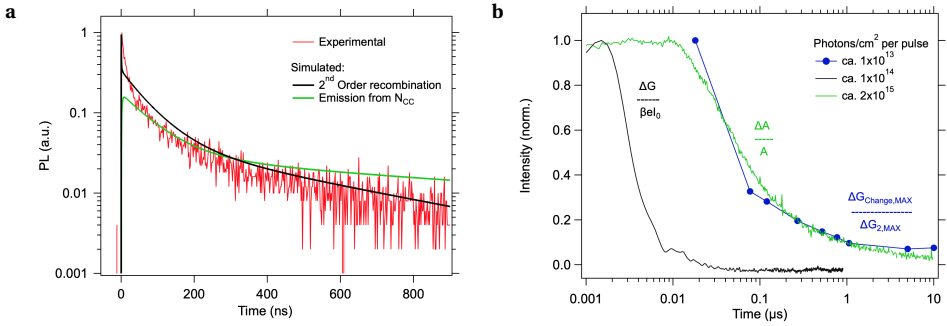


Figure 6.6: (a) Comparison of the experimental (red) and simulated (black and green) TRPL signals. The simulation has been done using the same kinetic parameters derived from DPE-TRMC measurements at an excitation intensity of approximately $4 \times 10^{16} \text{ cm}^{-3}$. (b) Normalized DPE-TRMC $\Delta G_{\text{Change,MAX}} / \Delta G_{2,\text{MAX}}$ (blue), transient absorption (green) and open cell TRMC (black) traces. The DPE-TRMC results have been normalized accounting for the bleaching effect at $t_D = 0$ ns.

6.7. EXTRAPOLATION TO SOLAR LIGHT

Lastly, by substituting G' in equations 6.1 and 6.2 with a continuous illumination profile corresponding to AM1.5, we can extrapolate the charge carrier concentrations on solar illumination.³⁴ For the calculations, the spectral photon flux has been corrected for the fraction of absorbed light for the $\text{Cs}_2\text{AgBiBr}_6$ thin film (details can be found in Appendix 6.E Figure 6.E.1). The time-dependent charge carrier concentrations on continuous illumination are reported in Figure 6.E.2. A detailed analysis of the processes over a broad range of intensities, i.e. 0.01-10 suns, reveals that upon continuous illumination almost all the electrons ($> 99.9\%$) decay via trap-assisted recombination. This results in extremely low free electron densities once the equilibrium is reached (see Appendix 6.E Figure 6.E.2). The evident dominance of trap-assisted electron recombination over the second order process during continuous illumination further supports the hypothesis that color center emission is responsible for the steady-state PL spectral features. For the positive charge carriers, the localization process is in competition with shallow trapping, yielding to a relatively low percentage of localized but mobile holes (approximately 28%), while the majority gets rapidly trapped (ca. 72%). The relative contribution

percentages are summarized in Table 6.2 at different illumination conditions. This analysis also reveals that under AM1.5 or even 10 suns both electron and hole trap states in $\text{Cs}_2\text{AgBiBr}_6$ do not saturate at all, despite the fact that charges remain trapped for long periods. The immobilization and loss of carriers via trap-assisted recombination is strongly detrimental for the performance of photovoltaic devices. However, long-lived charges in surface states may be beneficial for other applications such as photocatalysis or lasing.

Table 6.2: Simulation results of the percentage contributions of the localization, second-order recombination and trapping processes under continuous illumination. The saturation percentages of the electrons, $N_{T,CC}$, and holes, $N_{T,h}$, trap states is also reported.

	0.01 suns	0.1 suns	0.5 suns	1 sun	10 suns
2^{nd} order	0.001%	0.001%	0.002%	0.002%	0.003%
e^- trapping	>99.99%	>99.99%	>99.99%	>99.99%	>99.99%
$N_{T,CC}$ saturation	0.80%	1.93%	2.68%	3.32%	6.73%
h^+ localization	27.78%	27.79%	27.81%	27.86%	27.90%
h^+ trapping	72.22%	72.21%	72.19%	72.14%	72.10%
$N_{T,h}$ saturation	0.02%	0.08%	0.14%	0.20%	0.61%

6.8. CONCLUSIONS

To conclude, in this study we have performed extensive time-resolved measurements to reveal the complex charge carrier dynamics in $\text{Cs}_2\text{AgBiBr}_6$ thin films. We developed a new method i.e. double pulse excitation TRMC. By exciting the sample with two laser pulses, we obtain unprecedented detailed information regarding charge trapping and the corresponding depopulation process in $\text{Cs}_2\text{AgBiBr}_6$. Although single pulse TRMC experiments show that all mobile charges decay within 50 ns, we found that the second pulse led to an enhanced photoconductance up to 30 μs after the first pulse. Interestingly, this effect is only present when the energy of the second pulse exceeds the bandgap, meaning that this enhanced photoconductance is not related to trap release. Instead, we attribute the relatively higher photoconductivity from the second pulse to a higher yield of free charges, occurring as long as traps are populated from the first pulse. By using an intense first pulse complete saturation of the trap states can be accomplished, yielding maximal enhancement. For MAPbI_3 the opposite behavior is observed demonstrating that population of trap states by the first pulse is not prevailing and other factors such as second order recombination dominates. By varying wavelengths, intensities and delay times, we obtain a full picture of the (de-)population kinetics of defects in $\text{Cs}_2\text{AgBiBr}_6$. On analysis of all the data, a kinetic model is proposed showing to effectively capture the complex dynamics of photo-excited charges in the films. From the corresponding signal height, we derived a yield of 0.24 which concurs with an exciton binding energy of 120-130 meV. We found that electrons are rapidly trapped in color centers. Radiative emission of electrons from these color centers contributes to long-lived emission in agreement with the TRPL results. In line with TA observations, we conclude that holes get predominantly trapped in shallow states from which they release over many

microseconds. The trap-assisted recombination, effectively depleting the concentration of electrons in the conduction band, combined with the low hole mobility ($1.7 \text{ cm}^2/(\text{Vs})$) and shallow trapping, is expected to be a major drawback of $\text{Cs}_2\text{AgBiBr}_6$ in photovoltaic devices. Despite these limitations, the long-lived charge carriers in $\text{Cs}_2\text{AgBiBr}_6$ as observed in this work can offer a suitable, lead-free alternative for other applications, like X-ray detectors or photocatalysis.

PEROVSKITE SYNTHESIS

Thin films of approximately 150 nm (149 ± 31 nm) have been prepared in a N_2 filled glovebox by dissolving stoichiometric amounts of the precursor powders, CsBr (Sigma-Aldrich, 99.999%), AgBr (Strem, 99.9%), BiBr_3 (Sigma-Aldrich 99.998%), in anhydrous dimethyl sulfoxide (DMSO). A 0.5M solution has been stirred at 70°C for 1h, filtered with a filter of $0.22 \mu\text{m}$ pore size, and then spin-coated at 4000 rpm for 40 s on top of a quartz plate. The films have been dried at room temperature for 15 minutes and then annealed at 250°C for 5 minutes.

COMPLEMENTARY EXPERIMENTAL TECHNIQUES

Complementarily, transient absorption measurements were performed using an EOS multichannel pump probe transient absorption spectrometer (Ultrafast Systems LLC.). The third harmonic (355 nm) of a Nd:YAG laser (1064 nm, 650 ps FWHM pulse duration, 1 kHz) was used as the excitation source. Laser pulses with an energy of $4.5 \mu\text{J}$ were focused to a spot size of $3 \times 10^{-4} \text{ cm}^{-2}$, corresponding to a fluence of 2.7×10^{16} photons cm^{-2} per pulse. the probe pulse was generated using a LEUKOS super continuum light source (200-2400 nm, 200 mW, <1 ns) operating at 2 kHz. The white light is split into a probe and a reference beam, which is used to correct for fluctuations in the probe intensity. The reference and probe beam transmission spectra are both detected using fiber optics coupled multichannel spectrometer with a CMOS sensor (spectral resolution of 1.5 nm).

Time-resolved photoluminescence has been performed with an Edinburgh Instrument LifeSpec-ps spectrometer. The sample was excited at 404 nm by a Hamamatsu C8898 picosecond pulsed laser diode (repetition frequency 200 kHz, intensity 6×10^{11} photons/ cm^2).

BIBLIOGRAPHY

- (1) Jeong, J. et al. *Nature* **2021**, 592, 381–385.
- (2) Pazoki, M.; Jacobsson, T. J.; Hagfeldt, A.; Boschloo, G.; Edvinsson, T. *Physical Review B* **2016**, 93, 1–10.
- (3) Lau, C. F. J.; Deng, X.; Zheng, J.; Kim, J.; Zhang, Z.; Zhang, M.; Bing, J.; Wilkinson, B.; Hu, L.; Patterson, R.; Huang, S.; Ho-Baillie, A. *Journal of Materials Chemistry A* **2018**, 6, 5580–5586.
- (4) Wang, N.; Zhou, Y.; Ju, M. G.; Garces, H. F.; Ding, T.; Pang, S.; Zeng, X. C.; Padture, N. P.; Sun, X. W. *Advanced Energy Materials* **2016**, 6, 1–10.
- (5) Shao, S.; Liu, J.; Portale, G.; Fang, H. H.; Blake, G. R.; ten Brink, G. H.; Koster, L. J. A.; Loi, M. A. *Advanced Energy Materials* **2018**, 8, DOI: [10.1002/aenm.201702019](https://doi.org/10.1002/aenm.201702019).
- (6) Kopacic, I.; Friesenbichler, B.; Hoefler, S. F.; Kunert, B.; Plank, H.; Rath, T.; Trimmel, G. *ACS Applied Energy Materials* **2018**, 1, 343–347.
- (7) Chen, M.; Ju, M. G.; Garces, H. F.; Carl, A. D.; Ono, L. K.; Hawash, Z.; Zhang, Y.; Shen, T.; Qi, Y.; Grimm, R. L.; Pacifici, D.; Zeng, X. C.; Zhou, Y.; Padture, N. P. *Nature Communications* **2019**, 10, 1–8.
- (8) Cao, J.; Yan, F. *Energy and Environmental Science* **2021**, 14, 1286–1325.
- (9) Liu, X.; Wang, Y.; Wu, T.; He, X.; Meng, X.; Barbaud, J.; Chen, H.; Segawa, H.; Xudong, Y.; Han, L. *Nature Communications* **2020**, 11, 1–7.
- (10) Zhang, Z.; Yang, G.; Zhou, C.; Chung, C. C.; Hany, I. *RSC Advances* **2019**, 9, 23459–23464.
- (11) Chen, P.; Huang, Y.; Shi, Z.; Chen, X.; Li, N. *Materials* **2021**, 14, 2469.
- (12) Pan, W. et al. *Nat. Photonics* **2017**, 17, 726–732.
- (13) Wu, C.; Zhang, Q.; Liu, Y.; Luo, W.; Guo, X.; Huang, Z.; Ting, H.; Sun, W.; Zhong, X.; Wei, S.; Wang, S.; Chen, Z.; Xiao, L. *Advanced Science* **2018**, 5, 2–9.
- (14) Savory, C. N.; Walsh, A.; Scanlon, D. O. *ACS Energy Letters* **2016**, 1, 949–955.
- (15) Biega, R. I.; Filip, M. R.; Leppert, L.; Neaton, J. B. *Journal of Physical Chemistry Letters* **2021**, 12, 2057–2063.
- (16) Hoye, R. L.; Eyre, L.; Wei, F.; Brivio, F.; Sadhanala, A.; Sun, S.; Li, W.; Zhang, K. H.; MacManus-Driscoll, J. L.; Bristowe, P. D.; Friend, R. H.; Cheetham, A. K.; Deschler, F. *Advanced Materials Interfaces* **2018**, 5, 2–9.
- (17) *Materials Today* **2021**, xxx, DOI: [10.1016/j.mattod.2020.11.026](https://doi.org/10.1016/j.mattod.2020.11.026).
- (18) Fan, P.; Peng, H.-x.; Zheng, Z.-h.; Chen, Z.-h.; Tan, S.-j.; Chen, X.-y. **2019**, 6, 1–13.

- (19) Longo, G.; Mahesh, S.; Buizza, L. R. V.; Wright, A. D.; Ramadan, A. J.; Abdi-Jalebi, M.; Nayak, P. K.; Herz, L. M.; Snaith, H. J. *ACS Energy Lett.* **2020**, *5*, 2200–2207.
- (20) Zelewski, S. J.; Urban, J. M.; Surrente, A.; Maude, D. K.; Kuc, A.; Schade, L.; Johnson, R. D.; Dollmann, M.; Nayak, P. K.; Snaith, H. J.; Radaelli, P.; Kudrawiec, R.; Nicholas, R. J.; Plochocka, P.; Baranowski, M. *Journal of Materials Chemistry C* **2019**, *7*, 8350–8356.
- (21) Wright, A. D.; Buizza, L. R.; Savill, K. J.; Longo, G.; Snaith, H. J.; Johnston, M. B.; Herz, L. M. *Journal of Physical Chemistry Letters* **2021**, *12*, 3352–3360.
- (22) Slavney, A. H.; Hu, T.; Lindenberg, A. M.; Karunadasa, H. I. *Journal of the American Chemical Society* **2016**, *138*, 2138–2141.
- (23) Bartesaghi, D.; Slavney, A. H.; Gélvez-Rueda, M. C.; Connor, B. A.; Grozema, F. C.; Karunadasa, H. I.; Savenije, T. J. *Journal of Physical Chemistry C* **2018**, *122*, 4809–4816.
- (24) Pollock, T. P.; Schlenker, C. W. *J. Phys. Chem. C* **2021**, *125*, 18834–18840.
- (25) Zhang, H.; Debroye, E.; Zheng, W.; Fu, S.; Virgiglio, L. D.; Kumar, P.; Bonn, M.; Wang, H. I. *Science Advances* **2021**, *7*, DOI: [DOI:10.1126/sciadv.abj9066](https://doi.org/10.1126/sciadv.abj9066).
- (26) Schade, L.; Wright, A. D.; Johnson, R. D.; Dollmann, M.; Wenger, B.; Nayak, P. K.; Prabhakaran, D.; Herz, L. M.; Nicholas, R.; Snaith, H. J.; Radaelli, P. G. *ACS Energy Letters* **2019**, *4*, 299–305.
- (27) Xiao, Z.; Meng, W.; Wang, J.; Yan, Y. *ChemSusChem* **2016**, *18*, 2628–2633.
- (28) Li, T.; Zhao, X.; Yang, D.; Du, M.-H.; Zhang, L. *Phys. Rev. Applied* **2018**, *10*, 041001.
- (29) Hutter, E. M.; Gélvez-Rueda, M. C.; Bartesaghi, D.; Grozema, F. C.; Savenije, T. J. *ACS Omega* **2018**, *3*, 11655–11662.
- (30) Jöbsis, H. J.; Caselli, V. M.; Askes, S. H. C.; Garnett, E. C.; Savenije, T. J.; Rabouw, F. T.; Hutter, E. M. **2021**.
- (31) Savenije, T. J.; Guo, D.; Caselli, V. M.; Hutter, E. M. *Advanced Energy Materials* **2020**, *10*, 1–12.
- (32) Steele, J. A. et al. *Advanced Materials* **2018**, *30*, 1–7.
- (33) Kentsch, R.; Scholz, M.; Horn, J.; Schlettwein, D.; Oum, K.; Lenzer, T. *Journal of Physical Chemistry C* **2018**, *122*, 25940–25947.
- (34) Guo, D.; Caselli, V. M.; Hutter, E. M.; Savenije, T. J. *ACS Energy Letters* **2019**, *4*, 855–860.

APPENDICES

6.A. $\text{Cs}_2\text{AgBiBr}_6$ THIN FILM CHARACTERIZATION

The X-ray diffraction spectrum has been obtained with a *Brüker D8* diffractometer (Co $K\alpha$ -1 1.78Å). The resulting diffractogram (red) is shown in Figure 6.A.1a together with a reference spectrum (black).² Figure 6.A.1b shows the SEM spectrum of the sample deposited quartz.

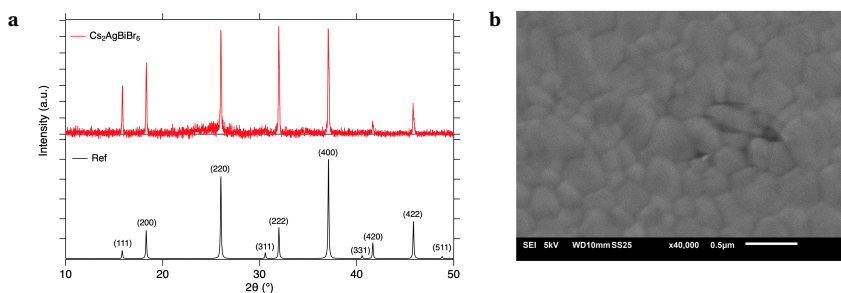


Figure 6.A.1: (a) XRD spectrum of $\text{Cs}_2\text{AgBiBr}_6$ thin film (red), and reference spectrum (black). (b) SEM image of the surface of the $\text{Cs}_2\text{AgBiBr}_6$ thin film.

Absorption and reflection spectra have been measured with a *Perkin Elmer Lambda 1050* spectrometers, equipped with an integrating sphere. The results are shown in Figure 6.A.2a. Figure 6.A.2b shows the light intensity within the sample at a distance L , calculates as per equation 6.A.1. From Tauc plots we have calculated the indirect and direct bandgaps, which resulted to be equal to 2.57 and 3.05 eV respectively in the thin films analyzed.

$$\frac{I_L}{I_0 - I_R} = e^{-\alpha L} \quad (6.A.1)$$

In equation 6.A.1, I_L represents the light intensity at distance L into the material, I_0 the incident intensity, I_R the reflected one, and α the absorption coefficient.

²Reference spectrum obtained from Slavney et al. J. Am. Chem. Soc. (2016), 138, 2138–2141

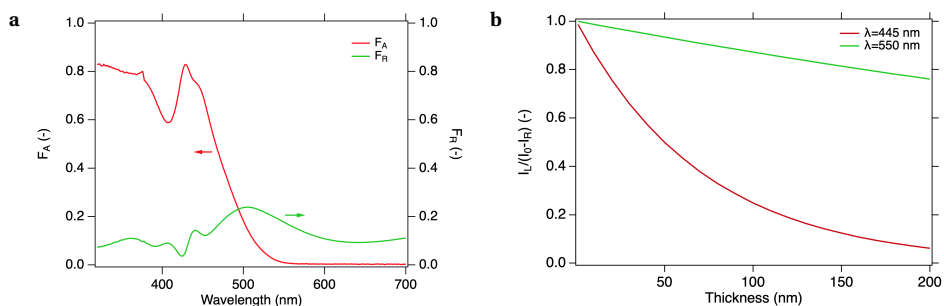


Figure 6.A.2: (a) Fractions of absorbed (red) and reflected (green) light in the 150 nm thick $\text{Cs}_2\text{AgBiBr}_6$ thin film; (b) light intensity profile at 445 nm (red) and 550 nm (green) excitation wavelengths.

Temperature dependent measurements (see Figure 6.A.3) have been conducted in a home-built set-up, which is able to perform both absorption and photoluminescence measurements. An *OceanOptics Maya 2000PRO* detector is used for absorption. Photoluminescence has been recorded with a *FLAME-S-VIS-NIR Ocean Optics* spectrometer upon photo-excitation by *CPS405 ThorLabs* laser diode at 405 nm.

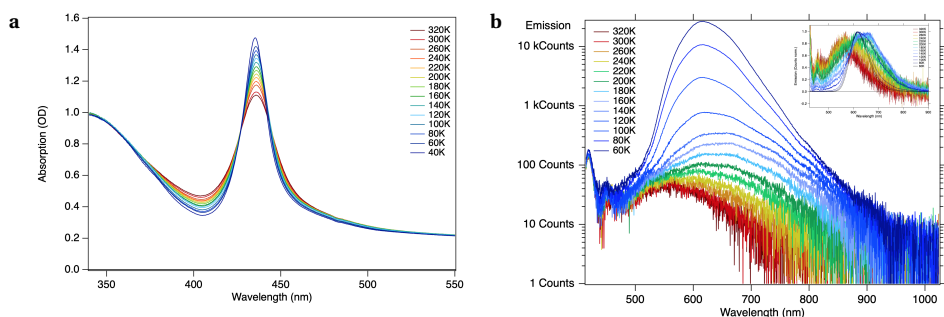


Figure 6.A.3: Temperature dependent optical characterization of $\text{Cs}_2\text{AgBiBr}_6$ thin film: (a) absorption, and (b) PL. The inset in (b) shows the normalized photoconductance in the temperature range analyzed. 40K photoluminescence spectrum is not shown as the detector reached saturation.

6.B. ADDITIONAL MEASUREMENTS

$\text{Cs}_2\text{AgBiBr}_6$

Measurements performed in an open cell reveal the extent of the "bleaching" of the TRMC signal at short delay times. As visible in Figure 6.B.1a, the apparent ingrowth of the signals at short delay times in the cavity (Figure 6.2b in the main text) can be ascribed to the partially lowered ΔG_{Change} signals due to the bleaching effect. Lastly, the DPE-TRMC results upon 445-600 nm are shown in Figure 6.B.1b.

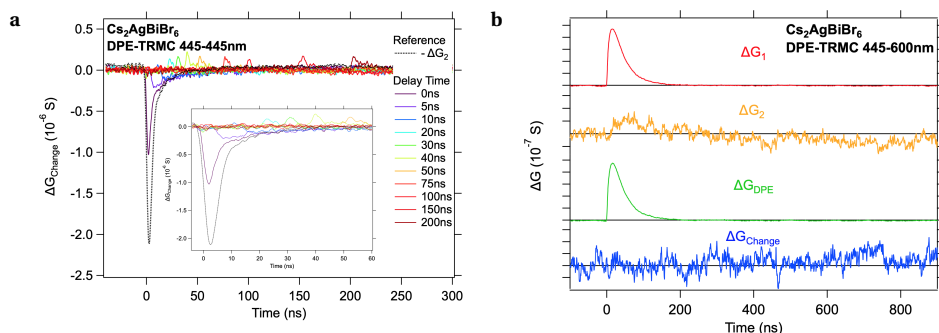


Figure 6.B.1: (a) ΔG_{Change} signals obtained by DPE-TRMC measurements conducted in an open cell. The inset focuses on the ingrowth of the positive feature after the bleaching of the first excitation signal. The sample has been photo-excited at 445-445 nm, with an intensity of approximately 1.5×10^{14} photons/cm². (b) DPE-TRMC at 445-600 nm excitation.

$\text{Cs}_{0.05}\text{FA}_{0.85}\text{MA}_{0.10}\text{Pb}(\text{I}_{0.97}\text{Br}_{0.03})_3$

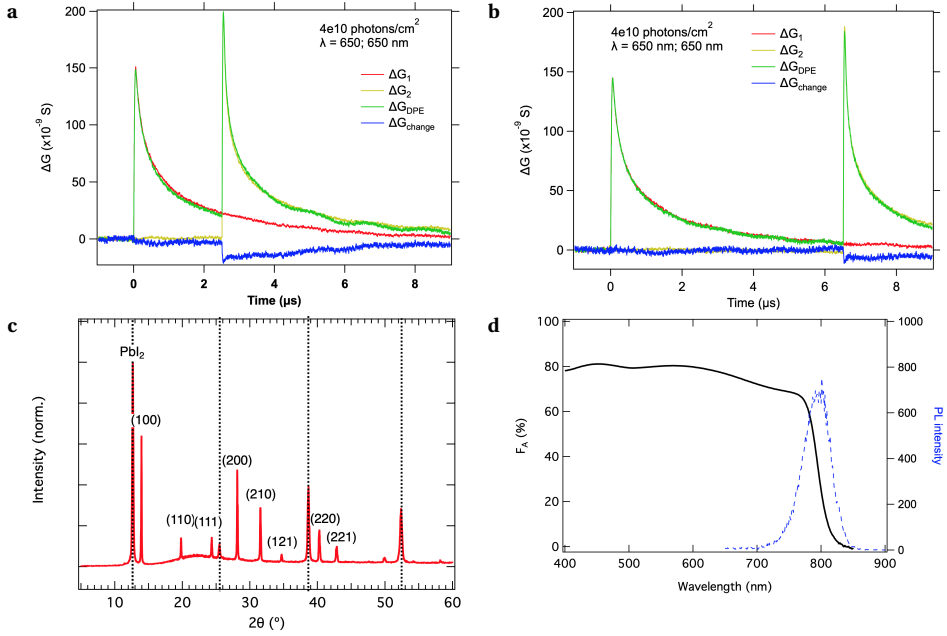


Figure 6.B.2: DPE experiment on $\text{Cs}_{0.05}\text{FA}_{0.85}\text{MA}_{0.10}\text{Pb}(\text{I}_{0.97}\text{Br}_{0.03})_3$ for a delay time of (a) 2.5 and (b) 6.5 μs. Excitation wavelength for both laser pulses is 650 nm. Independent of the delay time a negative signal is observed for the DPE-TRMC similar as has been observed for MAPbI_3 . The corresponding (c) XRD and (d) optical properties of the perovskite layer are added in the lower panels.

$\text{Cs}_2\text{AgBi}_{0.8}\text{Sb}_{0.2}\text{Br}_6$

Samples of mixed composition have been prepared following the same procedure reported above for $\text{Cs}_2\text{AgBiBr}_6$. To achieve the desired composition, stoichiometric amounts of BiBr_3 and SbBr_3 (Strem, 99%) have been added to the solution.

XRD diffraction spectrum is shown in Figure 6.B.3a, where a comparison is offered with the $\text{Cs}_2\text{AgBiBr}_6$ spectrum in the range 20–40°. The shift to higher angles is compatible with the inclusion of Sb in the structure. From the SEM image it is possible to notice the formation of some pinholes (see Figure 6.B.3b). Inclusion of Sb is supported also by the changes in the absorption spectra of the samples, as shown in Figure 6.B.3c.

DPE-TRMC measurements have been conducted also on this sample and the ΔG_{Change} signals at 445–445 nm excitation are shown in Figure 6.B.3d together with the mirrored ΔG_2 signal at the same intensity (as for MAPbI_3 in Figure 6.2f in the main text). Measurements are shown for t_D up to 500 ns as for longer delay times the signal to noise ratio was too low.

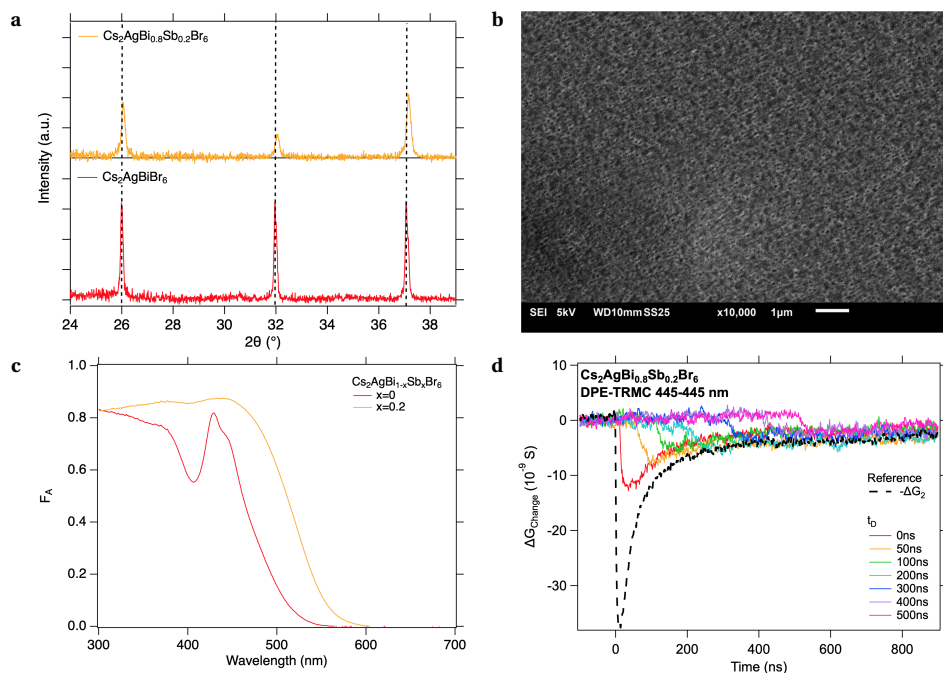


Figure 6.B.3: (a) XRD spectra of $\text{Cs}_2\text{AgBiBr}_6$ (red) and $\text{Cs}_2\text{AgBi}_{0.8}\text{Sb}_{0.2}\text{Br}_6$ (orange) in the range $20\text{--}40^\circ$, enhanced to highlight the shift caused by the inclusion of Sb (dashed black lines serve as eye guides only). (b) SEM image of the surface of $\text{Cs}_2\text{AgBi}_{0.8}\text{Sb}_{0.2}\text{Br}_6$. (c) Absorption spectrum of $\text{Cs}_2\text{AgBiBr}_6$ (red) and $\text{Cs}_2\text{AgBi}_{0.8}\text{Sb}_{0.2}\text{Br}_6$ (orange). (d) DPE-TRMC results of $\text{Cs}_2\text{AgBi}_{0.8}\text{Sb}_{0.2}\text{Br}_6$ upon 445-445 nm excitation at intensities close to 2×10^{14} photons/cm² per pulse.

EFFECT OF TEMPERATURE ON $\text{Cs}_2\text{AgBiBr}_6$ PHOTOCONDUCTANCE SIGNAL

On basis of the maximum used intensities for the first pulse of $1 \times 10^{13} \text{ cm}^{-2}$ and the perovskite layer thickness we can calculate the temperature rise in case all photon energy is converted into heat and no convection is occurring. Using typical values for the density of 4.4 gram/cm^3 and a heat capacity of about 300 J/KgK^3 , we come to a temperature rise of 17 K. If we compare that to the dependence of the signal size measured as function of temperature, as shown in Figure 6.B.4 we have to conclude that the modest change in temperature cannot be responsible for the observed changes in the double pulse experiments.

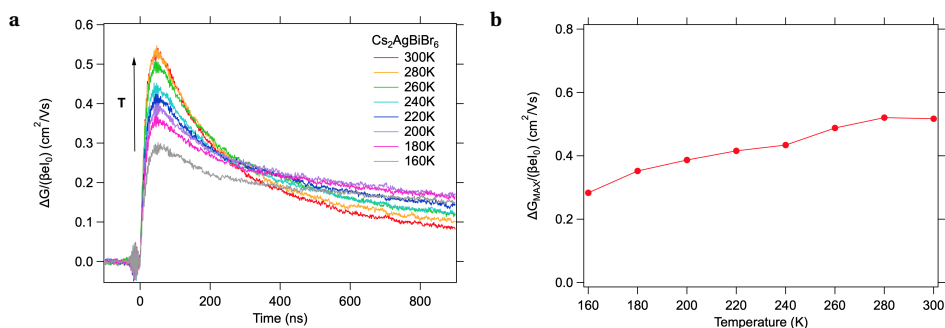


Figure 6.B.4: (a) TRMC traces recorded in the temperature range 300-160 K and (b) corresponding $\Delta G_{\text{MAX}} / (e\beta I_0)$ vs. temperature showing only a modest change in signal size over the entire temperature range.

ADDITIONAL DPE-TRMC FITTING RESULTS

Single pulse TRMC traces have been fitted to extract the kinetic parameters in absence of a pre-pulse, i.e. at $I_1 = 0 \text{ cm}^{-3}$. The results are shown in Figure 6.B.5.

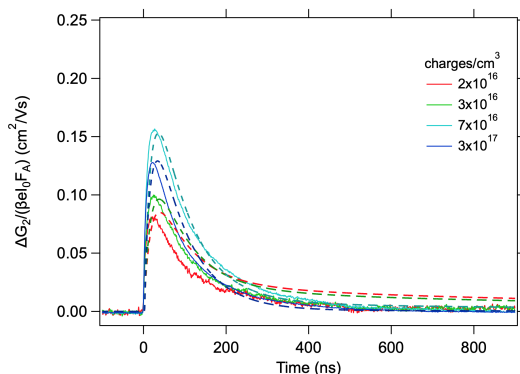


Figure 6.B.5: Single pulse TRMC traces obtained for $\text{Cs}_2\text{AgBiBr}_6$ for various laser intensities at an excitation wavelength of 445 nm including fits using the parameters mentioned in Table 6.1 in the main text.

³Value reported in Haeger, T. et al. (2020), J. Mater. Chem. C, 8, 14289–14311

The time-dependent concentrations of carriers in the different states can be extracted from the modelling of DPE-TRMC results. The results are shown in Figure 6.B.6 for a DPE-TRMC simulation at $t_D = 3 \mu\text{s}$ on 6.B.6a 1 μs and 6.B.6b 5 μs timescale. The fitted trace has been recorded at $I_1 = 3.6 \times 10^{17} \text{ cm}^{-3}$ and $I_2 = 2 \times 10^{16} \text{ cm}^{-3}$.

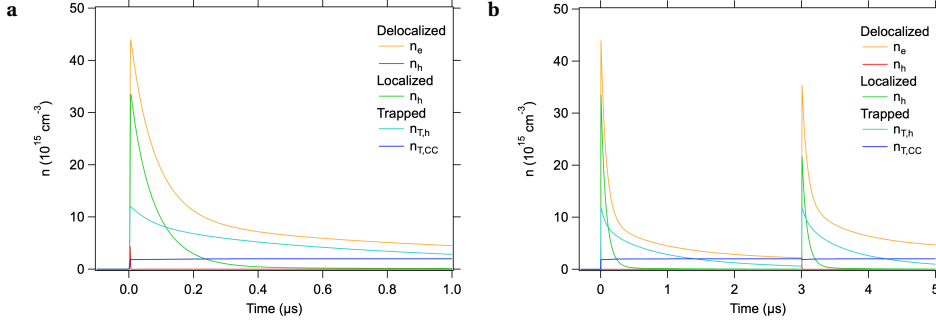


Figure 6.B.6: Time-dependent concentrations of delocalized (red), localized (green) and trapped (light blue) holes, and free (orange) and trapped electrons (blue) modelled upon 445-445 nm $t_D=3 \mu\text{s}$ excitation at I_1 of approximately $3.6 \times 10^{17} \text{ cm}^{-3}$ and I_2 of $2 \times 10^{16} \text{ cm}^{-3}$ on (a) 1 μs and (b) 5 μs timescale.

6.C. SAHA MODEL

The yield of free carriers, ϕ , over the total excitation, n , can be modelled with the help of the Saha equation as function of temperature, T , or the excitation intensity, n , according to equation 6.C.1.

$$\frac{\phi^2}{1-\phi} = \frac{1}{n} \left(\frac{2\pi m k_B T}{h^2} \right)^{3/2} e^{-\frac{E_B}{k_B T}} \quad (6.C.1)$$

In equation 6.C.1, m is the reduced effective mass, k_B the Boltzmann constant, h the Planck constant and E_B the exciton binding energy. The results are shown in Figure 6.C.1 in the E_B range 100-200 meV. The temperature dependency has been modelled on the following assumptions: *i*) the excitation intensity, n , has been set close to the saturation intensity, i.e. $2 \times 10^{17} \text{ cm}^{-3}$; *ii*) following the argumentation presented by Biega et al.⁴, we used the average value $0.27m_0$ for the reduced mass, m , with m_0 being the free electron mass.

The free carrier generation yield at room temperature has been estimated from the maximum photoconductance signal as mentioned in the main text. The maximum from open cell measurements (shorter response time) has been also considered as upper limit. The free carrier generation yield, i.e. n_{FC}/n , can be also defined as the fraction of absorbed photons leading to free carriers. Using the same notation as in equation 6.8 in the main text:

$$\phi = \frac{Ln_{FC}}{F_A I_0} \quad (6.C.2)$$

⁴Biega et al. (2021), J. Phys. Chem. Lett., 12, 2057–2063

where I_0 is the total incident intensity. The yield can be therefore estimated from the photoconductance maxima, as discussed in the main text.

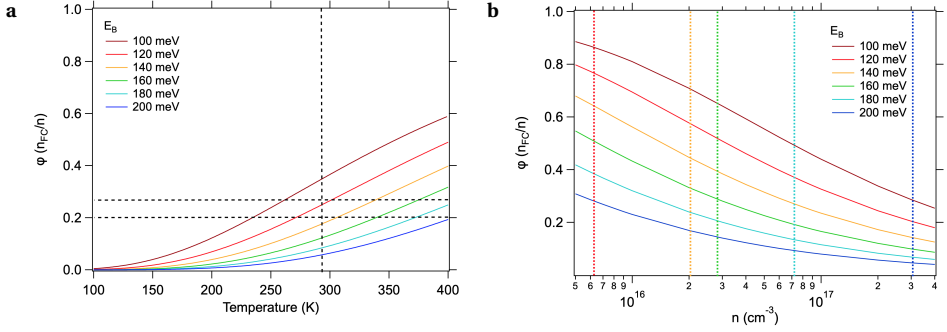


Figure 6.C.1: (a) Temperature dependent Saha model results in the exciton binding energy range 100-200 meV. The dotted lines represent the experimental temperature (296 K) and estimated yields of free carrier generation. (b) Concentration-dependent Saha model results. The dotted vertical lines represent the experimental intensities at which the model has been run in the main text.

6

6.D. TRPL SIMULATION

The TRPL signal has been simulated with the rate constants obtained from the fitting of the DPE-TRMC traces and the time-dependent concentrations modelled accounting for a generation profile G' that represents the TRPL laser pulse. The results are shown in Figure 6.D.1.

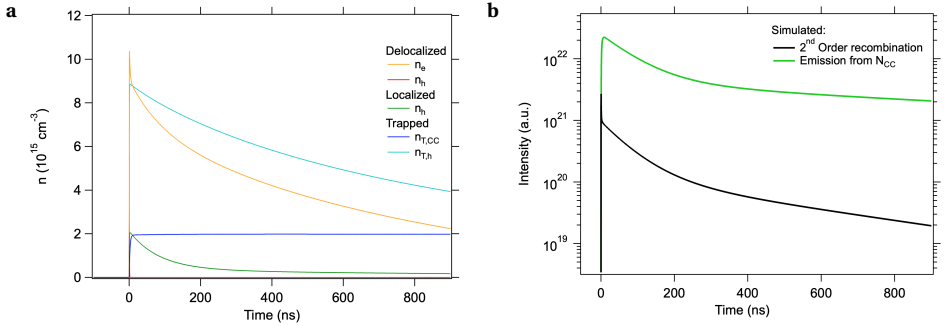


Figure 6.D.1: (a) Time-dependent concentrations upon a 405 nm excitation (80ps FWHM, $4 \times 10^{16} \text{ cm}^{-3}$) used for simulating the TRPL signals. (b) Results of the TRPL simulation accounting for second order recombination (black) and emission from color centers (green).

6.E. AM1.5 SIMULATION

The AM1.5 spectral photon fluence (black spectrum in Figure 6.E.1) has been corrected for the fraction of light absorbed by the $\text{Cs}_2\text{AgBiBr}_6$ sample under study. The corrected spectrum is shown in red in Figure 6.E.1. By integration, it is therefore possible to extrapolate the number of absorbed photons, which resulted to be approximately 2.5×10^{16} photons/cm².

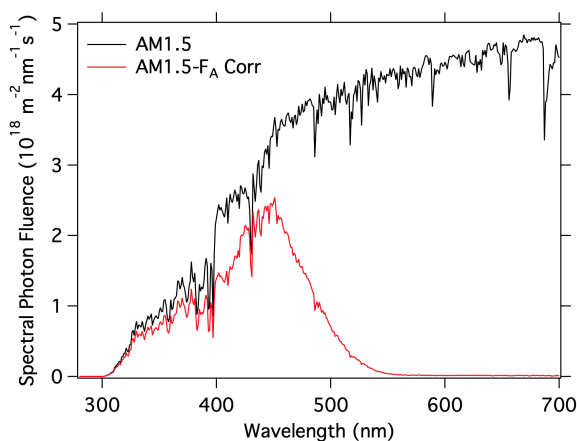


Figure 6.E.1: AM1.5 spectral photon fluence before (black) and after (red) correction by F_A .

The time-dependent electrons and holes concentrations at 0.1 and 10 suns are shown in Figure 6.E.2. Note that both delocalised charge carriers concentrations (red and orange traces) are orders of magnitude lower than trapped and localized carriers'. Specifically, at 0.1 suns $n_e = 7 \times 10^{10}$ and $n_h = 6 \times 10^8 \text{ cm}^{-3}$; at 10 suns $n_e = 5 \times 10^{11}$ and $n_h = 5 \times 10^9 \text{ cm}^{-3}$.

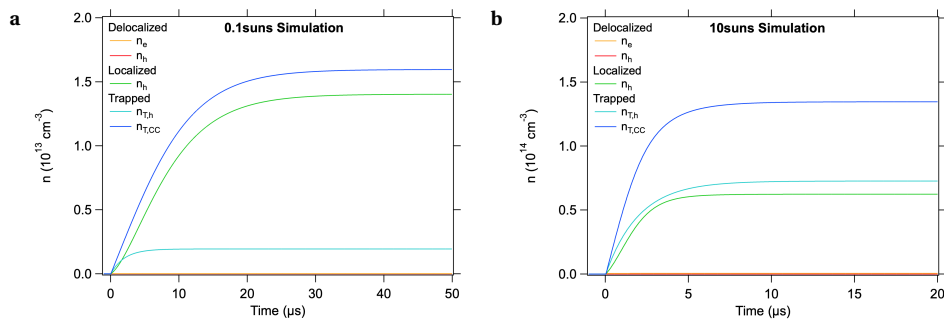


Figure 6.E.2: Calculated time-dependent concentrations upon (a) 0.1 and (b) 10 suns continuous illumination.

SUMMARY

For centuries we have relied on fossil fuels to produce energy for our needs, causing significant damage to the environment and our own health. To make an energy transition possible, technology has to step up, providing solutions for cleaner and cheaper energy production. In the field of solar energy, perovskite-based devices can offer a feasible alternative to conventional technologies, involving less energy intensive and cheaper manufacturing processes. Despite the great technological advancements of the past years, open circuit voltage losses and especially poor long-term stability are two of the main bottlenecks that still have to be overcome in order to bring the technology to market. In this thesis we have addressed such issues by investigating the origin and impact of electronic trap states on charge carrier dynamics in perovskite thin films of different composition. An introduction to the main properties of perovskite materials is provided in Chapter 1.

The fundamental properties of these materials have been investigated by means of different spectroscopic techniques. However, the core of the analyses relies on microwave conductance measurements. As discussed in Chapter 2, this technique can be used to investigate different properties of the materials, ranging from fundamental dielectric properties to charge carrier dynamics in presence of bias illumination. To this end, we implemented additional operational modes for the time-resolved microwave conductance (TRMC) measurements so far performed. Most importantly, for the first time we performed double pulse excitation time-resolved microwave conductance (DPE-TRMC) experiments on perovskite thin films. This technique offers unique insights into the charge carrier dynamics that allow us to reveal electronic trap states information inaccessible until now.

In Chapter 3 the results of steady-state microwave conductance measurements (SSMC) and impedance spectroscopy (IS) analyses on different Pb-based perovskites are discussed. Interestingly, higher dielectric losses in the GHz regime have been observed in MA-based perovskites, but not in FA- and Cs-based analogues. From the analysis of the temperature-dependent SSMC results, complemented with IS measurements, we have been able to relate such losses to the rotational motion of the methylammonium dipole, for which we determined activation energies and relaxation times in different compounds. However, despite the evident differences in the SSMC response, the temperature-dependent TRMC traces of all the perovskites analysed showed comparable trends, i.e. lower mobility and shorted lifetimes with higher temperatures. This study reveals that, notwithstanding its great impact on dielectric properties, the presence of the MA⁺ cation does not reduce charge carrier recombination nor significantly enhance defect screening in perovskite thin films.

Charge carrier recombination and defect states are the focus of interest in Chapter 4. Here, we provide a full description of the sub-bandgap absorption processes in MAPbI₃ thin films. Owing to the enhanced sensitivity of the TRMC technique, we have been able

to identify three distinct regions of optical excitation within the bandgap of the material. The first is a band tail region (Urbach tail) where band-like charge transport can still be observed. Surprisingly, charge extraction into selective transport layers can still occur even upon an excitation of 120 meV below the bandgap of 1.59 eV. Therefore, the presence of such tail of states is not expected to negatively impact neither the voltage nor the performance of MAPbI₃-based devices. The band-like transport becomes less prominent in a transitional region approximately 100 meV below the bandgap, gradually leaving place to defect absorption contributions. The latter becomes the dominant absorption process at low intensities below 1.40 eV. From the analysis of the photoconductance maxima in this region, we could show that the absorption arises from a limited number of optically active defect states, which can be now directly quantified. This work offers new insights on the relation between lattice vibrations and defects on the charge carrier dynamics in MAPbI₃ thin films.

Since one of the causes of instability and hysteresis in perovskite-based solar cells is the light-induced ionic motion within the perovskite layer, the recombination losses in pristine MAPbI₃ and bilayers with C60 or Spiro-OMeTAD have been further investigated performing TRMC measurements in presence of bias illumination (BI). With the analysis presented in Chapter 5 we close the gap between time-resolved analyses and device performances under continuous illumination, by quantifying kinetic parameters under bias illumination. As a consequence of the ionic motion, the concentration of trap states in the pristine MAPbI₃ layer is enhanced in presence of BI, leading to higher trap-assisted recombination losses. This effect is partially hindered by the presence of C60, which is known to passivate the perovskite surface. However, accumulation of electrons in the C60 under BI negatively impacts further extraction. On the contrary, the MAPbI₃/Spiro-OMeTAD interface is irreversibly affected by the mobile iodine ions under BI. As a result, we observed enhanced trap-assisted recombination in the MAPbI₃ layer as well as reduced hole extraction and higher interfacial recombination rate constants. This could be prevented by e.g. introducing an interlayer between the perovskite and transport layer. Furthermore, our study reveals the importance of accurately determining the kinetic parameters under operational conditions if we want to really investigate the origin of losses in devices. In fact, an erroneous determination of the relevant kinetic parameters could lead to large underestimation of the losses occurring in real applications.

Lastly, in Chapter 6 we reveal the potential of the newly developed double pulse excitation time-resolved microwave conductance (DPE-TRMC) technique in a study of the complex charge carrier dynamics in the double metal Cs₂AgBiBr₆ perovskite. Owing to the fact that during a DPE-TRMC experiment not only the intensity of illumination, but also wavelength and delay time in between the two pulses can be varied, we could obtain unique information over the charge trapping and depopulation time in Cs₂AgBiBr₆ thin films. Despite the rapid localization and trapping of the charge carriers in the (sub)nanosecond time scales, we observed higher photoconductance signals upon second pulse excitation, up to 30 μ s after the first pulse. By modelling the intensity-dependent DPE-TRMC data at various delay-times, we could relate such increment to a higher yield of free carrier generation during the second pulse. This is the result of the slow trap states depopulation time, which is here proven to occur over several tens of microseconds. While electrons are rapidly trapped in color centers (deep traps), holes

are predominantly trapped in shallow trap states where they reside for several microseconds. Utilizing the kinetic parameters extracted from our model, we simulated the contributions of the localization and recombination processes close to AM1.5 illumination conditions. The results show that almost all the electrons and more than 70% of the holes are lost in trap-assisted recombination processes. This factor, combined with the effective low mobilities of charge carriers in $\text{Cs}_2\text{AgBiBr}_6$ represents a major drawback for photovoltaic applications. Nonetheless, $\text{Cs}_2\text{AgBiBr}_6$ could still be a suitable active material in e.g. X-ray detection or photocatalysis.

Although remarkable progress has been made in improving the stability of perovskite-based devices, there is still room for improvement. Fundamental analyses, such as the ones presented in this thesis, are essential to achieve this goal. Contactless techniques, like TRMC, allow us to analyse the processes step-by-step, avoiding unwanted interference from multiple layers. Furthermore, the additional modes here presented open up a wide range of possibilities: SSMC could be used to verify the extent doping in the material or to investigate the origin of instability of Sn-based perovskites; TRMC with BI is used to reveal the suitability of an interface without the need of full device optimization; DPE-TRMC could be used not only to investigate trap states in different perovskites, but also the charge carrier kinetics during phase segregation or even the impact of Sn inclusion in Pb-based films.

SAMENVATTING

Eeuwenlang is men afhankelijk geweest van fossiele brandstoffen voor onze energiebehoeften met als gevolg aanzienlijke schade aan het milieu en onze gezondheid. Om een energietransitie mogelijk te maken, moet de technologie een tandje bijsteken en oplossingen bieden voor schonere en goedkopere energieproductie. Op het gebied van zonne-energie kunnen perovskiet-zonnecellen een goedkoper en energie zuiniger alternatief bieden voor conventionele zonneceltechnologieën. Ondanks de grote technologische vooruitgang van de afgelopen jaren, zijn verliezen in de nullastspanning en de slechte lange termijn stabiliteit twee van de belangrijkste knelpunten die nog moeten worden overwonnen om de technologie op de markt te kunnen brengen. In dit proefschrift hebben we dergelijke problemen opgepakt door onderzoek te doen naar de oorsprong en invloed van elektronische trapt toestanden op de dynamiek van ladingsdragers in dunne perovskietfilms bestaande uit verschillende componenten. In Hoofdstuk 1 wordt een inleiding gegeven in de belangrijkste eigenschappen van perovskietmaterialen.

De fundamentele eigenschappen van perovskietmaterialen zijn onderzocht aan de hand van verschillende spectroscopietechnieken. De primaire meettechniek is het microgolfgeleidingsexperiment (TRMC). Zoals besproken in Hoofdstuk 2 kan deze techniek worden gebruikt om verschillende materiaaleigenschappen te onderzoeken, variërend van fundamentele diëlektrische eigenschappen tot de dynamiek van ladingsdragers in de aanwezigheid van achtergrondverlichting. Hiertoe is het standaard microgolfgeleidingsexperiment uitgebreid. De nieuwste en belangrijkste uitbreiding is het dubbel-gepulsde microgolfgeleidingsexperiment (DPE-TRMC) die is toegepast op perovskiet dunne films. Deze techniek biedt unieke inzichten in de dynamiek van ladingsdragers en stelt ons in staat om niet eerder onthulde eigenschappen van elektronische vallen te bestuderen.

In Hoofdstuk 3 worden de meetresultaten van het steady-state microgolfgeleidings-experiment (SSMC) en impedantiespectroscopie experiment (IS) op verschillende Pb-gebaseerde perovskieten behandeld. Een resultaat is de observatie dat hogere diëlektrische verliezen in het GHz-regime zijn waargenomen in op MA-gebaseerde perovskieten, maar niet in op FA- en Cs -varianten. Uit de vergelijking van de temperatuurafhankelijke SSMC-metingen met IS-metingen kon worden afgeleid dat deze verliezen worden veroorzaakt door de rotatiebeweging van de methyllummonium-dipool. De activerings-energieën en relaxatietijden van deze rotatiebeweging zijn voor verschillende verbindingen bepaald. Ondanks de duidelijke verschillen in SSMC-metresultaten, waren de signalen uit de temperatuurafhankelijke TRMC voor alle geanalyseerde perovskieten vergelijkbaar, waarbij de mobiliteit lager werd en de levensduur van ladingen verkort bij hogere temperaturen. Deze studie toont aan dat, ondanks de grote impact op de diëlektrische eigenschappen, de aanwezigheid van het MA^+ kation de recombinatie van ladingsdragers niet vermindert, noch de afscherming van defecten in dunne perovskiet-

films significant verbeterd.

Recombinatie van ladingsdragers en defecten waren de focus het in Hoofdstuk 4 gepresenteerde onderzoek. In dit hoofdstuk geven we een volledige beschrijving van de sub-bandgap-absorptieprocessen in dunne films van MAPbI₃. Dankzij de verbeterde gevoeligheid van de TRMC-techniek hebben we drie verschillende regio's binnen de bandgap van het materiaal kunnen identificeren. De eerste is een bandstaartgebied (Urbach-staart) waar bandachtig ladingstransport kan plaatsvinden. Opmerkelijk is dat ladings-extractie in selectieve transportlagen nog steeds kan plaatsvinden, zelfs bij een excitatie van 120 meV onder de 1.59 eV bandgap. Daarom wordt niet verwacht dat de aanwezigheid van energieniveaus in deze Urbach-staart een negatieve invloed zal hebben op de spanning of de prestaties van op MAPbI₃ gebaseerde apparaten. Het bandachtige transport wordt minder prominent in een overgangsgebied op ongeveer 100 meV onder de bandgap. Hier wordt het aandeel van defecte absorptiebijdragen steeds groter. Met name bij lage intensiteiten onder 1,40 eV wordt dit het dominante lichtabsorptieproces. Uit analyse van de fotogeleidingsmaxima in dit gebied konden we aantonen dat de absorptie voortkomt uit een beperkt aantal optisch actieve defecten die direct konden worden gekwantificeerd. Dit werk biedt daarmee nieuwe inzichten in de relatie tussen roostertrillingen en defecten in de dynamiek van ladingsdragers in dunne films van MAPbI₃.

Een van de oorzaken van de instabiliteit en hysteresis in perovskietzonnecellen is de door licht geïnduceerde beweging van ionen in de perovskietlaag. Inzicht in dit proces is verkregen door een onderzoek naar de recombinatieverliezen in ongerepte MAPbI₃ en bilagen met C60 of Spiro-OMeTAD middels microgolfgeleidingsmetingen, in aanwezigheid van achtergrondverlichting (BI). Met de in Hoofdstuk 5 gepresenteerde data-analyse wordt de kloof gedicht tussen tijdsopgeloste analyses en apparaatprestaties onder continue verlichting, door het bepalen van kinetische parameters in aanwezigheid van achtergrondverlichting. Door de beweging van ionen verhoogt BI de concentratie van trapt toestanden in een enkele laag van MAPbI₃. Dit heeft hogere trap geassisteerde recombinatieverliezen tot gevolg. Het effect wordt gedeeltelijk belemmerd door de aanwezigheid van C60, waarvan bekend is dat het het perovskietoppervlak passiviert. Accumulatie van elektronen in C60 onder BI heeft echter een negatieve invloed op de verdere ladingsextractie. Daarentegen passiviert Spiro-OMeTAD het oppervlak niet en wordt het onomkeerbaar aangetast door de mobiele jodium-ionen in de aanwezigheid van BI. Dit resulteerde in een verbeterde trap-geassisteerde recombinatie in de MAPbI₃-laag, evenals een verminderde extractie van gaten en hogere constanten voor de grensvlak-recombinatiesnelheid. Deze gevolgen kunnen worden voorkomen door bijvoorbeeld het aanbrengen van een tussenlaag tussen de perovskiet- en transportlaag. Daarnaast laat ons onderzoek zien hoe belangrijk het is om de kinetische parameters onder operationele omstandigheden nauwkeurig te bepalen als we de oorsprong van verliezen in apparaten echt willen onderzoeken. In feite zou een foutieve bepaling van de relevante kinetische parameters kunnen leiden tot een grote onderschatting van de verliezen die optreden in echte apparaten.

Ten slotte bieden we in Hoofdstuk 6 inzicht in het potentieel van het nieuw ontwikkelde dubbel-gepulsde microgolfgeleidingsexperiment (DPE-TRMC) techniek, waarbij we de complexe dynamiek van ladingsdragers in het dubbele metaal Cs₂AgBiBr₆ perovs-

kiet hebben bestudeerd. Omdat tijdens een DPE-TRMC-experiment niet alleen de intensiteit van de verlichting, maar ook de golflengte en het interval tussen de twee pulsen kan worden gevarieerd, kunnen we unieke informatie verkrijgen over het verval van ladingen in vallen en de bijbehorende verblijftijd in dunne films van $\text{Cs}_2\text{AgBiBr}_6$. Ondanks een sneller verval van ladingen naar vallen, hebben we hogere fotogeleidingssignalen waargenomen bij de tweede pulsexcitatie, tot $30 \mu\text{s}$ na de eerste puls. Door de intensiteitsafhankelijke DPE-TRMC-gegevens te modelleren als functie van het tijdsinterval tussen twee pulsen, de intensiteitstoename worden gerelateerd aan een hogere opbrengst van mobiele ladingsdragers die werden gecreëerd tijdens de tweede puls. Dit is het resultaat van de lange levensduur rap-toestanden, die enkele tientallen microseconden lang is. Terwijl elektronen snel worden vastgezet in kleurcentra (diepe vallen), worden gaten voornamelijk vastgezet in ondiepe vallen waarin ze zich enkele microseconden bevinden. Met de kinetische parameters uit ons model hebben we de bijdragen van de lokalisatie- en recombinatieprocessen onder verschillende AM1.5-verlichtingsomstandigheden gesimuleerd. Hieruit blijkt dat bijna alle elektronen en meer dan 70% van de gaten verloren gaan in valgeassisteerde recombinatieprocessen. Deze factor, gecombineerd met de effectieve lage mobiliteit van ladingdragers in $\text{Cs}_2\text{AgBiBr}_6$, vormt een groot nadeel voor fotonvoltaïsche toepassingen. Niettemin zou $\text{Cs}_2\text{AgBiBr}_6$ nog steeds kunnen dienen als geschikt actief materiaal voor bijvoorbeeld röntgendetectie of fotokatalyse.

Hoewel er opmerkelijke vooruitgang is geboekt in het verbeteren van de stabiliteit op perovskiet gebaseerde apparaten, is er zeker ruimte voor verbetering. Fundamentele analyses, zoals die in dit proefschrift zijn gepresenteerd, zijn essentieel om dit doel te bereiken. Contactloze technieken, zoals TRMC, stellen ons in staat om de processen stap voor stap te analyseren, waardoor ongewenste interferentie van meerdere lagen wordt vermeden. Bovendien bieden de hier gepresenteerde varianten op de TRMC-techniek een breed scala aan mogelijkheden: SSMC kan worden gebruikt om de mate van doping in het materiaal te bevestigen of om de oorsprong van instabiliteit van op Sn-gebaseerde perovskieten te onderzoeken; TRMC met BI kan worden gebruikt om de geschiktheid van een interface te onthullen zonder de noodzaak van een volledige apparaatoptimalisatie; DPE-TRMC kan worden gebruikt om de kinetiek van ladingsdragers tijdens fase-scheiding of de impact van Sn-opname in op Pb-gebaseerde films te onderzoeken.

ACKNOWLEDGEMENTS

I would like to start these acknowledgements by thanking the person who made this project possible, my supervisor Tom. I still remember the lecture you gave during the photovoltaic course I attended back in 2015. After many classes about silicon, your overview on organic and perovskites (they were not such a hot topic back then) really got my attention, to the point I decided I would have really liked to do my thesis project in your group. Although I did arrive too late for the project on perovskites, you put me in contact with Ferdinand so I did have the opportunity to work in the OM group. I very much enjoyed that and when I heard there was a possibility to apply for a PhD under your supervision, I took that chance. I am glad I got the opportunity to work with you. I have always appreciated your way of supervising students and your ability to make such an enjoyable working environment for all of us. Thank you for your guidance, encouragement and support during the past four years.

A lot of people came and left during my time at OM. Sudeep, Dengyang, Damla, you have been my first office mates and I have very much enjoyed my time with you! Thank you for all the nice discussions and help during my first year. I confess I kept Taz on the chair next to me during the days the office was empty. Luckily, that did not last for long. Jiashang, Zimu, you were a very welcomed presence when I came back from my maternity leave. I truly enjoyed working with you. The same I can say for Jin and Luana. I wish you both best of luck with the very interesting project you are working on. I am sure you will be able to overcome all the issues. A special thank is also due to “my” last two students, Job and Leyi. Together with Jasmeen, you really made my last year unforgettable!

Luckily, I can say some people never left. Ferdinand, Arjan and Laurence, thank you all for the interesting discussions you often sparked with your comments during the meetings. Jos, you have been a pillar in my project and I could not thank you enough for all you have done.

Speaking of people that never left, Kevin you have been a constant in my life since the moment I met you. There are many things I could say, but I will limit my thanks here to the “professional” part of our relationship. Together with Ruben, you taught me a lot during my master thesis, and even more when I started the PhD. Even now, while finalizing this thesis, you managed to teach me more on programs like Adobe and Power Point. Thank you for everything.

Last but not least, voglio ringraziare la mia famiglia. Mamma, senza di te nulla di questo sarebbe stato possibile. Grazie per tutto quello che hai fatto e fai ancora per me. Sono grata del supporto che tu e papà mi avete sempre dato in ogni passo della mia carriera, fino ad arrivare dove sono ora. Un grazie speciale anche a mia sorella, non solo per il tuo supporto, ma anche per aver avuto la pazienza di leggere e correggere tutti i testi che ti ho mandato nell'ultimo periodo. Much appreciated!

CURRICULUM VITÆ

Valentina Marta CASELLI

16-04-1992 Born in Varese, Italy

EDUCATION

2018–Present	Delft University of Technology PhD Chemical Engineering Delft, The Netherlands
2014–2016	Delft University of Technology Master's Degree, Sustainable Energy Technology Delft, The Netherlands
2011–2014	Università Ca' Foscari Bachelor's Degree, Sustainable Chemistry and Technology Venezia, Italy



EXPERIENCE

2017–2018	Sungevity International Remote Solar Designer Amsterdam, The Netherlands
2015–2016	Delft University of Technology Teaching Assistant Delft, The Netherlands
2013	Università Ca' Foscari Assistant in "Planning and Evaluation" Venezia, Italy

LIST OF PUBLICATIONS

- **V.M. Caselli**, J. Thieme, H.J. Jöbssis, S.A. Phadke, J. Zhao, E.M. Hutter and T.J. Savenije, *Traps in the Spotlight: How Traps Affect the Charge Carriers Dynamics in Cs₂AgBiBr₆ Perovskite*, Cell Reports Physical Science 2022, 3, 101055
 - **V.M. Caselli** and T.J. Savenije, *Quantifying Charge Carrier Recombination Losses in MAPbI₃/C60 and MAPbI₃/Spiro-OMeTAD with and without Bias Illumination*, J. Phys. Chem. Lett. 2022, 13, 7523-7531
 - **V.M. Caselli**, Z. Wei, M.M. Ackermans, E.M. Hutter, B. Ehrler, and T.J. Savenije, *Charge Carrier Dynamics upon Sub-bandgap Excitation in Methylammonium Lead Iodide Thin Films: Effects of Urbach Tail, Deep Defects, and Two-Photon Absorption*, ACS Energy Lett. 2020, 5, 3821-3827
 - **V.M. Caselli**, M. Fischer, D. Meggiolaro, E. Mosconi, F. De Angelis, S.D. Stranks, A. Baumann, V. Dyakonov, E.M. Hutter, and T.J. Savenije, *Charge Carriers Are Not Affected by the Relatively Slow-Rotating Methylammonium Cations in Lead Halide Perovskite Thin Films*, J. Phys. Chem. Lett. 2019, 10, 5128-5134
-
- H.J. Jöbssis, **V.M. Caselli**, S.H.C. Askes, E.C. Garnett, T.J. Savenije, F.T. Rabouw and E.M. Hutter, *Recombination and localization: Unfolding the pathways behind conductivity losses in Cs₂AgBiBr₆ thin films*, Appl. Phys. Lett. 2021, 119, 131908
 - J. Zhao, **V.M. Caselli**, M. Bus, B. Boshuizen, T.J. Savenije, *How Deep Hole Traps Affect the Charge Dynamics and Collection in Bare and Bilayers of Methylammonium Lead Bromide*, ACS Appl. Mater. Interfaces 2021, 13, 14, 16309–16316
 - T.J. Savenije, D. Guo, **V.M. Caselli**, E.M. Hutter, *Quantifying Charge-Carrier Mobilities and Recombination Rates in Metal Halide Perovskites from Time-Resolved Microwave Photoconductivity Measurements*, Advanced Energy Materials 2020, 10 (26), 1903788
 - Z. Wei, D. Guo, J. Thieme, C. Katan, **V.M. Caselli**, J. Even, T.J. Savenije, *The importance of relativistic effects on two-photon absorption spectra in metal halide perovskites*, Nat Commun 2019, 10, 5342
 - K.M. Felter, **V.M. Caselli**, D.D. Günbas, T.J. Savenije, F.C. Grozema, *Interplay between charge carrier mobility, exciton diffusion, crystal packing, and charge separation in perylene diimide-based heterojunctions*, ACS Appl. Energy Mater. 2019, 2, 11, 8010–8021

- M.E.F. Bouduban, V.I.E. Queloz, **V.M. Caselli**, K.T. Cho, A.R. Kirmani, S. Paek, C. Roldan-Carmona, L.J. Richter, J.E. Moser, T.J. Savenije, M.K. Nazeeruddin, G. Grancini, *Crystal orientation drives the interface physics at two/three-dimensional hybrid perovskites*, J. Phys. Chem. Lett. 2019, 10, 19, 5713–5720
- D. Guo, **V.M. Caselli**, E.M. Hutter, T.J. Savenije, *Comparing the calculated fermi level splitting with the open-circuit voltage in various perovskite cells*, ACS Energy Lett. 2019, 4, 4, 855–860
- E. Cattaruzza, **V.M. Caselli**, M. Mardegan, F. Gonella, G. Bottaro, A. Quaranta, G. Valotto, F. Enrichi, $\text{Ag}^+ \rightleftharpoons \text{Na}^+$ ion exchanged silicate glasses for solar cells covering: down-shifting properties, Ceramics International 2015, 41, 5, 7221-7226